Fragmentation Dynamics of Triatomic Molecules : Contribution of Geometry

Tomoko Muranaka

UNIVERSITE de CAEN/BASSE-NORMANDIE

U.F.R. des SCIENCES

ECOLE DOCTORALE SIMEM

THÈSE

présenté par

Mlle. Tomoko MURANAKA

et soutenue
le 30 octobre 2007

en vue de l'obtention du

DOCTORAT de l'UNIVERSITE de CAEN

Spécialité: Milieux dilués et optique fondamentale
Arrêté du 07 août 2006

Dynamique de la fragmentation de molécules tri-atomiques: contribution de la géométrie

Membres du JURY

Mme. Karine WOHRER-BEROFF, Directrice de Recherche CNRS, Orsay **(*Rapporteur*)**
M. Haruo SHIROMARU, Professeur des Universités, Tokyo (Japon) **(*Rapporteur*)**
M. Jean-Pierre GRANDIN, Directeur de Recherche CNRS, Caen
M. Amine CASSIMI, Ingénieur CEA, Caen **(*Directeur de thèse*)**


BON VOYAGE!

Acknowledgements

This thesis is the result of three years of work in the laboratory CIRIL where I have been fueled and supported by many people. People sometimes compare life to a voyage. For me, especially, these three years in France was literally a long voyage, not always with moderate winds. It is a pleasant task to express my gratitude to all those who made this voyage possible.

The first person I would like to thank is my supervisor Dr. Amine Cassimi. With his enthusiasm, his great knowledge and skill of experiment, and his practical suggestion not only for research but also for life, he helped to navigate this voyage correct. I owe him lots of gratitude for having me show his way of research. It is difficult to overstate how much I have learned from him.

I owe my sincere gratitude to Dr. Serge Bouffard, Director of CIRIL, who accepted me to join this excellent laboratory. I would like to thank also for Dr. Emmanuel Balanzat, Vice Director of CIRIL for their administrative affaires. Also their interests for this research encouraged me a lot.

I am indebted to Prof. Dr. Lamri Adoui, who gave me the opportunity to come to France, for his kind assistance for joining AMA group of CIRIL. If he had not participated to the conference where we met!

My warmest thanks are due to Dr. Brigitte Ban-d'Etat, for her gracious suggestion. Her calm and thoughtful consideration has a deep impression on me.

I am grateful for all the member of CIRIL: researchers for their advice, technicians for their help (and well organized coffee time!), secretaries for administrative procedures… I wish to thank my many young colleagues who made "French life" attractive, especially Dr. Jimmy Rangama for his encouragement (with beers).

My sincere thanks are due to Dr. Karine Wohrer-Beroff, Prof. Dr. Haruo Shiromaru and Dr. Jean-Pierre Grandin for being a member of the jury. Their pointed questions and meaning discussions are deeply appreciated.

The financial supports of the French Government and of ITSLEIF are gratefully acknowledged. I would like to express my gratitude to Prof. Dr. Bernt Huber, Coordinator of ITSLEIF, for his consideration.

I appreciate the interest and contribution of Japanese professors, especially Prof. Dr. Toshiyuki Azuma, my former supervisor, and Prof. Dr. Yasunori Yamazaki.

Finally, I would like to express my loving thanks to my friends and family. Without their encouragement and understanding, it would have been impossible to finish this work and continue again the voyage.

Table of Contents

Introduction

Ce travail de thèse a été réalisé à la suite des études des collisions Ion-Atome, Ion-Molécule menées au laboratoire CIRIL. Après de premiers résultats concernant la molécule diatomique de monoxyde de carbone CO, nous avons abordé l'étude de la dynamique de fragmentation de molécules poly-atomiques.

Lors de l'interaction entre un ion multi-chargé rapide et une molécule, la durée de l'interaction est plusieurs ordres de grandeur plus brève que les temps caractéristiques des mouvements nucléaires dans la molécule. Ainsi plusieurs états électroniques de la cible sont peuplés alors que les noyaux conservent leur position initiale, celle de la molécule neutre. Ensuite la molécule ionisée se dissocie en libérant l'énergie potentielle excédentaire sous la forme d'énergie cinétique. Nous mesurons cette énergie cinétique par la technique COLTRIMS (COLd Target Recoil Ion Momentum Spectroscopy), alliant mesure de temps de vol et imagerie en multi-coïncidence.

Une cible poly-atomique simple pour commencer l'étude de la dynamique du processus de fragmentation moléculaire est le dioxyde de carbone CO_2, une molécule tri-atomique linéaire. Lors d'une précédente expérience, nous avons réussi à identifier le scénario de rupture de la liaison selon le degré d'ionisation.

Le CO_2 triplement ionisé, se dissociant par la voie $C^+/O^+/O^+$, présente une dynamique de type "fragmentation concertée synchrone", c'est-à-dire que les deux liaisons C-O sont rompues simultanément. En raison de la structure symétrique de CO_2^{3+}, les deux ions O^+ sont émis dans des directions opposées alors que l'ion central C^+ est presque au repos (figure f-1a).

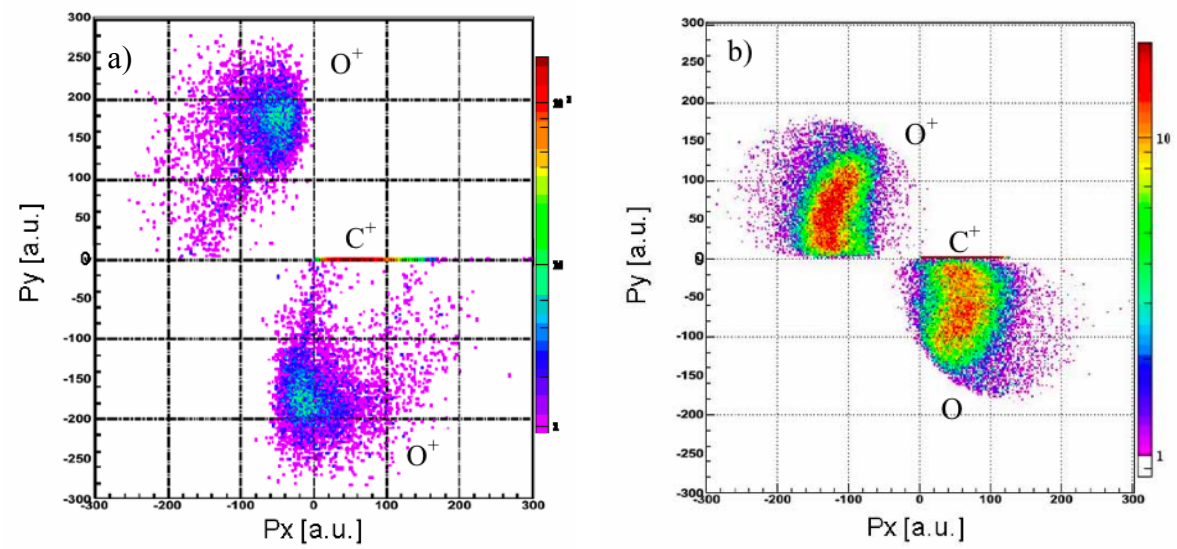

Figure f- 1 Diagramme de Newton de la fragmentation de CO_2 en a) $C^+/O^+/O^+$ et b) $C^+/O^+/O$. La quantité de mouvement du C^+ est choisie comme axe P_x, le O^+ (le plus énergétique pour le cas de $C^+/O^+/O^+$) est placé dans la partie supérieure du diagramme ($P_y>0$).

Contrairement au cas de la fragmentation de la molécule triplement ionisée qui suit un mécanisme simple de type "explosion coulombienne", le CO_2 doublement ionisé présente un comportement plus compliqué. Notamment, le canal de dissociation le plus fréquemment observé est la fragmentation à deux corps: $CO_2^{2+} \rightarrow CO^+ + O^+$. Le diagramme de Newton de la dissociation complète $CO_2^{2+} \rightarrow C^+ + O^+ + O$ montre clairement que l'atome d'oxygène neutre est émis dans la même direction que l'ion C^+ (figure f-1b). Ceci peut être la manifestation de l'existence d'une étape

intermédiaire CO^+/O^+ avant la dissociation complète en trois fragments. Ce type de fragmentation, qui n'est ni une "fragmentation concertée synchrone" ni une "fragmentation séquentielle pure" est appelé "fragmentation concertée asynchrone".

Afin d'étudier l'influence de la géométrie sur la dynamique de la fragmentation, nous avons décidé de conduire le même type d'expériences avec la molécule de dioxyde d'azote NO_2 qui, contrairement au CO_2, n'est pas linéaire.

Une autre approche pour révéler le mécanisme de fragmentation d'une molécule tri-atomique est discutée dans cette thèse. Le dication de la molécule d'eau deutérée HDO^{2+} présente une rupture préférentielle de la liaison OH. Avant ce travail de thèse, deux valeurs différentes du rapport de branchement $(H^+ + OD^+)/(D^+ + OH^+)$ ont été obtenues expérimentalement pour une fragmentation induite par impact d'ion rapide (CIRIL et KSU). Deux approches théoriques différentes ont également permis d'évaluer ce rapport. Notre précédent résultat a été comparé au calcul semi-classique s'appuyant sur la surface d'énergie potentielle de l'état fondamental de HDO. Bien que les résultats expérimental et théorique soit en accord pour ce qui concerne la rupture préférentielle de la liaison OH, ainsi que l'énergie cinétique libérée (KER) par chacune de ces deux voies de fragmentation $H^+ + OD^+$ et $D^+ + OH^+$, des différences importantes subsistent pour ce qui est du rapport de branchement entre ces deux voies.

Les questions encore ouvertes au début de ce travail de thèse sont les suivantes:

- Y a-t-il une contribution des états excités du dication sur cet effet isotopique?
- Quelle est la distribution d'énergie cinétique pour chacune des voies de dissociation?
- Comment les autres isotopomères (H_2O, D_2O) se comportent-ils?

Dans cette thèse, pour répondre à ces questions, nous avons développé un spectromètre adapté à ces voies spécifiques de la dissociation à deux corps de la molécule d'eau doublement chargée.

Dispositif expérimental

Dans l'étude de la dynamique de fragmentation d'une molécule, l'information primaire est la distribution d'énergie cinétique emportée par les fragments (KER: Kinetic Energy Release). Ces dernières années, notre groupe a réalisé la mesure de KER en haute résolution à l'aide de la technique la plus récente utilisée dans le domaine de la spectroscopie d'impulsion d'ions reculs "COLTRIMS". Notre dispositif expérimental est constitué de cinq parties principales:

- un faisceau d'ions projectiles fourni par l'accélérateur GANIL
- un jet supersonique de faible diamètre délivrant un faisceau monocinétique de molécules - un spectromètre de vitesse permettant la détection des fragments avec un angle solide de 4π stéradians
- deux détecteurs sensibles en position placés en vis à vis pour la détection des ions reculs et des électrons en coïncidence
- un système d'acquisition permettant une détection multi-hit en mode événement par événement.

Projectiles:

Dans ce travail de thèse, nous avons utilisé un faisceau d'ions S^{15+} à 13,7 MeV/u pour l'expérience dédiée à la molécule HDO et Ne^{8+} à 4,7 MeV/u pour l'expérience dédiée à la molécule NO_2. L'intensité du faisceau est ajustée afin d'obtenir un nombre moyen d'événements de coïncidence de l'ordre de 2000 coups par seconde et ainsi assurer la corrélation des électrons avec les ions détectés.

Jet supersonique:

L'objectif de la mesure étant de déterminer les vecteurs impulsion initiaux des fragments en haute résolution, la température des molécules cibles doit être basse et le diamètre de la zone de collision doit être faible. Les jets moléculaires de type "supersonique" satisfont pleinement ce cahier des charges.

NO_2: La manipulation du dioxyde d'azote NO_2 est plutôt délicate. Tout d'abord c'est un gaz fortement toxique. De plus, NO_2 est liquide à température ambiante et se polymérise à basse température (présence du dimère N_2O_4). En pratique, nous avons chauffé le générateur de jet à une température d'environ 100°C, permettant ainsi de conserver la proportion de NO_2 à 89% dans la cible.

HDO: La molécule de HDO est obtenue à partir de la vapeur du mélange liquide de H_2O et D_2O en proportions égales. Le jet se compose alors des trois molécules HDO, H_2O et D_2O dans un rapport de proportion de 2:1:1 respectivement. Ce mélange de trois isotopomères permet une comparaison directe des résultats respectifs de fragmentation. La pression de vapeur a été maintenue à environ 550mbars correspondant à une température de 84°C.

Spectromètre:

Le spectromètre se compose de deux parties: l'une dédiée à la détection des ions reculs et l'autre à celle des électrons. Dans ce travail de thèse, nous avons adapté le spectromètre à chacune des expériences : NO_2 et HDO.

NO_2: Afin d'observer différentes voies de dissociation, comprenant les voies impliquant un fragment neutre telle que $N^+/O^+/O$, nous avons adopté un spectromètre en condition "focalisation en temps" (figure f-2). Cette configuration permet de s'affranchir du volume de la zone de collision et ainsi obtenir une résolution suffisante même si tous les fragments ne sont pas détectés. C'est la configuration standard de toutes les expériences de spectroscopie d'impulsion (COLTRIMS).

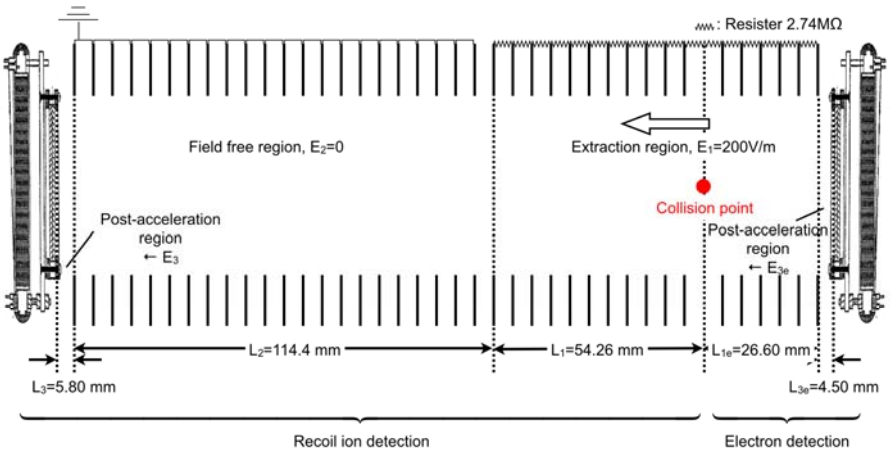

Figure f- 2 Schéma du spectromètre de temps de vol: type "focalisation de temps"

HDO: Une alternative, appelée "focalisation en position" et utilisable uniquement pour les événements complets pour lesquels tous les fragments sont détectés, consiste à s'affranchir de la zone de vol libre dans le spectromètre. Dans ce cas, puisque le détecteur sensible en position peut être monté plus prés du point collision, une meilleure résolution est obtenue. Les évènements complets auxquels nous nous sommes intéressés sont les voies $H^+ + OD^+$, $D^+ + OH^+$, $H^+ + OH^+$ et $D^+ + OD^+$. En imposant la conservation de la quantité de mouvement, ces voies sont clairement séparées.

Détecteur:

Afin d'obtenir l'information sur le partage de quantité de mouvement entre les fragments, nous devons mesurer leur vecteur vitesse. Cette mesure est réalisée en utilisant les détecteurs sensibles en position (PSD) fournissant deux types d'observables: l'information temporelle correspondant au temps d'arrivée des particules sur le détecteur (galettes de micro-canaux, MCP), et la position de leur point d'impact par des anodes à ligne à retard montées à l'arrière des MCP. L'efficacité de détection nominale de ce PSD est environ 50%.

Système d'acquisition:

Les signaux rapides issus des détecteurs constituent un évènement multi-paramétrique et nécessitent un système de traitement électronique sophistiqué. Nous avons construit un programme d'acquisition et d'analyse en temps réel fondé sur le système d'acquisition du GANIL au standard CAMAC et VME. Les événements sont sélectionnés par le "trigger" lors d'une détection en coïncidence des trois particules : projectile-electron-ion recul.

Analyse des données

L'étape d'analyse des données nous permet d'effectuer la calibration du dispositif puis de déterminer les quantités physiques à mesurer. Un des avantages de la calibration d'un spectromètre COLTRIMS est qu'elle est réalisée à partir des données mesurées elles-mêmes. L'algorithme que nous avons mis en œuvre est le suivant:

-Préparation des données

Il s'agit, dans un premier temps, de trier les évènements pour ne garder que ceux qui pourront être analysés. C'est également au cours de ce tri que les données sont converties du format du logiciel d'acquisition (format IN2P3) au format du logiciel de dépouillement ROOT.

-Détermination des paramètres de calibration

La deuxième partie du traitement des données consiste à déterminer les paramètres de calibration que sont le point d'origine de détecteur ainsi que les constantes de conversion des codeurs afin de remonter finalement aux quantités physiques.

-Sélection des événements

Afin d'éviter les événements correspondant à des fausses coïncidences, les données enregistrées sont filtrées et choisies sur des critères de multiplicité des différents signaux.

-Etalonnage des spectromètres

Cette étape indispensable de l'analyse consiste à déterminer les valeurs du champ électrique régnant dans le spectromètre ainsi que la longueur de celui-ci. Ces valeurs permettent de remonter à la vitesse des différents fragments, à partir du temps de vol et de la position du point d'impact mesurés sur le détecteur. D'autre part, la position et le diamètre du faisceau projectile et du faisceau de molécules cibles sont obtenus.

Spectromètre NO_2 "condition de focalisation en temps":

Pour obtenir des temps de vol absolus, il faut soustraire au temps mesuré un décalage systématique que nous appelons T_{offset}. Or nous avons vu que le temps de vol d'un ion dans ce type de spectromètre comporte deux termes: l'un dépendant de la vitesse initiale et contribuant à la largeur des pics de masse, l'autre, du rapport masse sur charge de l'ion et déterminant la position de ces pics. C'est de la position de certains de ces pics de masse, associés à des fragments identifiés, que la valeur du champ électrique et de T_{offset} sont obtenues.

La détermination de la projection du point de collision dans le plan du détecteur est nécessaire pour calculer des vitesses des fragments dans le plan du détecteur. L'extension spatiale de cette projection nous permet de déterminer le volume de collision correspondant à la zone de recouvrement du jet supersonique et du faisceau d'ions projectiles.

Spectromètre HDO "condition focalisation en position 3D":

L'avantage de ce dispositif est que chaque voie de dissociation peut être complètement séparée des autres en tirant avantage de la conservation d'impulsion, avantage rendu possible par la détection complète de tous les fragments. Le point de collision peut être calculé à posteriori pour chaque événement à partir des mesures. Par conséquent, la résolution en position n'est pas limitée par le volume de point collision, comme dans le cas précédent, mais uniquement par la résolution finale du détecteur PSD (300μm). Comme on pouvait s'y attendre, la résolution en énergie cinétique s'en trouve grandement améliorée jusqu'à atteindre une valeur aussi faible que 100meV.

Résultats NO_2

L'objectif de ce travail est d'étudier le rôle de la géométrie d'une molécule sur la dynamique de sa fragmentation en comparant le cas d'une molécule tri-atomique coudée, NO_2, et à celui d'une molécule linéaire, CO_2, dont les résultats sont présentés dans l'introduction.

La dissociation de l'ion moléculaire NO_2^{3+} en trois fragments ($N^+/O^+/O^+$) montre clairement que la dynamique de la fragmentation est de type "concertée synchrone", comme nous l'avions montré dans le cas de la molécule linéaire $CO_2^{3+} \rightarrow C^+ + O^+ + O^+$. Les différences géométriques ont des effets significatifs et forts sur la dynamique de dissociation: dans le cas de NO_2, l'atome central, l'azote, participe fortement dans le bilan de quantité de mouvement.
Le diagramme de Newton résume graphiquement ce bilan (figure f-3). La quantité de mouvement emportée par chacun des deux fragments O^+ est semblable à celle mesurée dans le cas de CO_2^{3+}. Cependant, le fragment central N^+ a une valeur finie (comprise entre 100-200a.u.) dans la direction opposée aux deux fragments O^+, contrairement du dioxyde de carbone pour lequel le fragment C^+ est pratiquement au repos (figure f-1a). La distribution d'énergie cinétique emportée par les fragments du NO_2^{3+} est centrée autour de 35 eV. La résolution expérimentale est ~250meV (figure f-4).

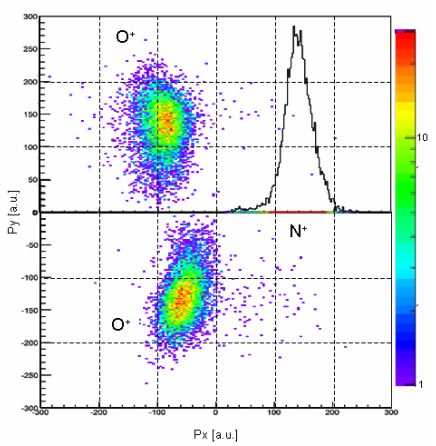

Figure f-3 Diagramme de Newton de la fragmentation de NO_2 en $N^+/O^+/O^+$. La quantité de mouvement N^+ est choisie comme axe P_x, le O^+ le plus énergétique est placé dans la partie supérieure du diagramme (P_y>0)

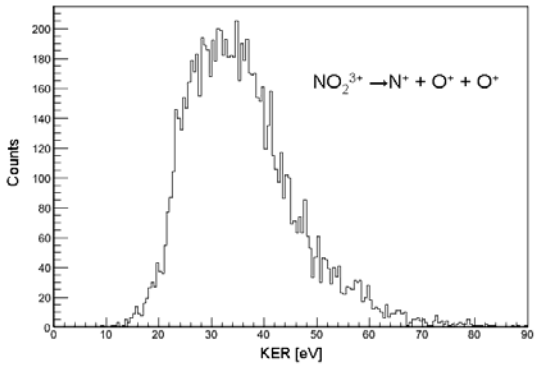

Figure f-4 Distribution de KER de la voie $N^+/O^+/O^+$ sur NO_2

D'autre part, le cas de la dissociation du dication NO_2^{2+} montre plusieurs structures spécifiques additionnelles. Dans le cas de la dissociation à deux corps $NO_2^{2+} \rightarrow NO^+ + O^+$, les événements sont aisément identifiés et séparés. La distribution de KER mesurée pour cette voie est en bon accord avec les travaux précédents. Par contre, lors de la dissociation complète du dication ($NO_2^{2+} \rightarrow N^+/O^+/O$), il n'est pas possible de séparer parfaitement, par les méthodes d'analyse de données conventionnelles, les événements associés à cette voie de ceux associés aux voies à trois corps provenant d'ions moléculaires plus chargés. Cependant, les différences de KER correspondant à ces voies de fragmentation ont permis cette séparation: la contribution de la voie de dissociation ($N^+/O^+/O$) est dominante pour des valeurs de KER inférieures à 20eV (figure f-5). Dans cette région, nous avons observé trois dynamiques de dissociation différentes:

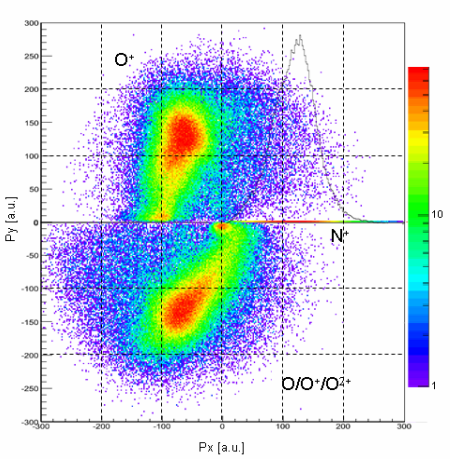

Figure f-5 Diagramme de Newton de la fragmentation de NO_2 en coïncidence N^+/O^+. La quantité de mouvement N^+ est choisie comme axe P_x, le O^+ détecté est placé dans la partie supérieure du diagramme (P_v>0)

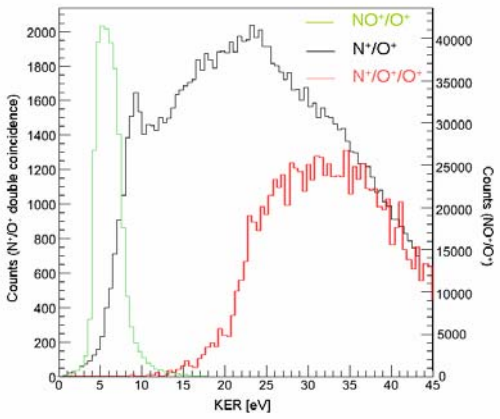

Figure f-6 Distribution de KER de la voie de coïncidence N^+/O^+, NO^+/O^+, $N^+/O^+/O^+$ sur NO_2

1. L'atome d'oxygène neutre est émis vers l'ion azote.
2. L'atome d'oxygène neutre est pratiquement au repos et la quantité de mouvement est partagée entre les ions azote et oxygène.
3. Les fragments chargé O^+ et neutre O peuvent avoir les mêmes quantités de mouvement et leur somme est compensée par l'ion azote N^+.

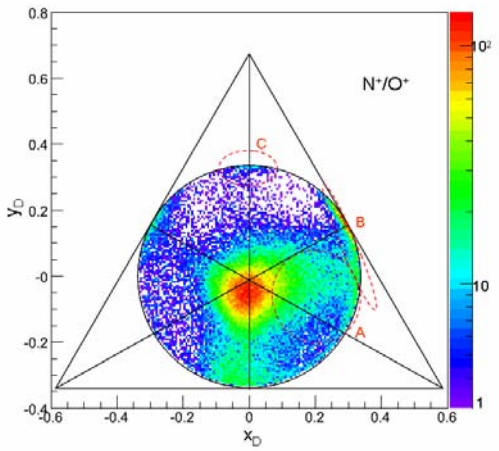

Figure f-7 Diagramme de Dalitz de la fragmentation de NO_2 en coïncidence N^+/O^+.

La représentation dite de "Dalitz" donne une autre confirmation pour ces scénarios. La figure f-7 montre le diagramme de Dalitz où sont reportés tous les évènements associés à la détection en coïncidence des ions N^+ et O^+. La distribution la plus importante au centre de la figure correspond au cas de la fragmentation concertée synchrone de l'ion moléculaire NO_2^{3+}. La région A n'apparaît que pour les valeurs de KER inférieures à 20eV (voir figure f-6). Elle correspond à l'extension asymétrique des liaisons N^+-O et de N^+-O^+.

La région B, visible à la périphérie du cercle, indique que l'oxygène neutre n'a aucune quantité de mouvement. La région B est associée au pic situé entre 5-15eV sur la distribution d'énergie cinétique libérée (KER).

Enfin, La région C correspond au cas où les deux fragments oxygène, neutre et simplement ionisé, ont des quantité de mouvement pointant dans la direction opposée à celle du fragment N^+, lançant supposer que la dissociation implique une étape intermédiaire du type (N^+/O_2^+). Le KER correspondant à cette observation est dans l'intervalle 7.5-20eV (principalement 10-15eV).

En conclusion, la dissociation à trois corps de la molécule NO_2 doublement ionisée conduit à une dynamique complexe dans laquelle la quantité de mouvement se répartit indifféremment sur les trois fragments, contrairement au cas plus simple d'une molécule linéaire. C'est évidemment la signature d'une fragmentation de type «concerté asynchrone».

Résultats HDO

Un des intérêts principaux de ce travail est de comparer le mécanisme de dissociation du dication HDO^{2+} induit par impact d'ion lourd rapide avec les prédictions théoriques s'appuyant sur les surfaces d'énergie potentielle (Potential Energy Surface, PES) de cet ion moléculaire. Les deux voies de dissociation de l'ion moléculaire HDO^{2+} ($H^+ + OD^+$ et $D^+ + OH^+$), ainsi que celles des deux isotopomères symétriques D_2O ($D^+ + OD^+$) et H_2O ($H^+ + OH^+$), sont analysées aux vues des résultats du calcul. Ces quatre voies de dissociation de ces dications peuvent être clairement séparés par notre technique expérimentale, comme le montre bien la carte de coïncidence présentée ci-dessous (figure f-8).

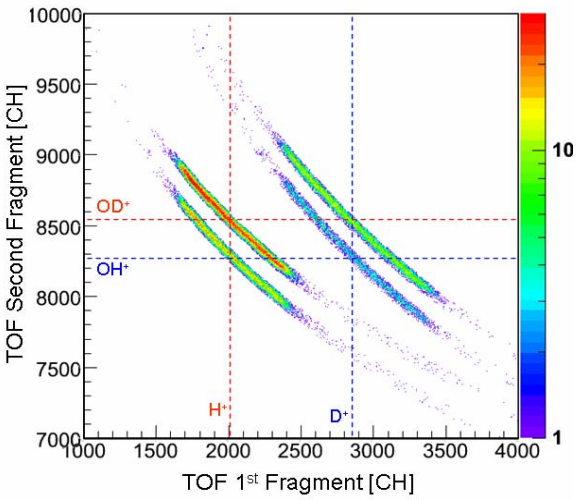

Figure f-8 Carte de coïncidence des premier et deuxième ions détectés lors de la fragmentation des dications de la molécule d'eau, après nettoyage par le filtre en position 3D.

La fragmentation du HDO^{2+} fait l'objet d'une attention importante dans de nombreuses expériences récentes du fait de la forte sélectivité isotopique de la rupture des liaisons OH et OD. Deux valeur du rapport de branchement $(H^+ + OD^+)/(D^+ + OH^+)$ ont été mesurées par des méthodes expérimentales différentes et sont en désaccord de 25% (6,5 ± 0,5 [réf. V.1] et 5,2 ± 0,3 [réf. V.2). Dans ce travail de thèse, nous avons obtenu une valeur expérimentale intermédiaire. Utilisant une technique d'imagerie ainsi qu'un spectromètre de temps de vol particulièrement adapté à cette expérience, il a été possible d'avoir un accès direct aux distributions d'énergie cinétique emportée par les fragments (KER) et à la proportion de chacune des deux voies avec une haute résolution. Il s'agit de la première expérience permettant l'étude simultanée de tous les isotopomères de la molécule d'eau. En effet, la dissociation de H_2O^{2+} et de D_2O^{2+} ont été analysées de la même manière que HDO^{2+} afin d'être directement comparables. Les proportions des différents fragments et les rapports de branchement dans le cas de l'impact d'ions S^{15+} de 13,7MeV/u sont présentés dans le tableau1. La rupture de la liaison OH s'avère être 5,7 fois plus probable que celle de la liaison OD.

Voie de dissociation	Nombre d'événements	Proportion de la voie
$H^+ + OD^+$	29984	5,7 ± 0,1
$D^+ + OH^+$	5294	1
$H^+ + OH^+$	16830	3,2 ± 0,1
$D^+ + OD^+$	17222	3,3 ± 0,1

Tableau 1 Les proportions des différents fragments et les rapports de branchement dans le cas de l'impact d'ions S^{15+} de 13.7MeV/u

Un autre aspect important de la fragmentation à deux-corps de HDO^{2+} est la différence des valeurs moyennes de l'énergie cinétique libérée (KER) par chacune des deux voies de dissociation. Les valeurs obtenues lors d'un précédent travail sont respectivement 6eV pour la voie $D^+ + OH^+$ et 7eV pour la voie $H^+ + OD^+$ avec une résolution de 0,5eV. Nous avons amélioré la précision sur la mesure de ces valeurs pour chacune des quatre voies de dissociation des dications de l'eau. Les valeurs moyennes de KER sont les suivantes : 6,5±0,1eV pour les trois voies $D^+ + OH^+$, $H^+ + OH^+$ et $D^+ + OD^+$, valeur conforme au résultat de Siegmann et al [réf.V.3] pour la voie de $H^+ + OH^+$, et 6,9±0,1eV pour la voie $H^+ + OD^+$ (figure f-9).

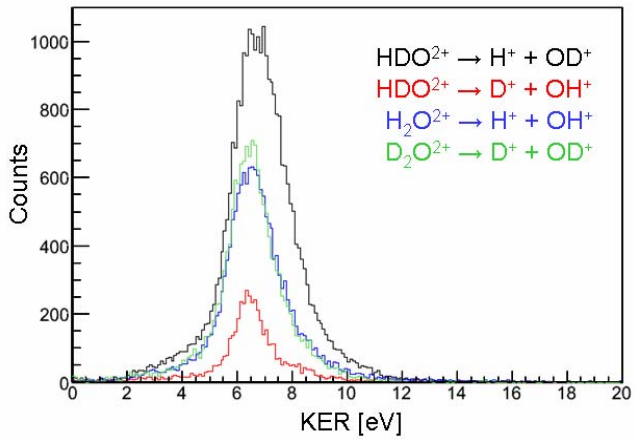

Figure f-9 Distribution de KER des voies de fragmentation H^+/OD^+, D^+/OH^+ pour HDO^{2+}, H^+/OH^+ et D^+/OD^+ pour HO_2 et DO_2, respectivement.

Les caractéristiques principales du processus sont bien reproduites par un calcul semi-classique. En effet, le rapport de branchement théorique de 7,2 est en bon accord avec la valeur expérimentale de 5,7. De plus, il est remarquable que les écarts entre les valeurs moyennes de KER des différentes voies de fragmentation soit bien reproduite. Néanmoins, la simulation ne tient compte que de l'état fondamental de l'ion moléculaire. La différence observée entre l'expérience et le calcul peut éventuellement venir du fait que la collision peut peupler un ou plusieurs états électroniques excités du dication.

Pour tester cette hypothèse, nous avons réalisé une autre expérience avec un ion projectile de basse énergie cinétique: Ne^{10+} à 10keV/q. Dans ce régime de vitesse de collision, l'ionisation de la molécule se fait par l'intermédiaire de la capture d'électrons par le projectile. L'idée sous jacente est de tenter d'obtenir le dication dans un état électronique différent en le produisant par l'intermédiaire de processus différents : la capture électronique ou l'ionisation directe. Nous avons obtenu des rapports de branchement ainsi que des distributions d'énergie cinétique très similaires à ceux mesurés pour le projectile à haute vitesse et ainsi donc pas de différence notable.

§ I Introduction

Numerous studies have already been devoted to molecular fragmentation. In the case of ion-induced fragmentation, one can address many fundamental aspects of molecule. In CIRIL laboratory, ion-atom and ion-molecule collision have been investigated by using specially designed supersonic gas jet apparatus and multi-charged ion produced by GANIL for a decade. Besides, the recent evolution of experimental technique, called COLTRIMS which is now ubiquitous in the field of atomic physics research, opened doors for further studies of spectroscopy. The study of the fragmentation dynamics of triatomic molecule is, therefore, one of the grand sum of these achievements.

I.1 Fragmentation Process

The analysis of molecular fragmentation is based on the Franck-Condon principle. The qualitative picture of the principle is illustrated in figure I-1. This illustration shows a ground state molecular energy curve and two dissociative electronic states of diatomic molecule AB. The duration of interaction between a fast multi-charged ion and a target molecule is estimated to be order of the 10^{-18}-10^{-17} second which is quite shorter than molecular characteristic times: vibration (10^{-14}-10^{-12}) and rotation (10^{-12}-10^{-9}). As a result, the nuclear locations remain unchanged during electronic transition so the ionized molecule keeps the equilibrium internuclear distance of the neutral molecule. In a second step, since most of multiply charged molecular ions are not stable, nuclear motion starts off along the potential energy curves. When resulting ionized molecule $(AB)^{q+}$ dissociates into A^{q1+} + B^{q2+} (q=q1+q2), potential energy difference between transient molecular ion state $(AB)^{q+}$ and final state (A^{q1+} + B^{q2+}) is transferred into kinetic energy shown as E_{k1} in the figure, named Kinetic Energy Release (KER). Thus by measuring the KER distribution, it is possible to obtain the informa-

tion on the fragmentation process of the molecule corresponding to the excited states of the molecular ion.

In the case of diatomic molecules, the charge of the transient molecular ion is generally shared equally into two fragments [ref. I.1-3]. This is because the electron rearrangement in the transient molecule occurs in a much shorter time ($\approx 10^{-16}$) than the dissociation process.

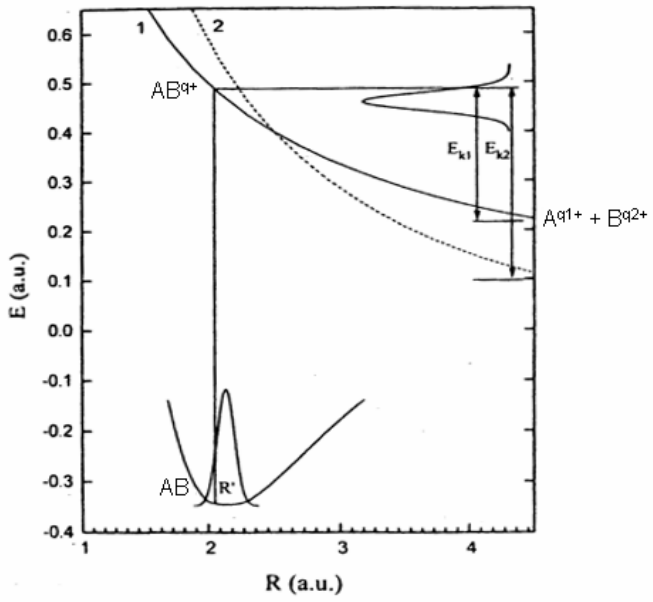

Figure I- 1 Schematic potential energy curves of a diatomic molecule.

In the early experiments on diatomic molecular fragmentation, the mean KER value could only be estimated due to the low resolution and results were in fair agreement with simple Coulomb Explosion Model (CEM) predictions [ref.I-4, 5 for example]. In this model, the KER in the diatomic molecular fragmentation into ($A^{q1} + B^{q2}$) is assumed to be due to the Coulomb repulsion energy:

$E_{\mathrm{ker}} = \dfrac{14.4 q_1 q_2}{r}$ [eV], where r [Å] is the internuclear distance of the neutral molecule at equilibrium.

More recently, the KER distribution have been measured with better resolution both high energy (1-100MeV) and low energy (several keV/q) ion impact. The results obtained by high energy ion impact experiments show that the mean KER values disagree with the predictions of CEM and include high energy components [ref. I.3,6,7]. These high energy components were attributed to highly excited molecular ions. At low energy experiments, contrary, the reaction channels and mean KER values lower than the CEM predictions have been determined [ref.I.8,9]. Furthermore, the measured KER values were well accorded with the theoretical results from potential energy curves obtained a quantum chemical calculation. In CIRIL, both low energy and high energy ion induced fragmentation of CO molecule have successfully conducted. The resolution of KER has been im-

proved down to 250 meV leading to clear structures on the spectra. These structures have been interpreted by the use of "exact" molecular potential energy curves [ref. I.10]. These results indicate that the fragmentation process is completely driven by dissociative excited states of the transient molecular ion produced during the collision.

The reactions of triatomic molecules are, however, not able to be described by such a simple picture. Following potential energy "surfaces", no more simple curves, many reaction channels are involved in the fast ion-molecule collision. The reaction channels which end into complete three-body dissociation may hold the different scenarios. According to Maul and Gericke [ref.I.11] terminology and its expansion proposed by Hsieh and Eland [ref.I.12], the different fragmentation mechanisms are distinguished into three types as follows:

1) Pure sequential fragmentation
2) Synchronous concerted fragmentation
3) Asynchronous concerted fragmentation

The first case corresponds to two independent two-body dissociation reactions. In other word, the first atomic fragment has no interaction with the other fragments when the second dissociation step of the intermediate diatomic fragment takes place:

$$(ABC)^{q+} \rightarrow A^{q1+} + (BC)^{q2+} \qquad \text{then}$$
$$(BC)^{q2+} \rightarrow B^{q3+} + C^{q4+}$$

The second fragmentation type is defined as the one for which the two bond breakages occur simultaneously and with a symmetric behavior.

$$(ABC)^{q+} \rightarrow A^{q1+} + B^{q2+} + C^{q3+}$$

Then the third one includes reactions from instantaneous dissociation via asymmetric stretch to non pure sequential dissociation, meaning a second step influenced by the primary fragment.

$$(ABC)^{q+} \rightarrow A^{q1+} + (BC)^{q2+}$$
$$\rightarrow A^{q1+} + B^{q3+} + C^{q4+}$$

The following discussion in the present thesis for three-body fragmentation relies on this categorization.

I.2 Experimental Backgrounds

The recent growth in research on atomic and molecular physics field has strongly benefited from the recent evolution of the Recoil Ion Momentum Spectroscopy (RIMS) technique[1] [ref.I.13]. This method, originally designed for ion-atom collision experiments [ref.I.14], is now widely used either for electron impact [ref. I.15 for review], synchrotron radiation [ref.I.16 for review], or femto-second laser [e.g. ref.I.17] experiments. Apart from the use of supersonic jet target, one of the most important things among numerous technical developments is the multi-hit detection of particles. This "breakthrough" offers unprecedented opportunities for coincidence measurements of fragments from a molecule. The spectrometer can be modified easily to different specifications as well. The time-focusing condition allows to reconstruct momentum components even for undetected particles [ref.I.18]. Position-focusing condition avoids the problem of the resolution limitation due to the volume of the collision region [ref.I.19,20]. Another significant development which helps to obtain the complete kinematics of molecules is the imaging technique. Using a 2D position sensitive detector while the longitudinal velocity is deduced by time of flight measurement, molecular coordinates can be reconstructed in a simple manner.

The localised target, coincidence, multi-hit detection and imaging techniques allow now to investigate the mechanisms of molecular fragmentation with kinematically complete data set.

I.3 Previous Results and Scopes of Present Works

I.3.1 Fragmentation Dynamics

For the last few years, a number of studies have been devoted to polyatomic molecular fragmentation with RIMS techniques. Most of experimental studies have approached molecular characteristics through photoionization. After the successful investigation of diatomic molecules, our group has decided to go further taking advantage of fast ion impact, i.e. the momentum transfer between the projectile ion and target molecules is negligible. Because of this characteristics, ion induced fragmentation can give direct information of momentum sharing among molecular fragments in different dissociation channels which cannot be done easily with laser excitation since fragments may start moving during the light pulse if too long.

[1] Or, COLTRIMS especially for the COLd Target experiment.

The linear triatomic molecule CO_2 was the first candidate [ref.I.21] in order to reveal the role of an internal degree of freedom, such as stretching. A slight bend angle of the triatomic molecule leads the fragments to move in a plane, rather than on an axis as in the case of diatomic molecules. The main results obtained from the previous experiment concerned the dissociation channels of triply and doubly ionized molecules corresponding to the main "island" in the figure I-2:

$$CO_2^{3+} \rightarrow C^+ + O^+ + O^+$$

$$CO_2^{2+} \rightarrow C^+ + O^+ + O$$

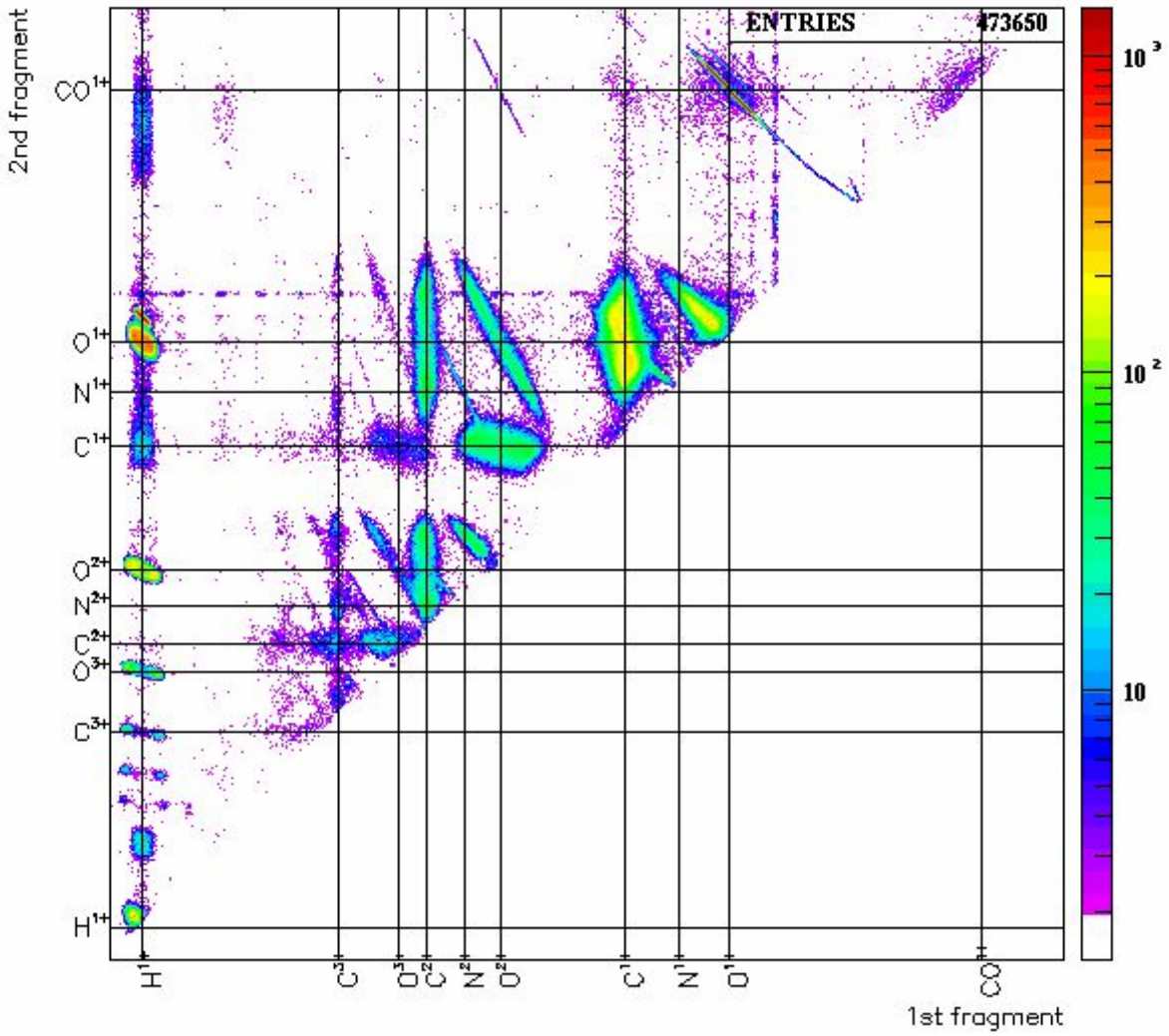

Figure I- 2 Coincidence Map of 1st and 2nd fragments from CO_2 collision with 8MeV/u Ni^{24+}

In order to show the shared momentum balance among the fragments, Newton diagram, representing the momentum balance in the molecular frame, is an usual way to present it. Following to the definition (section I.1), these momentum vector coordinates can be used to discriminate the dis-

sociation process. In figure I-3 and I-4, the center atom C^+ momentum direction is chosen as the x-axis while the more energetic/detected O^+ fragment defines the positive y axis (see section IV.3 for detail).

The Newton diagram corresponding to triple ionized dissociation channel, on figure I-3, shows a symmetric emission of the two oxygen fragments while the carbon ion has smaller momentum (0-100 a.u.) in the molecular frame. This is characteristic of a synchronous concerted fragmentation. Due to the simultaneous bond breakages of C-O, the center atom ion C^+ stays nearly at rest.

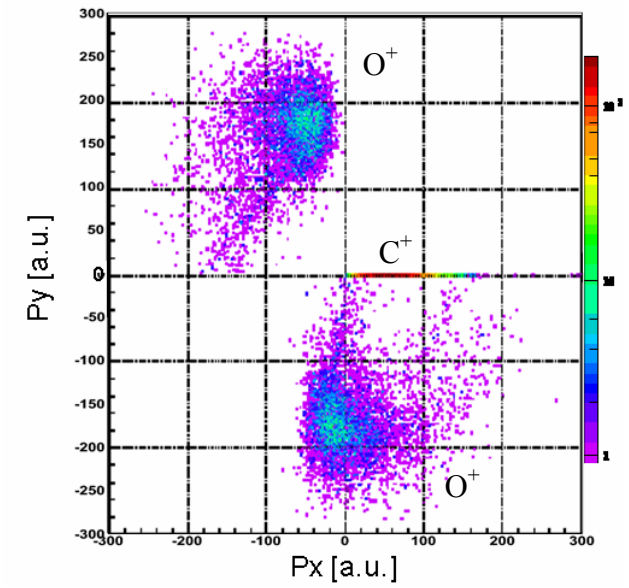

Figure I- 3 Newton diagram of the fragmentation of CO_2^{3+} forming $C^+/O^+/O^+$.

The case of CO_2^{2+} dissociation is more complex. Since the neutral fragments can not be detected, one has to separate the relevant events ($C^+/O^+/O$) form double coincidence measurements (C^+/O^+) including "incomplete" events from ($C^+/O^+/O^+$) and ($C^+/O^+/O^{2+}$), etc (figure I-4.a to I-4.b, see figure I-5 for additional information). The figure I-4.b shows no features corresponding to the synchronous concerted fragmentation. What one can observe here is that the neutral O fragment is emitted towards the C^+ momentum direction. This fact enables to assume that the dissociation proceeds through the intermediate step $CO^+ + O^+$. Moreover, comparing the KER distributions of the dissociation channel which ends into $CO^+ + O^+$ and $C^+ + O^+ + O$, there is a certain threshold where the complete dissociation starts to be observed and become dominant (figure I-6). A simple model could be evoked for this dissociation channel relying on an "asymmetric stretch picture". The first bond break leads to (C^+-O) and O^+, then due to the recoil of C^+, the internal vibrational energy of the molecular fragment CO^+ increases. This transferred energy from the first step introduces the threshold effect observed in the KER distribution: if the energy is larger than the CO^+ binding energy, the dissociation ends into complete three-body fragments ($C^+/O^+/O$), otherwise two-body fragmentation (CO^+/O^+) is detected. Consequently the process of the CO_2^{2+} fragmentation is the non-pure sequential categorized in asymmetric concerted fragmentation.

In order to go further, these interpretations have to extend into a more general triatomic molecule case with a bending angle. Thus NO_2, a bent molecule having similar mass ratio to CO_2 has been considered to be an ideal candidate for the next step. The molecular characteristics of equilibrium CO_2 and NO_2 are shown in table I-1.

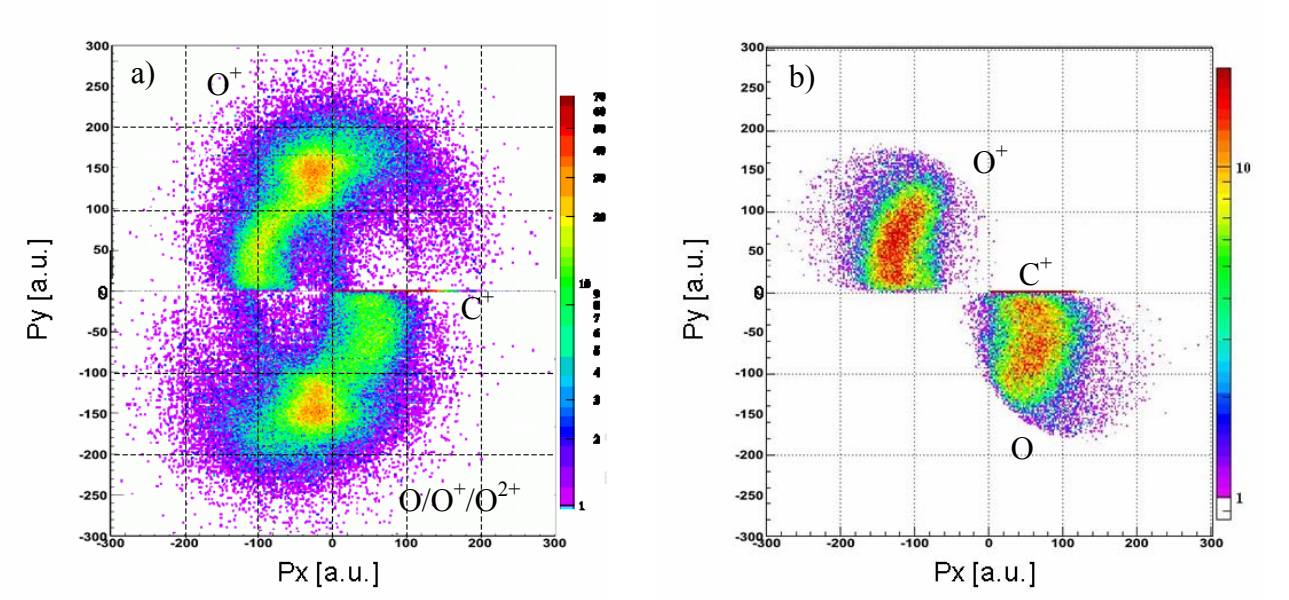

Figure I- 4 Newton diagram of a) all measured C^+/O^+ double coincidence events consisting mainly in ($C^+/O^+/O$), ($C^+/O^+/O^+$) and ($C^+/O^+/O^{2+}$) dissociation channels b) separated $C^+/O^+/O$ dissociation channel from a).

A particular attention is given to the dication, for which the fragmentation scenario may become even more complicated. The rotation of the intermediate molecular fragment should participate more in the dissociation energy sharing among all degrees of freedom than for a linear molecule.

The mean KER value when the dissociation of NO_2^{2+} results in the formation of the charged pair (NO^+/O^+) has been first measured to be 8.03 eV by R. G. Cooks et al. in 1974 [ref.I.22] with electron impact. Then in PIPICO (PhotonIon-PhotonIon-COincidence) and PEPIPICO (PhotonElectron-PhotonIon-PhotonIon Coincidence) double photo-ionization measurements, total KER of 8.6 and 7.1±1 eV have been measured, respectively by J.H.D. Eland et al. in1987 and 1988 [ref.I.23,24]. Authors also estimated an energy release of 6.1±1 eV and 6.3±3 eV for ($N^+/O^+/O$) and ($N/O^+/O^+$) dissociation channels, respectively. At the same period, theoretical calculations have also been reported by the same authors [ref.I.25]. More recently, Masuoka and Kobayashi [ref.I.26] have measured same dissociation channels as Eland et al by PIPICO measurements in better resolution. However, these studies focus on the thresholds of double ionization and dissociation, electronic states, or partial cross sections, but not at the dynamics of the fragmentation. The present study will

then give the first direct results of the NO_2^{2+} fragmentation dynamics. Moreover, the systematic understanding of geometrical contribution on molecular fragmentation may hopefully be used as a probe of the electric processes involved, in such fields of cluster fragmentation or radiation damage.

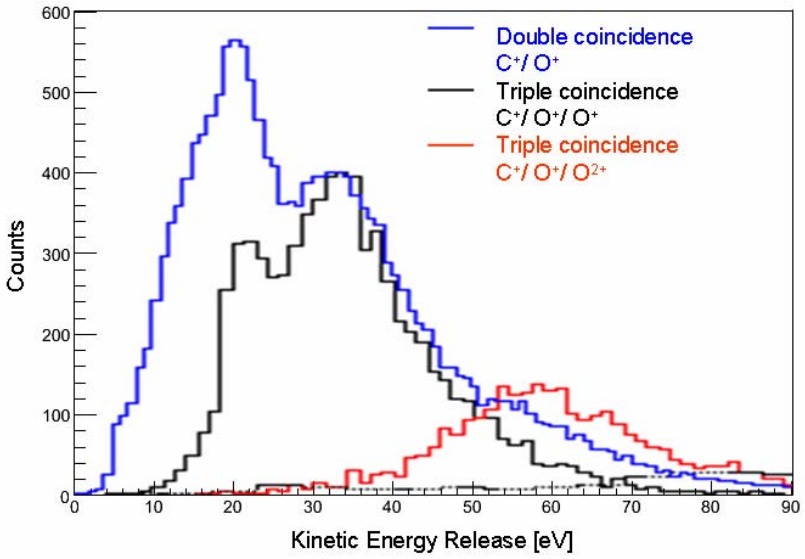

Figure I- 5 Comparison of three KER distributions obtained by double coincidence event C^+/O^+ (blue) and completely identified triple coincidence events $C^+/O^+/O^+$ (black) and $C^+/O^+/O^{2+}$ (red) dissociation channels. To emphasize the contribution of $C^+/ O^+/ O^+$ and $C^+/ O^+/ O^{2+}$ channels on double coincidence spectrum, peak heights of both spectra are adjusted arbitrarily.

	Mass	r (A-O) [Å]	Bond	angle [deg.]
CO_2	44	1.163	Two double bonds	172
NO_2	46	1.197	One unpaired electron	134

Table I- 1 Characteristics of molecule CO_2 and NO_2 in equilibrium ground state.

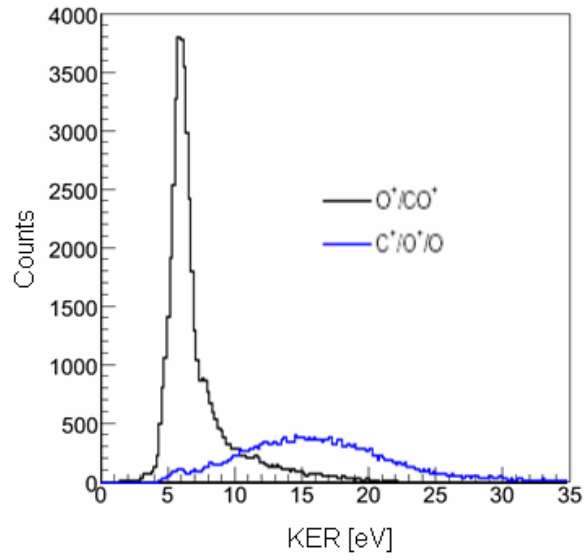

Figure I- 6 KER distributions of double ionization dissociation channel forming CO^+/O^+ (black) and $C^+/O^+/O$ (blue).

I.3.2 Branching Ratio of HDO^{2+} Dissociation

Another way to get information on triatomic molecular ion potential energy surfaces is to take advantages of isotopomers. Asymmetric HDO^{2+} deuterated water dication fragmentation has been given special attention in recent experiments [ref.I.27,28] and particularly to the two-body fragmentation channel leading to an atomic and a molecular ion as final products. The exciting question is about the nature of the atomic fragment. Is it equivalent to get H^+ or D^+ as the atomic fragment? In other words, is the OH bond weaker than the OD bond? The answer is that a strong isotopic preference has been observed in favor of the cleavage of OH bond over OD bond in HDO dication dissociation. Two values have been measured for the branching ratio $(H^+ + OD^+) / (D^+ + OH^+)$ which disagree by 25% ([ref. I.27]: 6.5 ± 0.5, [ref. I.28]: 5.2 ± 0.3). In order to find out the underlying process leading to this selective behavior, calculations of this ratio have also been performed, either semi-classical [ref. I.27] or wave-packet propagation calculations [ref. I.28], both restricted to the lowest HDO^{2+} potential energy surface.

Aiming to test them in details and understand the reason for this strong isotopic selection, we measured branching ratio and Kinetic Energy Release (KER) distributions with a high resolution. Taking advantage of the detection of both fragments, we used a COLTRIM spectrometer without the field-free region of the usual Wiley-MacLaren configuration. This allows to decrease the extracting electric field down to 20V/cm and thus to improve the KER resolution (see section II.3.4).

In order to be as complete as possible, H_2O and D_2O were analyzed in the same way as HDO giving a direct calibration of relative cross sections within the same experiment.

§ II Experimental Specifics

To investigate the dynamics of fragmentation process, primary key information is the Kinetic Energy Release (KER) distribution of the system. In recent years our group has achieved high resolution measurement of KER using the Recoil Ion Momentum Spectroscopy technique [ref. II.1-3].

Our experimental setup consists in three main parts: 1. projectile ion provided by GANIL beam lines, 2. target supersonic molecular gas jet apparatus attached to the main chamber and 3. recoil ion and electron spectrometer with position sensitive detector on each ends. The improved new acquisition system is also described in this chapter.

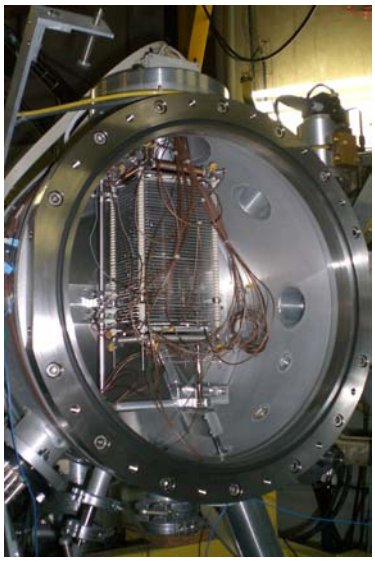

Figure II- 1 Photograph of Recoil Ion Spectrometer in the main chamber.
The projectile ion comes from left-hand side and collides with target molecules from a supersonic jet generator installed on the backside of the reaction chamber.

II.1 Projectiles: Highly Charged Ions

II.1.1 High Energy Projectile Ions from GANIL Facility

Most of our experiments have been conducted at the SME beam line located at GANIL accelerator facility. SME means medium energy exit (Sortie Moyenne Energie) designed for interdisciplinary research (atomic and molecular physics, solid state physics). As illustrated in figure II-2, projectile ions are produced by an ECR ion source and pre-accelerated by a compact cyclotron(C01 or C02), then are injected into the first Cyclotron with Separated Sectors (CSS1) for acceleration up to 4 to 13MeV/amu. Since these cyclotrons have the same specifications, the charge state of extracted ion has to be changed before going into the second accelerator (CSS2) to be accelerated further. Therefore after the exit of CSS1, extracted ions pass through a thin carbon foil for charge stripping. After this stripper, one charge state is sent into SME beam line while another one is directed to CSS2 for high energy (24-96MeV/amu) acceleration. Due to the function principle of the cyclotron accelerators, GANIL provides a pulsed beam which frequency depends on the type and the energy of the circulating ion.

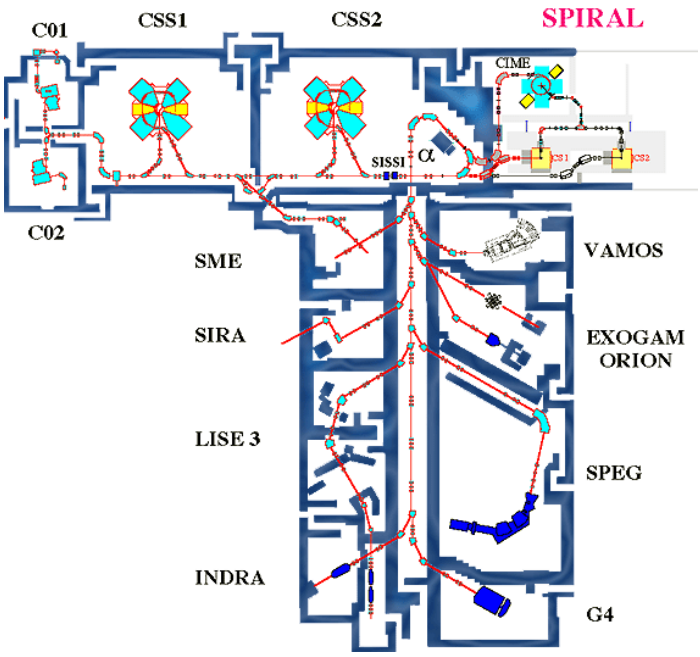

Figure II- 2 GANIL beam facility

In the present work, we used 13.7MeV/amu S^{15+} for one of HDO experiments and 4.7MeV/amu Ne^{8+} for NO_2 experiment as projectile ions[1]. These high energy highly charged ions enable us to observe directly the dynamics of molecular fragmentation. Since the velocities of projectile ions are so high, the momentum exchange between projectiles and target molecules are neg-

[1] Velocities in atomic units are 23.4a.u and 13.7a.u., respectively.

ligible. For all experiments, the beam intensity is adjusted to have an average number of coincidence events around 2000cps in order to avoid random coincidences.

II.1.2 Low Energy Projectile Ions from ARIBE[2] Facility

One of the HDO fragmentation experiments has been conducted at ARIBE beam line. This low energy facility located at GANIL has started providing low energy ion beams since 2005. There are 7 experimental areas in total as showed in figureII-3 for conducting heavy ion experiments. Highly charged heavy ions with high intensity are provided from an ECR ion source and extracted up to 25keV/q.

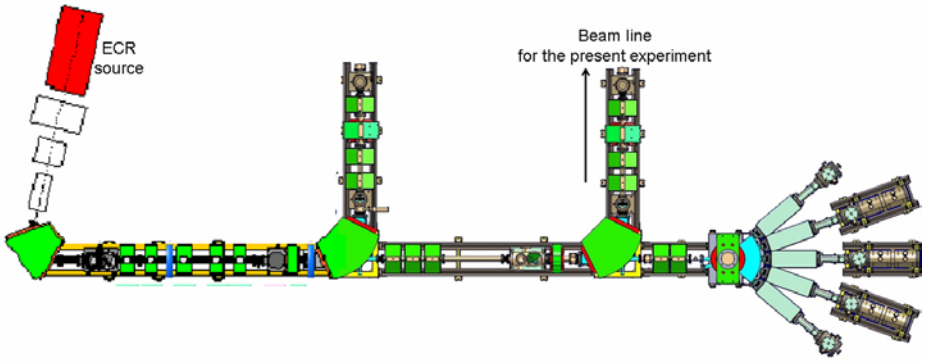

Figure II- 3 ARIBE beam line

In contrast with high energy ion impact, we can no more neglect the momentum transfer between the target and the projectile during collision. Using the position sensitive detector (see II.4), we have observed the charge-exchange on the projectile 1 meter downstream after collision. The projectile delivered to the line L4 passes through two collimators of 10mm in diameter placed at 1.5m and just before the reaction chamber respectively. Then inside the chamber, a third collimator cuts the beam to 0.6mm in diameter to let it cross the collision point. After collision, the multi-charged projectile ions are bent and charge separated by passing through electrostatic deflector plates. Then a drift tube, equipped with a Position Sensitive Detector at the end, is installed after the reaction chamber. Its angle can be modified easily to be adjusted to the chosen projectile charge state [ref. II.2, 4].

We have used Ne^{10+} with an energy of 17keV/q, i.e. 0.56a.u. in velocity. The deflectors are biased to -310V for the upper one and of +310V for the other in order to be able to separate differ-

[2] Accélération de Recherche avec les Ions de Basse Energie

ent ion charge states. The detector is set 10cm higher than the beam line in the case of Ne^{9+} or lower charged projectile.

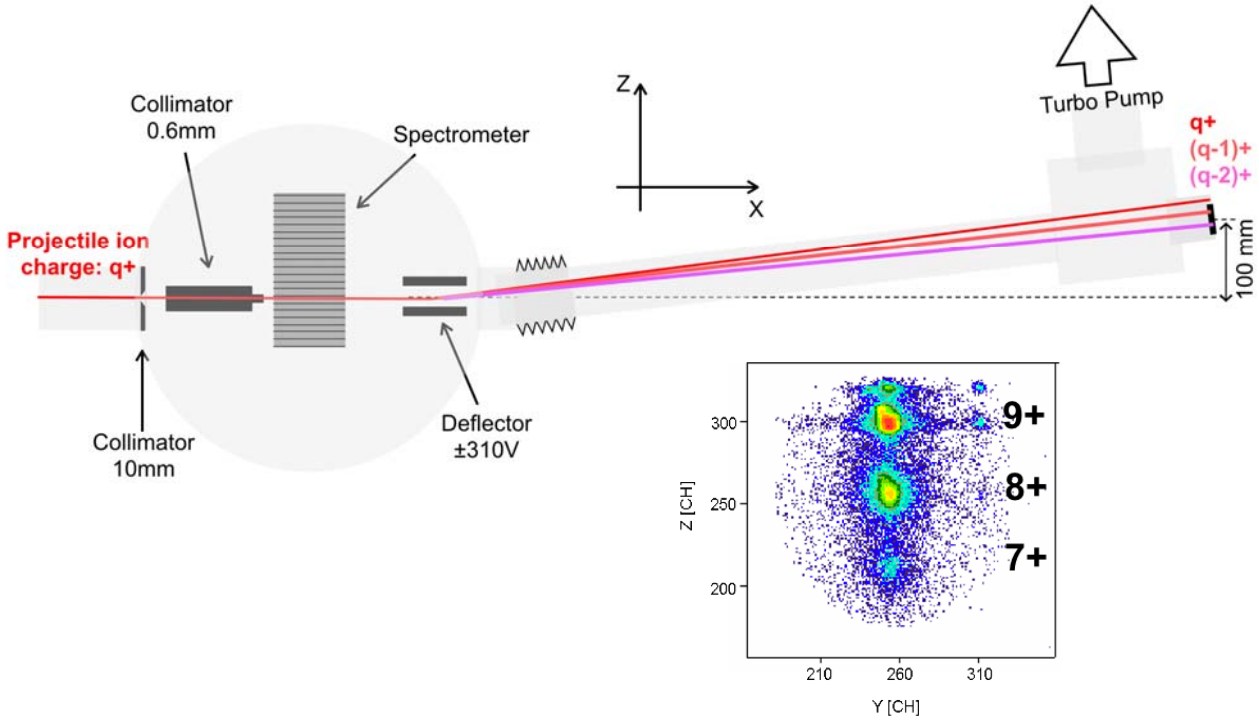

Figure II- 4 Schematic drawing of the projectile detection principle and a typical detector image for Ne^{10+} projectile after a charge exchange reaction: Ne^{9+}, Ne^{8+} and Ne^{7+} are detected on the detector**.**

II.2 Target Molecules: Supersonic Jet

II.2.1 Principle and Setup

The cold and dense gas target is produced by specially designed supersonic gas jet apparatus (Campargue [ref. II.5, 6]). The use of supersonic gas jets allows to achieve high resolution measurements that would be impossible with a standard gas cell target at room temperature. Indeed, a small sized target and a reduced thermal motion are necessary for our imaging technique (see following sections).

The supersonic jet gas is produced by the expansion from a strong pressure P_0 through a small nozzle to a low pressure stage (Figure II-6). During this adiabatic expansion, the initial disordered momentum is transformed into the directed momentum along the nozzle axis. The supersonic gas jet bordered by a shock-front is formed. The gas jet flowed in the first stage is extracted by a sharp skimmer placed in the "zone-of-silence" without breaking its characteristics. To obtain reasonable gas jet properties, the product of $P_0 \cdot D$ should be larger than 1 mbar · cm, where D is the nozzle di-

ameter [ref. II.1, 7]. Practically, the performances of gas jets are mainly fixed by the pumping speed in the first stage and the distance between nozzle and skimmer at the exit to the collision chamber.The nozzle position is easily adjustable in order to obtain the best performance for different gas species and driving pressures. Then a high quality jet goes into the collision chamber through a collimator at the exit of the second stage. The second stage has an important role in maintaining a good vacuum in the reaction chamber.

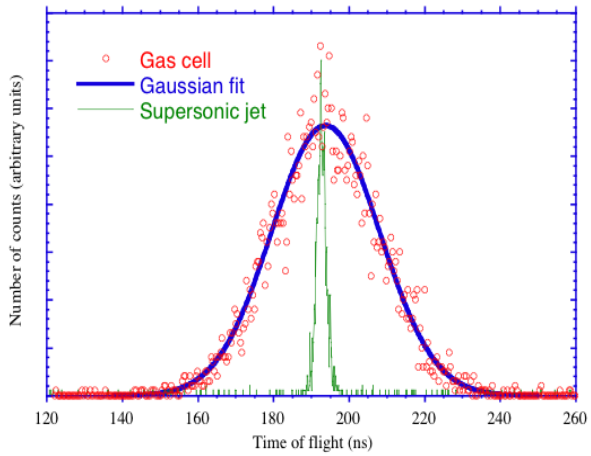

Figure II- 5 Comparison of Ar^+ flight time peaks obtained with a gas cell (red circle) and a supersonic gas jet (green line). The width of these distributions is due to the initial thermal motion of the target atoms.

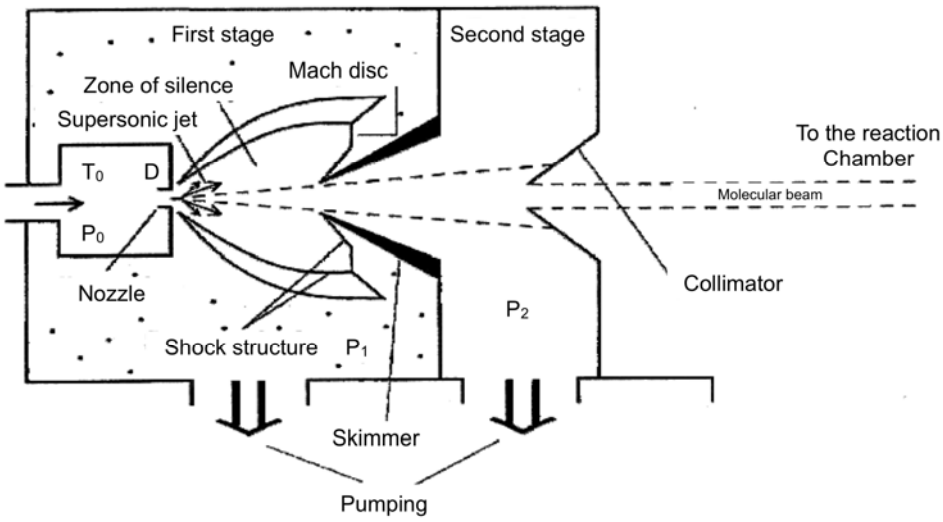

Figure II- 6 Schematic drawing of the principle of supersonic gas jet generator (Campargue type)

To make this system work properly, specific pumps for each stage are required. For the first stage, we used a combination system of three pumps: ROOTS pump of 2050m^3/h, ROOTS pump of 253m^3/h and rotary pump of 40m^3/h. The vacuum in second stage is obtained with a turbo pump of

400l/s associated with a rotary pump. The vacuum in the collision chamber is kept by a turbo pump and liquid nitrogen trap. Finally, to avoid diffusion of the jet, a beam dump is located after the collision region and is pumped with a 70l/s turbo molecular pump. Between the collision chamber and the gas generator device is inserted a valve which allows the jet to flow into the chamber or isolates it rapidly and efficiently.

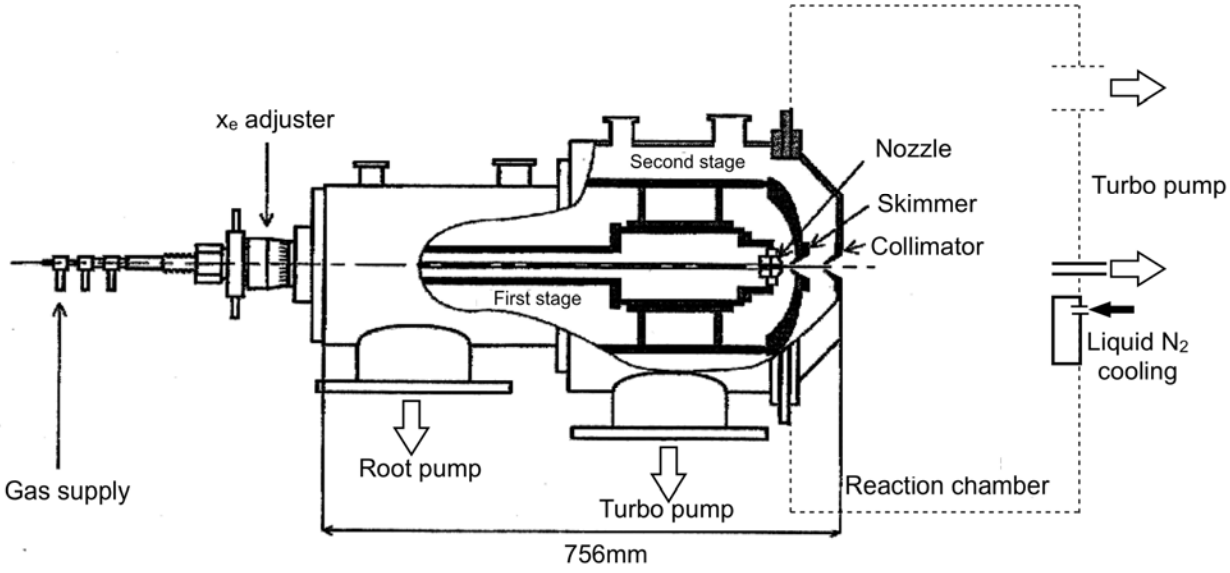

Figure II- 7 Mechanical aspects of the supersonic gas jet generator and pumping systems

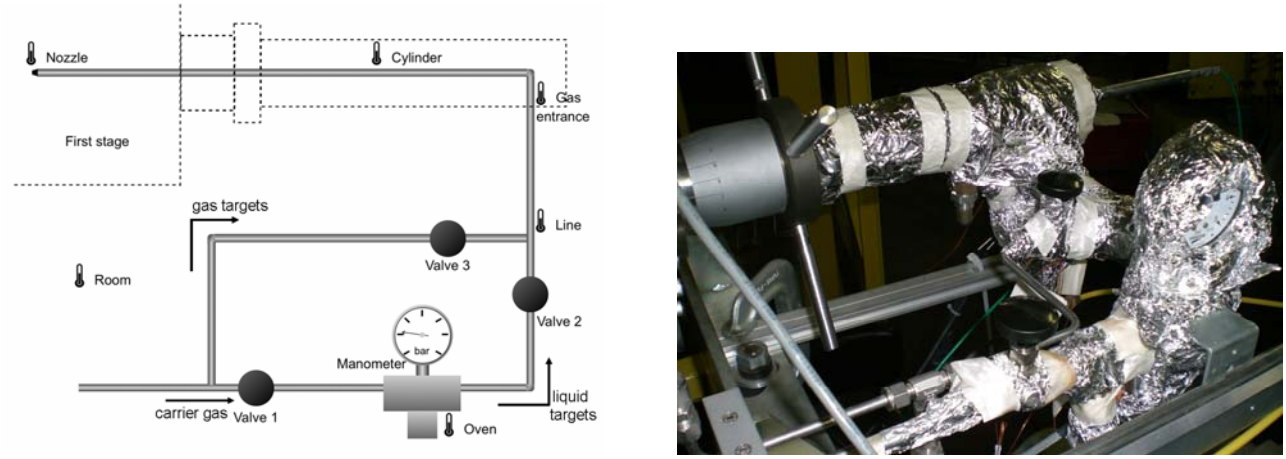

Figure II- 8 Photograph and schematic drawing of the source gas injection apparatus. Temperatures at 5 points along the gas flow and of the room are surveyed and limited to certain values. Whole apparatus is winded by heating wires and covered by Al foil.

In order to be able to use molecules from a liquid at room temperature, an oven has been added to the setup. The vapor has to be transported from the oven to the nozzle through heated stainless steel tubes. The oven has to be the coldest point in order to avoid condensation. Heating and temperature monitoring is remotely controlled by a Lavbiew program through a Field Point interface.

II.2.2 NO_2 Preparation

Handling NO_2 is rather complicated. First of all, it's a highly toxic gas. An NO_2 detector has been used for that purpose. The other problems are due to the chemical and physical properties of NO_2. Nitrogen dioxide is a liquid in normal atmospheric condition (Figure II-9a). Thus heating is necessary in order to obtain a high enough pressure for the supersonic gas jet. Furthermore, the main problem is due to the fact that NO_2 almost does not exist as a pure molecule. At low temperature, it polymerizes to the dimer N_2O_4. To form the monomer NO_2, temperature has to be raised (Figure II-9b) to change the relative proportion of each compound. It is only above the critical point at 158°C that the gas consists only of monomer NO_2. In practice however, it is pretty hard to keep all equipment at this high temperature. The nozzle was then kept at around 100°C and experiments have been performed at different injection pressures (2 and 5 bars) in order to estimate the contribution of the dimers.

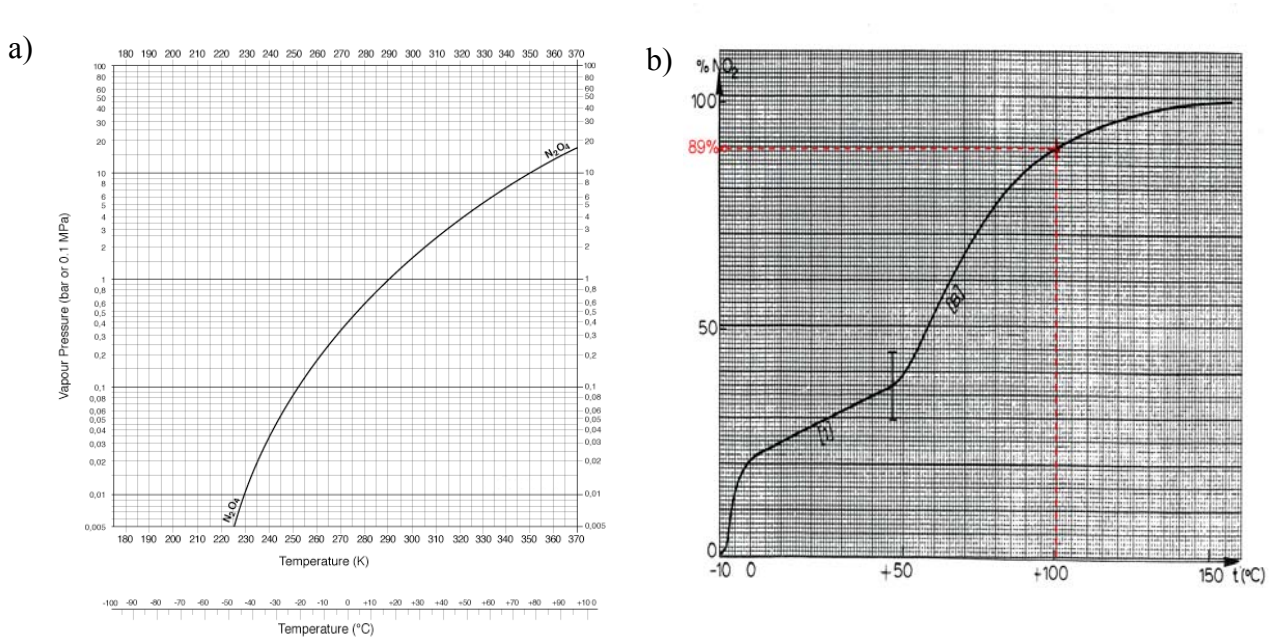

Figure II- 9 a) The relationship temperature versus pressure for N_2O_4. b) Phase diagram of $NO_2 \leftrightarrow N_2O_4$. The red line indicates the applied nozzle temperature and corresponding ratio of NO_2 expected in the present experiment.

II.2.3 HDO Preparation

HDO molecule is obtained by mixing liquid H_2O and D_2O with equal proportion. The vapor obtained by heating the oven is then composed by the three molecules HDO, H_2O and D_2O in a proportion ratio of 2:1:1 respectively. As our experiment was able to sort among them, this mixture of three molecules allows a direct comparison of the respective fragmentation results. The vapor pressure was kept at around 550mbars corresponding to 84°C.

II.2.4 Characteristics

The achieved performances of the supersonic gas target in present experiments are as follows:

Diameter

The optical diameter i.e. the divergence of jet gas flow is defined by the nozzle-skimmer-collimator geometry.

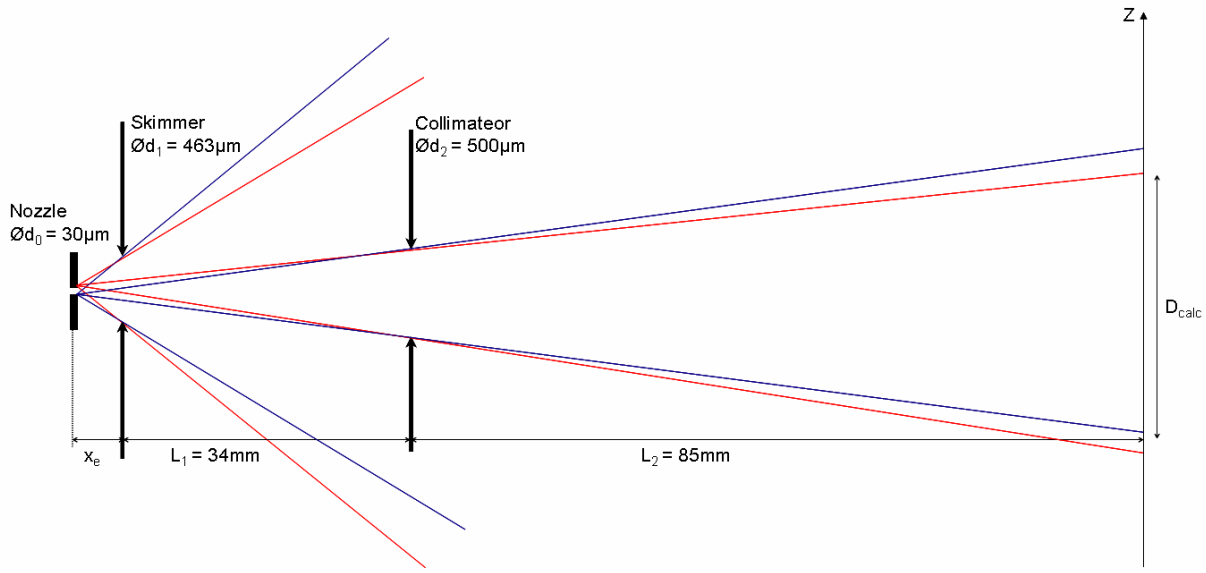

Figure II- 10 Schematic drawing of the gas jet geometry

Velocity

The velocity mean value of molecular gas jet is given by

$$V = \sqrt{5.347 \frac{RT}{M}} \qquad (2.\ 1)$$

where R is the molar gas constant, T is the temperature in Kelvin and M the molar mass of the molecule [ref. II.1].

Target (mass)	x_e [mm]	D_{calc}[mm]	D_{exp}[mm]	T [K]	V_{calc}[m/s]	V_{exp}[m/s]
NO_2 (46)	2.5	1.7	1.5±0.3	340	573	734±160
CO (28)	4	1.5	1.2±0.3	303	690	700±5
HDO (19)	2.5	1.7	1.5±0.3	389	953	950±5

Table II- 1 Diameter at the collision point and velocities of target molecular gas jet. (calculated and measured, see III-2)

II.3 Time Of Flight Spectrometer

This must be a heart of the COLTRIMS experiment. The spectrometer normally consists of two different parts: recoil ion detection and electron detection areas. It is positioned in the main chamber such as its extraction direction is perpendicular to both the direction of the projectile beam and the gas jet, as shown in Figure II-10. The Time Of Flight (TOF) and position information measured by RIMS Spectrometer are the observables which give access to the momentum vectors of the fragments and from which Kinetic Energy Release (KER) is deduced with a high resolution.

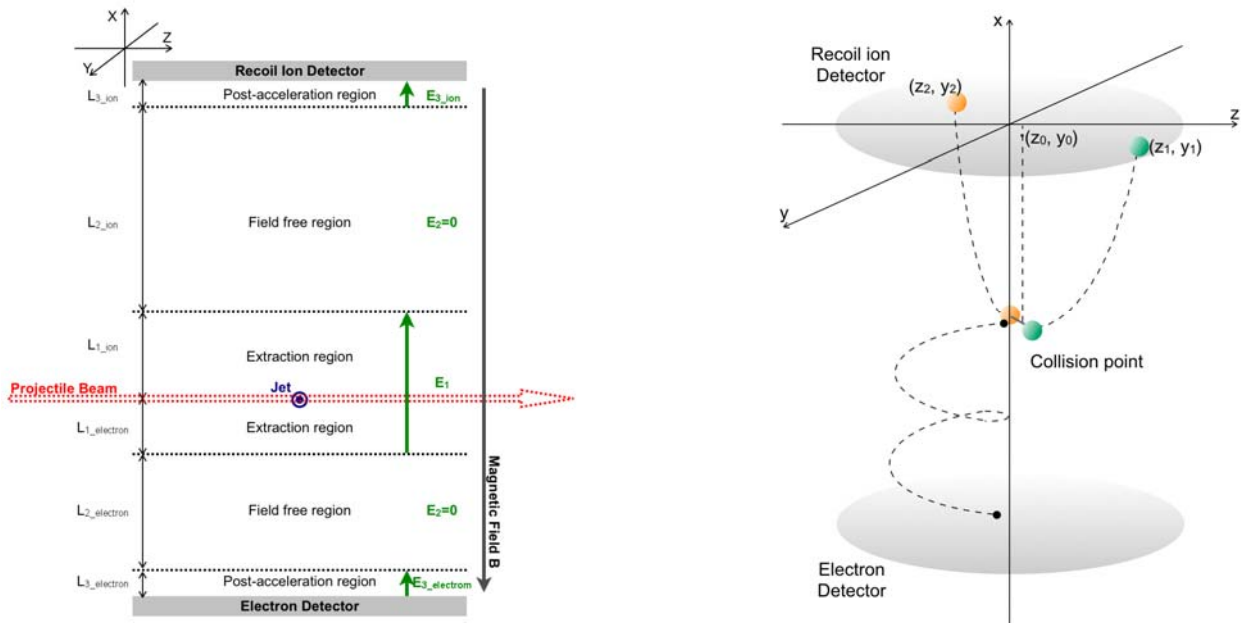

Figure II- 11 Schematic drawing of typical COLTRIM Spectrometer and geometry definition

II.3.1 Spectrometer Design and Construction

Parameters one should adjust for expected reaction channel detection are the following: 1. Extraction field E_1, 2. Extraction field length L_1, 3. Field free region path length L_2, 4. Post-acceleration field E_3 and 5. Post-acceleration path length L_3 for each side. A magnetic field can also be added for proper electron detection. Moreover the geometrical limitation has to be taken into account such as the size of chamber, the diameter of detectors. The uniform electric field is realized by a stack of electrodes. Each electrode is pilled up with 5mm ceramics spacers and connected with resistors of 2.74 MΩ. The extraction region is closed by high transmission (90%) grids on both sides.

II.3.2 Time Of Flight Equations

It is useful to calculate TOFs of fragments in each region independently. From the motion equation, the flight time of each region T_1, T_2 and T_3 are given as follows. Then the total TOF is equal to the sum of these three.

$$TOF = T_1 + T_2 + T_3 \tag{2. 2}$$

Extraction region

When a particle of mass m, charge q and a velocity vector $\boldsymbol{v}$ flights through the first region under the extraction field $\boldsymbol{E_1}$ and the magnetic field $\boldsymbol{B}$ (see section II.3.5), the motion equation is described as follows:

$$m \cdot \boldsymbol{a} = \boldsymbol{F} = q(\boldsymbol{E_1} + \boldsymbol{v} \times \boldsymbol{B}) \tag{2. 3}$$

$$\begin{cases} m \cdot a_x = qE_1 \\ m \cdot a_y = qBv_z \\ m \cdot a_z = -qBv_y \end{cases}$$

Thus the equation along to the x axis is expanded into:

$$\upsilon_{(t)} - \upsilon_{0x} = \int_0^t \frac{q}{m} E_1 \, dt = \frac{q}{m} E_1 \, t \tag{2. 4}$$

$$L_1 - x_0 = \frac{q}{2m} \; E_1 T_1^2 + \upsilon_{0x} T_1 \tag{2. 5}$$

$$T_1 = \frac{m}{qE_1} \left\{ -\upsilon_{0x} + \sqrt{\upsilon_{0x}^2 + \frac{2qE_1}{m}(L_1 - x_0)} \right\} \tag{2. 6}$$

where v_{ox} is the initial velocity the particle has after the collision and the second term of the last equation indicates the velocity at the exit of the extraction region. The aim of this extraction is to reach a 4π detection solid angle for the particles and velocities of interest.

Field-free region

Since there is no electric field, the velocity of the particle stays constant.

$$T_2 = \frac{L_2}{\sqrt{\upsilon_{0x}^2 + \frac{2qE_1}{m}(L_1 - x_0)}} \tag{2. 7}$$

Post-acceleration region

The particle is again accelerated by the electric field E_3 to have enough energy to trigger the detector.

$$T_3 = \frac{m}{qE_3}\left\{-\sqrt{\upsilon_{0x}^2 + \frac{2qE_1}{m}(L_1 - x_0)} + \sqrt{\upsilon_{0x}^2 + \frac{2qE_1}{m}(L_1 - x_0) + \frac{2qE_3}{m}L_3}\right\} \tag{2. 8}$$

These equations indicate that the TOF of the particle principally depends on its initial velocity along to the x axis, the collision point and the ratio of its mass over charge.

II.3.3 Time Focusing Condition

In order to improve the more resolution of this kind of spectrometer, the electrode geometry is set such as the Wiley-Maclaren condition is fulfilled [ref. II.8]. This time-focusing condition means that the flight time is independent from the collision point:

$$\frac{dTOF}{dx_0} = 0 \tag{2. 9}$$

According to (2.6) - (2.8), as long as $qE(L_1\text{-}x_0) >> 1/2mv_{0x}^2$, the influence of the target size is suppressed at least to first order if the following condition is fulfilled.

$$L_2 \approx 2L_1 \tag{2. 10}$$

For NO_2 fragmentation, by adopting this condition, we have observed several different ionized dissociation channels induced by ion impact simultaneously. The first region is for extraction. The electric field of this region provides the initial separation of positive (recoil ions) and negative (electron) particles. The acceleration should be high enough to gain the z direction velocity to reach detectors keeping 4π solid angle. The second region is used for a field free region which has a length twice of that of extraction path for time focusing for fragment ions. The calculated NO^+ fragment TOF as a function of x_0 is shown in figure II-12. It shows that the time of flight does not depend on the collision point location x_0 over a range of a few millimeters. In practice, there are few tenths of millimeters off due to the geometrical limitation by the size of electrodes and spacers.

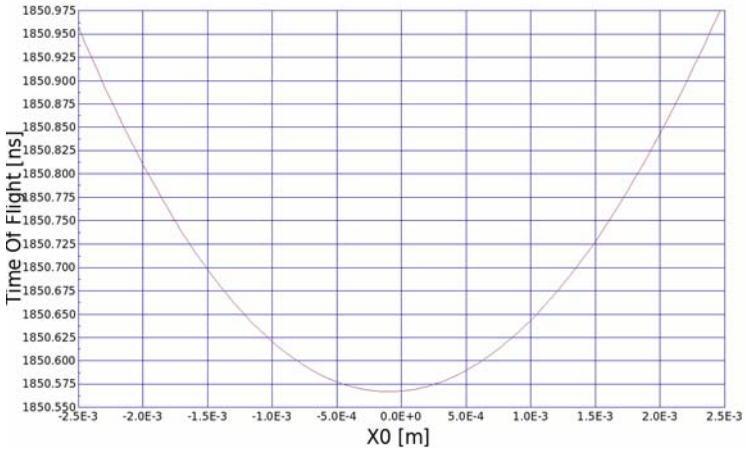

Figure II- 12 Time focusing image of NO^+ fragment in the present spectrometer.

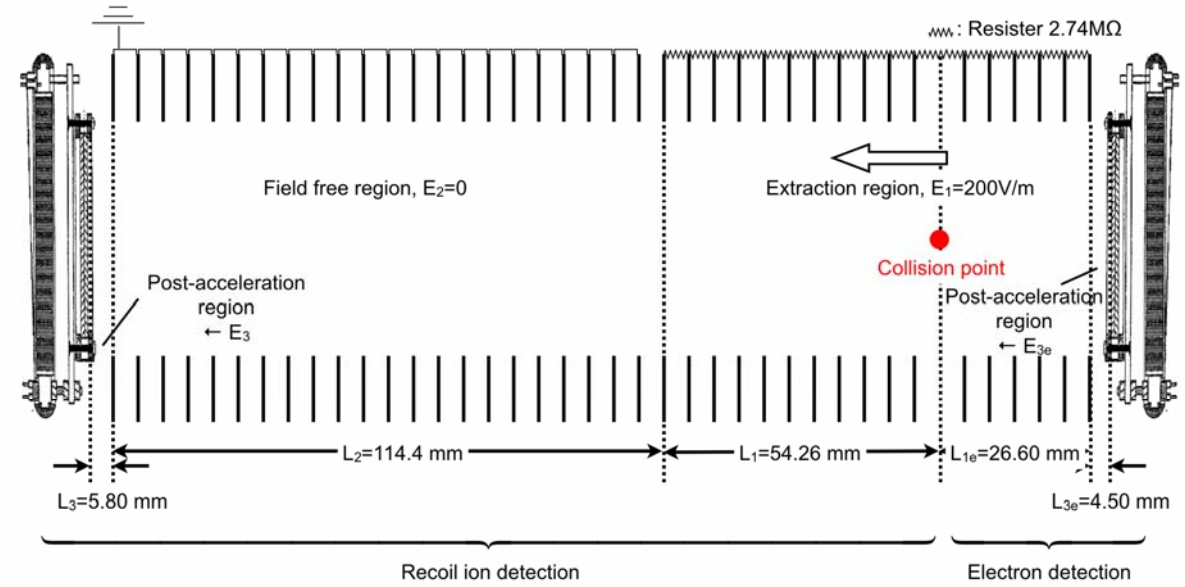

Figure II- 13 Spectrometer for NO_2: Wiley-MacLaren time focusing condition

II.3.4 3D Focusing Condition

The time focusing condition brings a strong improvement in the TOF resolution, even more in the case of single fragment detection. However, this condition has no effect on the velocity components obtained from the position measurement on the detector.

An alternative exists for complete events, for which all fragments are detected and the field free region suppressed. This allows to mount the position sensitive detector closer to the collision point. As a consequence, a weaker electric field may still provide a 4π detection solid angle. This leads directly to an improved resolution on the fragment momentum determination which, furthermore, enhances the resolving power of the apparatus. Indeed, the different fragmentation channels, such as $H^+ + OD^+$ and $D^+ + OH^+$ are much better separated. As will be showed in section III-3, this method corresponds to a space focusing in all three dimensions. To realize the spectrometer in such a short size, one has to take into account the maximum flight distance of the particle which has the initial velocity in opposite direction of its detector. The length has to be long enough to avoid particle on opposite detectors.

II.3.5 Magnetic field

To make sure that electrons are detected on a 4π solid angle, a set of Helmholtz coil is mounted around the main collision chamber. The magnetic field direction parallel to the electric field insures that electrons even with high initial transverse momentum follow spiral-like trajectories towards the detector instead of escaping. A magnetic field around 10 Gauss keeps electrons inside the spectrometer dimension. Electron detection allows acquisition triggering which makes it possible to perform the experiment with quasi-continuous beam of projectile ions.

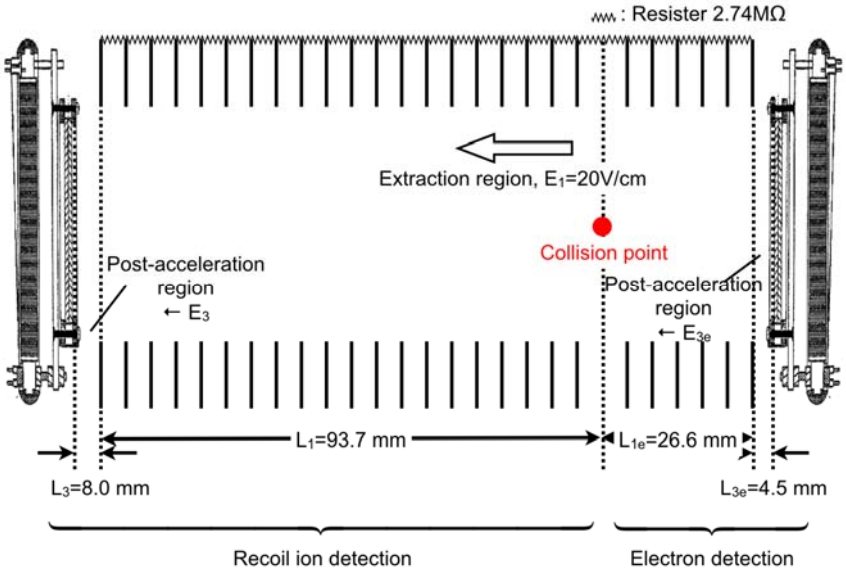

Figure II- 14 Spectrometer for NO_2: Wiley-MacLaren time focusing condition

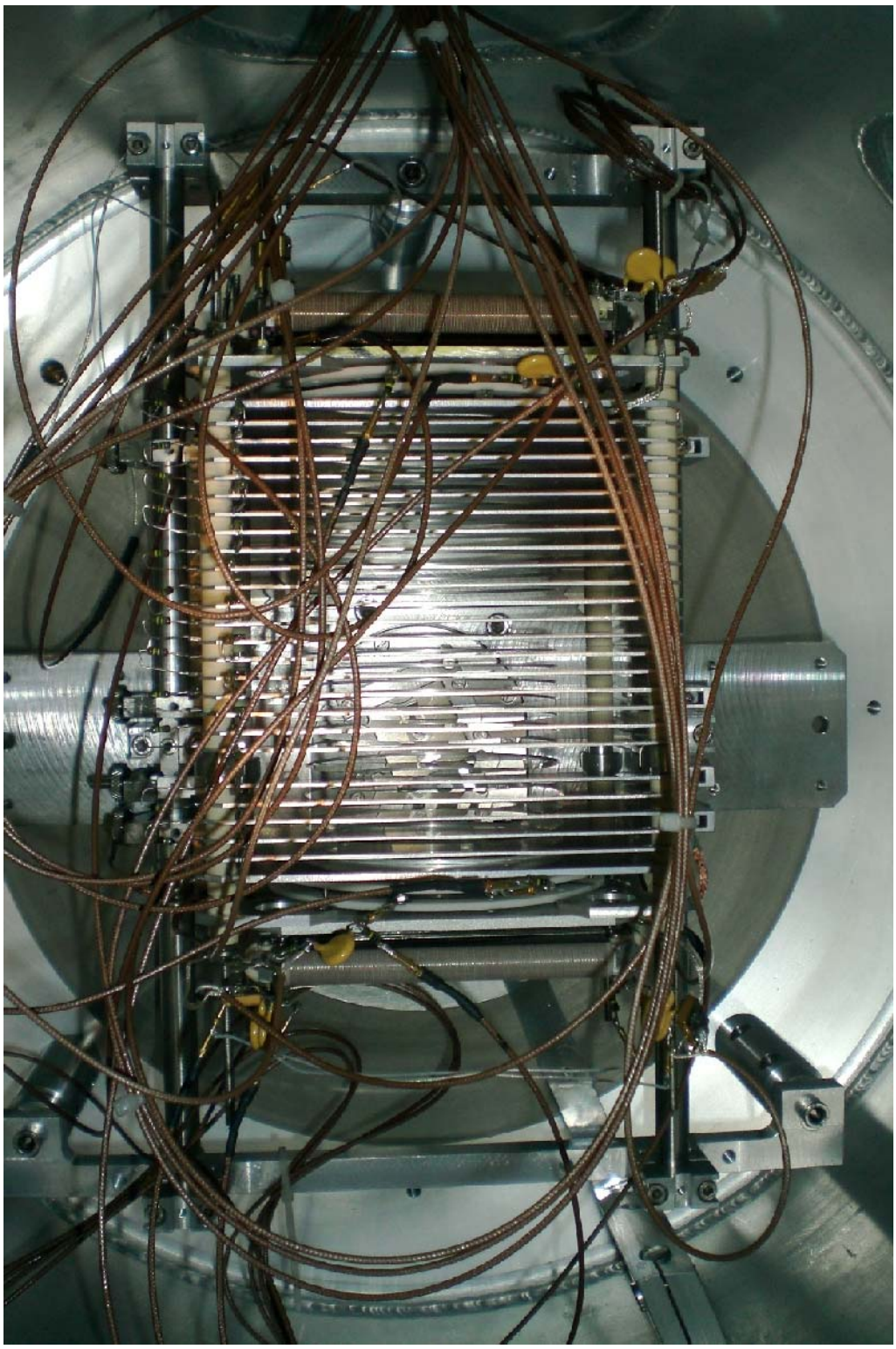

Figure II- 14 Photograph of the spectrometer for HDO experiment

II.4 Position Sensitive Detectors (PSD)

In order to obtain information on momentum sharing among fragments, we need to measure the velocity vectors. Using a stack of three Micro Channel Plate (MCP) and square type two dimension Delay Line anode Detector (DLD) [ref. II.9] (figure II-15), particle arrival times and positions on the detector have been observed. This PSD system is widely used as it is capable of detecting ions, electrons and even neutral particles if they have enough energy to produce an electron avalanche on impact with MCPs. Recent progresses in electronics made it possible to use this device in a multi-hit mode. Our setup has two of these detectors (80mm in diameter) mounted on each end of spectrometer for registering positive recoil ions and electrons. The multi-hit capability and position information are mainly used on the recoil ion side since the detection of all fragments is essential for the Kinetic Energy Release (KER) reconstruction. For the low energy HDO fragmentation experiment, an additional 40mm PSD has been used for projectile ion detection (figure II-4).

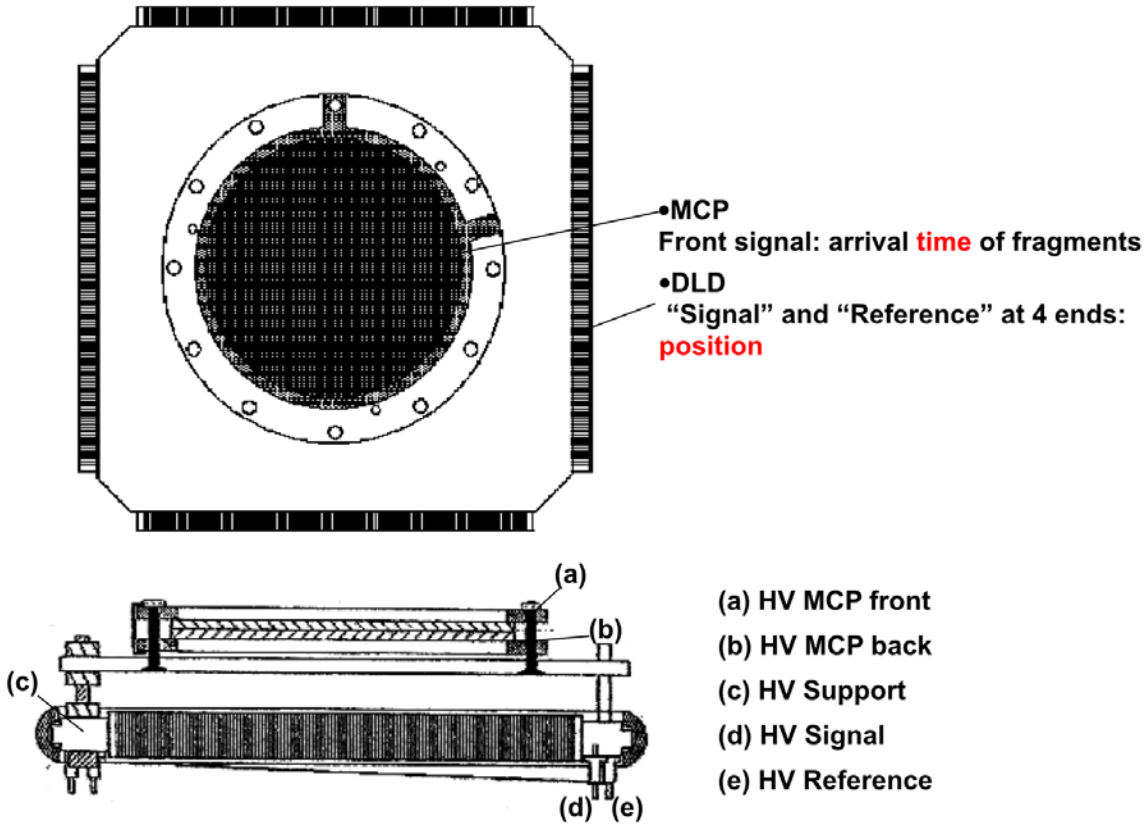

Figure II- 15 Schematic of a Position Sensitive Detector [RoentDek].

II.4.1 Micro Channel Plate (MCP)

For all our PSD devices, a so-called z-stack (three plates) type MCP is used. When an ion or an atom having an energy in the order of few keV hits one of the MCP channels, secondary electron avalanche occurs as illustrated in figure II-17. This signal from the MCP front gives the flight time of fragments and secondary electrons exited from MCP back are used for position detection on the DLD. The detection efficiency for charged particles with a kinetic energy of about 2keV or more is about 60%, determined by the ratio of the open channel surface over the total surface. For electron detection, the best efficiency is realized at kinetic energies between 100 - 3000eV. The MCPs have to be biased under a vacuum of 10^{-6} mbar or better.

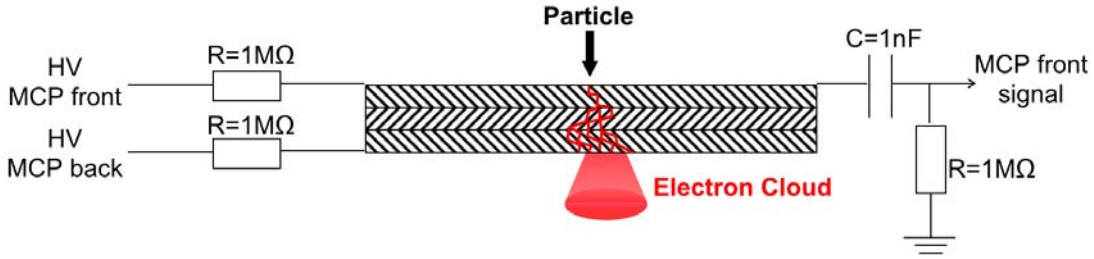

Figure II- 16 Schematic of MCP and its signal pick up electronics.

II.4.2 Delay Line Detector (DLD)

The detector anodes is made of two pairs of wires wound, perpendicular one to the other, in many loops around a biased support and with a spacing of the order of 0.5mm. This anode collects the electron cloud coming from the back side of the MCP stack. The 2D position (Z, Y) is derived from the propagation time of the electric signal toward the wire ends (T_1_Z, T_2_Z and T_1_Y, T_2_Y). In each pair of wires, one is biased in order to collect the electrons while the second one acts as a reference. The final anode signal is obtained after subtracting the reference output to the collected signal using miniaturized transformers (TP104 from Richardson Electronics s.n.c) inside the reaction chamber. The small sized differential circuit makes it possible to avoid the noise on the cable. This differential signal is then fed into fast differential amplifiers (ORTEC FTA 820A) followed by Constant Fraction Discriminator (ORTEC CFD 935). The final time coding is performed by a CAMAC Time-to-Digital Converter (LeCroy TDC3377).
The positions are then calculated by:

$$Z = C_{DLD}(T_1\_Z - T_2\_Z)\,, \quad Y = C_{DLD}(T_1\_Y - T_2\_Y) \qquad (2.\ 11)$$

where C_{DLD} is the conversion factor of the "time/position" corresponding to the propagation the velocity of signal along the wires. For our recoil ion detector, the propagation time from one end of the wire to the other is in the order of 70ns.

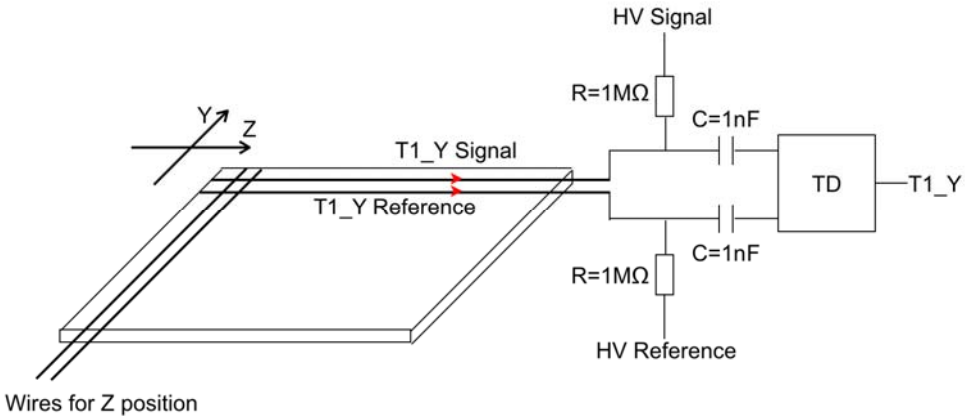

Figure II- 17 Schematic of DLD and its signal pick up electronics

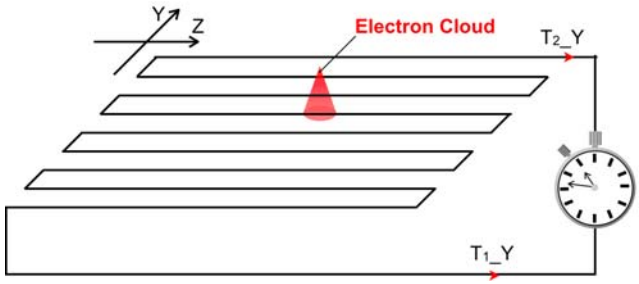

Figure II- 18 Principle of position measurement of DLD

Since the length of wires is unchanged, obviously the sum of the propagation time is constant. This sum plays a very important role for the evaluation of the detector anomalies in the operation. We will discuss this additional information in section III-1.

[V]	NO_2 / Recoil Ion	NO_2 / Electron	HDO / Recoil Ion	HDO / electron
DLD Signal	-700	2900	-560	2900
DLD Reference	-750	2850	-610	2850
DLD Support	-1000	2600	-860	2600
MCP Front	-1100	2500	-960	2500
MCP Back	-3500	100	-3360	100
Grid	-1900	-100	-360	-100

Table II- 2 Bias voltages of each part of the Spectrometer

II.5 Acquisition Setup

The multi-hit fast signals coming from PSDs require sophisticated electronics. Both MCPs and DLD timing signals of each fragment have to be treated properly for high resolution measurement and a restrictive trigger is needed to avoid collecting too much uncorrelated data.

II.5.1 Signal Treatment

In present experiments, measuring the time precisely is of importance since both TOF and position rely on it. Thus, we have used Constant Fraction Discriminator (CFD) for all signals from PSD sets. CFD generates a logical signal when the input signal reaches a certain "fraction" of its amplitude. This function allows us to obtain timing information independently from the pulse height of signals. The operation principle of a CFD is as follows: 1. The input signal is duplicated. 2. One is reversed and attenuated, the other is delayed. 3. The sum signal (dipolar shape) crosses 0V and starts the logical signal at the same moment independently form its amplitude. In practice, however, there is a so-called "jitter" on the zero-crossing resulting from the signal to noise ratio achieved. For our detector, the remaining jitter is lower than 1ns.

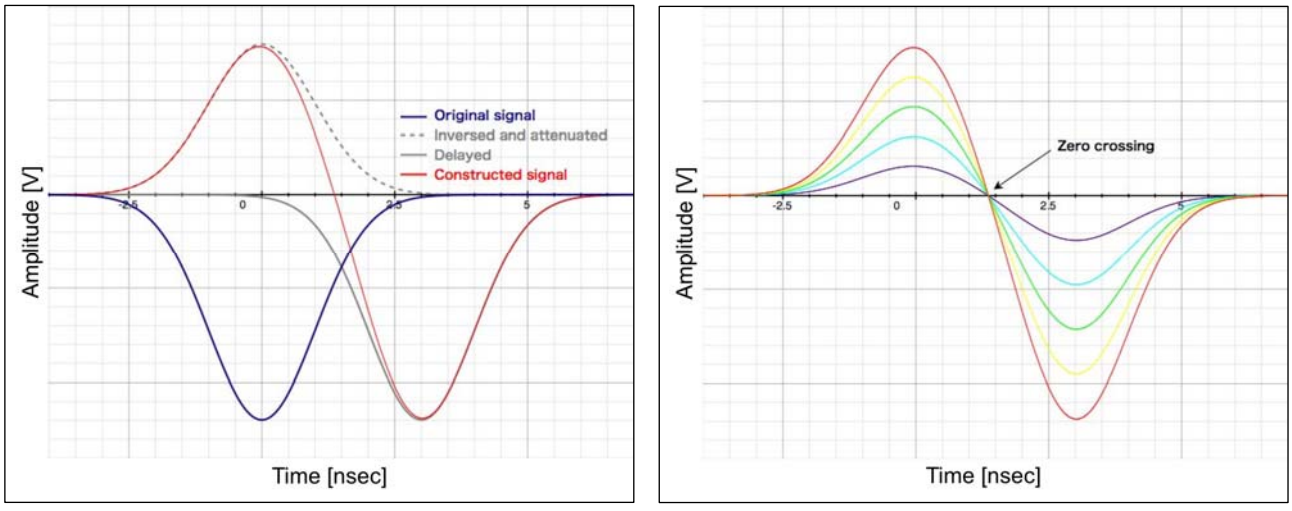

Figure II- 19 Principle of the CFD operation

Then output signals from CFDs, i.e. the arrival times are measured by a LeCroy 3377 TDC (Time-to-Digital Converter) or utilized to make a reference time ("trigger", see below). This type of TDC has incorporated 32 independent signal channels which are capable of recording up to 16 hits each with respect to the same reference time. This reference time is used as a "COMMON STOP".

Thus timing signals are registered as multi-start signals. It is also important to note that to obtain the "real-TOF" from registered raw data, we need "Time Offset" corresponding time-zero which is obtained through a calibration procedure (see III-2). The processing time window was fixed between 6-10μs for present experiments. The Lowest Significant Bit (LSB) is of 500 ps for time range up to 32μs with only 8.5ns dead time [ref. I.2]. The linearity of this TDC has been once calibrated as well as the channel-time conversion factor using a Time Calibrator. The latter factor corresponds to 0.5ns within a 0.004% error.

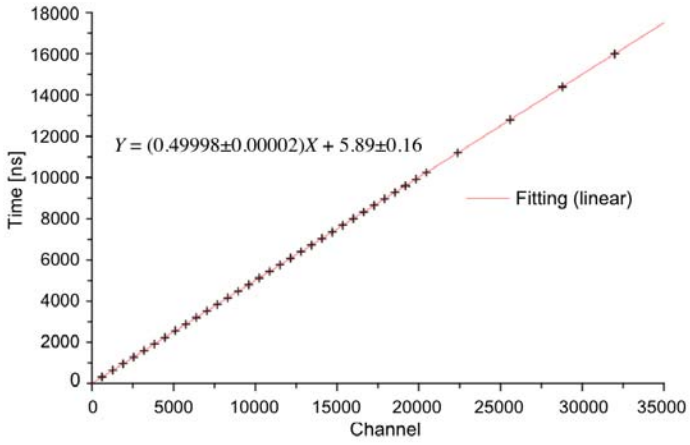

Figure II- 20 TDC calibration

II.5.2 Triggers

The role of the trigger is to sort the interesting event among all the particles reaching the different detectors. The ratio of the proper event / all detected event in the spectrometer is about 10%. An interesting event is characterized by the simultaneous accurence of an ionizing event and a molecular fragment ion detecting several signals are conbined in order to make the decision of keeping or rejecting the event:

-cyclotron high frequency (HF)
-projectile bunch detection
-electron detection
-recoil ion detection

The fast-decision electronics is showing figure II-21. The first coincidence is made between the HF signal and the projectile detection signal in order to get rid of the noise (AND1 on figure II-21 and 22). An ionization rection is then identified as an additional coincidence with the detection of an electron (AND2). This decision has to be made before the next projectile ion bunch collides on the gas target (≈100ns). The final coding order sent to the acquisition results from the last combination with the recoil ion signal (AND3). This signal has to arrive before a certain delay relative to the projectile detection. This delay corresponds to the time of flight range of the experiment.

The AND2 output starts the GATE1 to open a time window of 10μs long to make the triple coincidence signal with the recoil ion. Finally after the construction of the reference time signal by combing the impulsion of the GATE2 and the delayed HF signal, this signal is plugged into the TDC Common Stop input as the master trigger of the experiment. Both the AND1 and the AND2 signals are measured by TDC for additional information on count rates. During the operation, without precise analysis, the AND2 is also used as the virtual time origin to obtain rough TOF spectra (see section III-2).

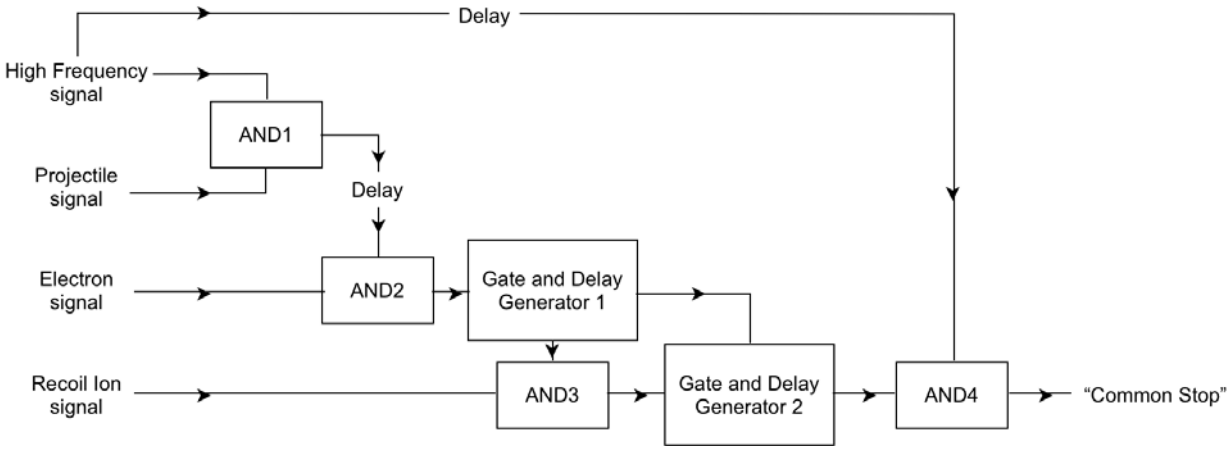

Figure II- 21 Flow chart of trigger signal generation

II.5.3 Acquisition control programs

The GANIL acquisition system, through a VME front end is used to control CAMAC modules and register the obtained data in list mode. Users can modify their control programs in FORTRAN language and configure the CAMAC modules through an active user interface. The major advantage of using this system is its capability to build the analysis program into the user control program file and to visualize transformed values during the acquisition as well as primary spectra. The user control files are sorted mainly in three parts: the module definition part, the parameter definition part and the master control programs. The spectrum visualization is realized using the VISUGAN (VISUalisation GANIL) system in default and users can easily adopt the GRU (GANIL ROOT Utility) system based on the ROOT software [ref. II.10] which has much more applications for analysis. Connecting through the internet network to GANIL acquisition server, we use freely the libraries of programs and can record data onto server, local Linux machine and extension disk at the same time if needed.

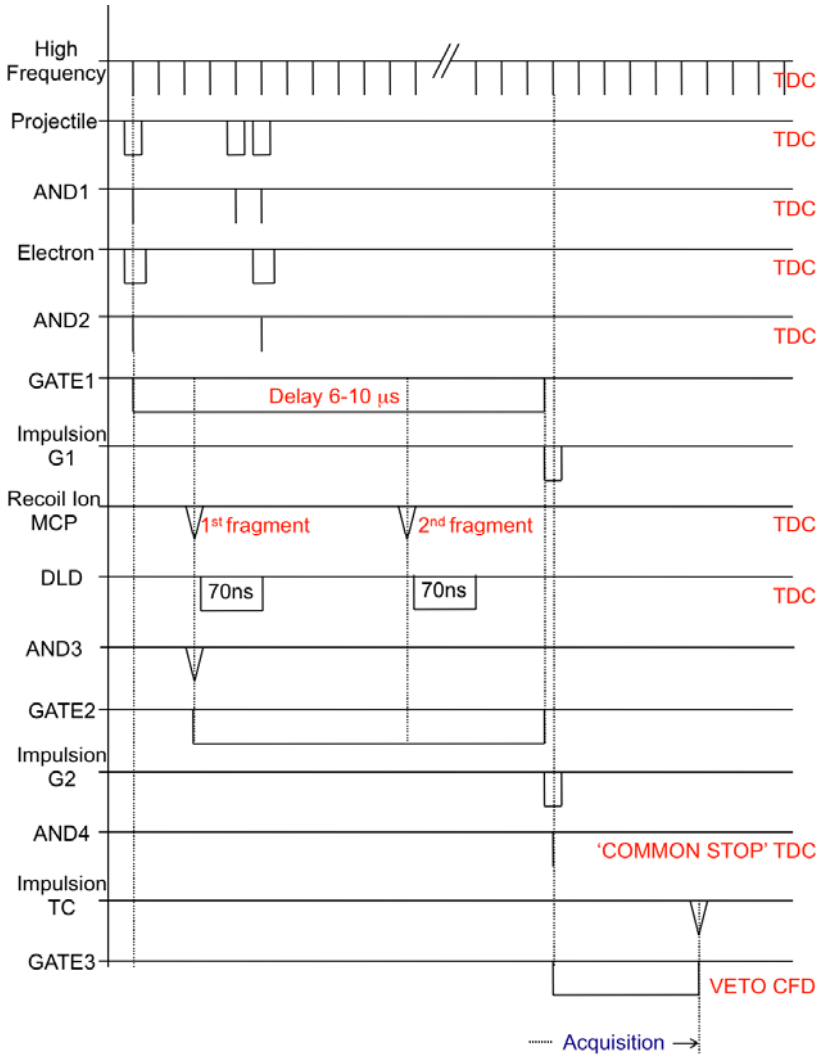

Figure II- 22 Timing algorithm for generating the trigger

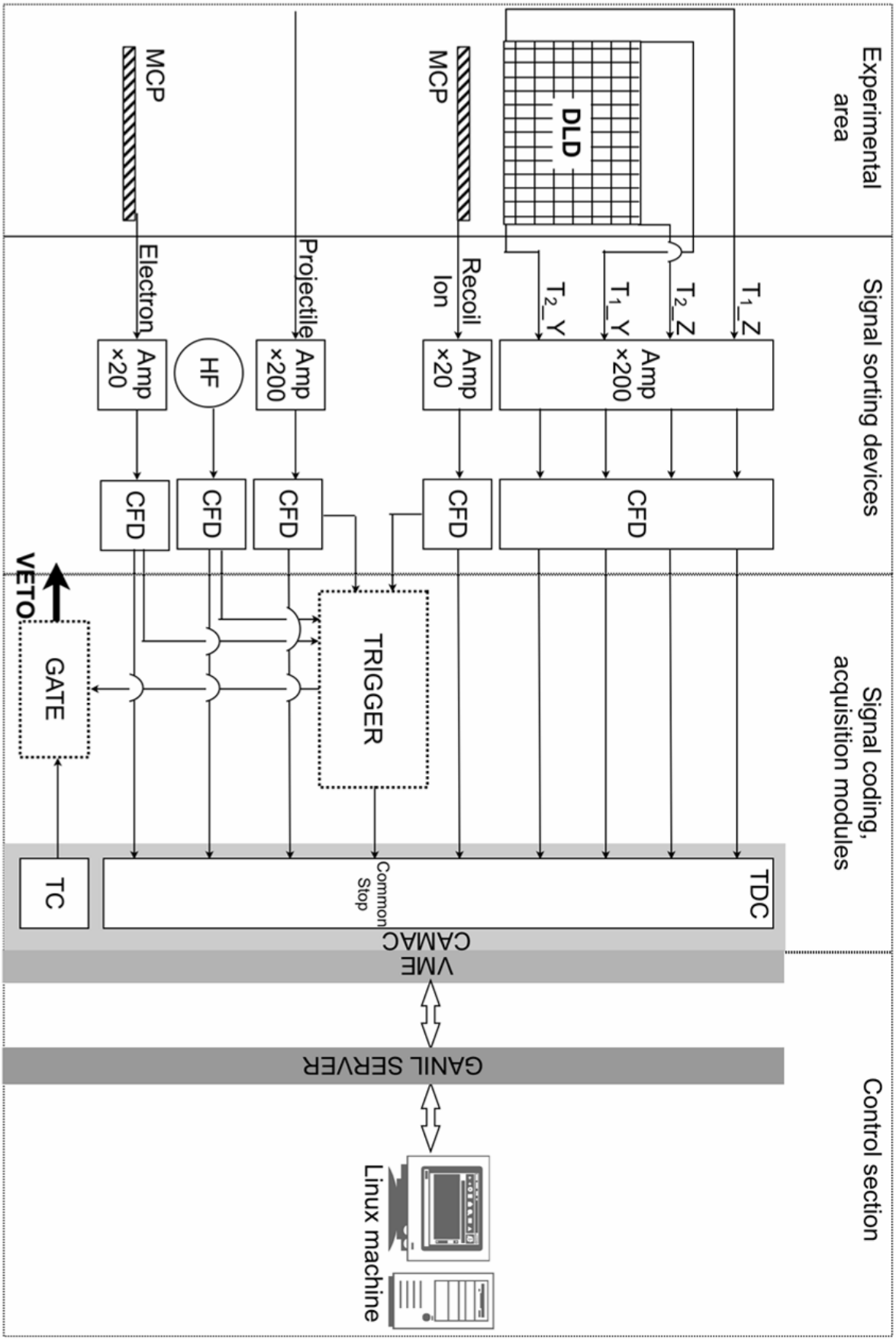

Figure II- 23 Overall view of experimental setup.

§ III Data Analysis Details

In this chapter, the detailed data reduction process to obtain proper results is presented. First the preparation of the data set for analysis is described. Then observed projectile, target molecule jet and fragments characteristics are presented in detail for each experiment: NO_2, HDO at SME and HDO at ARIBE. One of the advantages of the COLTRIMS data analysis is that most of the constants and factors defined by the experimental setup can be extracted from the obtained data itself.

III.1 Preparation of Data

III.1.1 Algorithm

As we are using the GANIL acquisition system, raw data were recorded in the GANIL original format. For the analytical treatment in ROOT software, first of all, the format is modified using the program "GANIL to ROOT" for multi-hit experiments[1]. After the transformation, from the raw data in ROOT format, so-called “Good Events” are selected (First Step). “Good” means that more than two ions are detected and all 5 recoil ion detector signals (TG_DI[2], T1_Z, ..., T2_Y) have the same number of hit. In the same program, two functions and one calculation are included as well: 1. the random numbers are added to all obtained values in order to avoid any discrete structure, 2. multi-hit timing values are rearranged in right order since we used the TDC in “Common Stop” mode, 3. propagation times on the DLD detector are calculated. Then the events are filtered by the propagation time sum of both z and y direction to select proper events (Second Step). Finally

[1] The multi-hit program was realized thanks to Luc Legeard from GIP (Groupe d'Informatique pour la Physique) of GANIL.

[2] The timing signal from MCP front of recoil ion detector in French: Temps Gallette_Detecteur Ion.

all run files with filtered events are chained (Third Step) after verifying the agreement of calibration parameters of different run files. Then the final data file is prepared. Additional calculation and visualization are done in the Third Step program files for each dissociation channels separately.

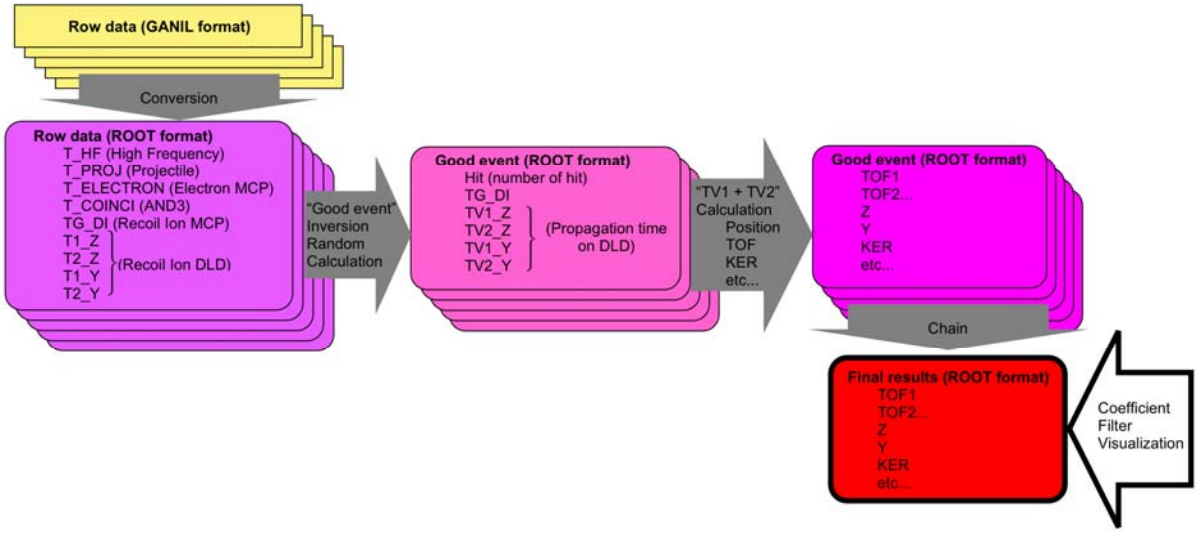

Figure III- 1 Procedure for data reduction

III.1.2 Propagation Time of the Delay Line Anode

As it was introduced in section II-2, the sum of the signals from both sides of one delay line should be constant. This propagation time plays the role of a precise test for the detector operation and to take uncorrelated signals away. The propagation times of DLD anode (TV_1_Z, TV_2_Z, TV_1_Y, TV_2_Y[3]) are obtained by the difference between the timing signal from DLD (T_1_Z, T_2_Z, T_1_Y, T_2_Y) and from MCP (TG_DI):

$$\begin{aligned} TV_1\_Z &= T_1\_Z - TG\_DI \\ TV_2\_Z &= T_2\_Z - TG\_DI \\ TV_1\_Y &= T_1\_Y - TG\_DI \\ TV_2\_Y &= T_2\_Y - TG\_DI \end{aligned} \qquad (3.\ 1)$$

since at such short distance, the flight time between the MCP and DLD is negligibly small and TG-DI may be assimilated to the arrival time of the electron cloud on the delay line.

This constant value can be represented in two different ways: the direct one dimension spectrum of the sum, or 2D spectrum of the propagation time towards one side versus the other which should be a diagonal line. Figure III-2 shows a typical sum spectrum of Z side propagation time of.

[3] TV means the “real time” in French (Temps Vrais)

The Full Width of Half Maximum is about 3 channels i.e. 1.5ns, corresponding to the regulation limit of this DLD. The background counts represent less than 0.1% of the total. The propagation time towards one side as a function of the other gives the expected negative slope diagonal line (figure III-2b) which confirms a correct setting of the detector. If there is any electrical noise or miss function, this diagonal shape collapses.

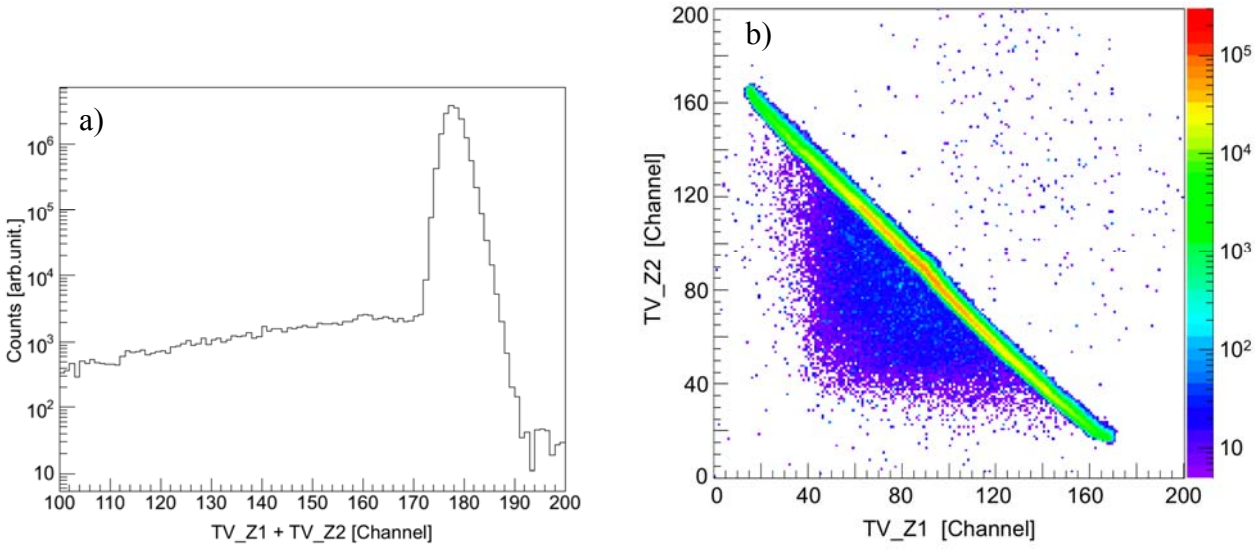

Figure III- 2 a) "TV_Z1 + TV_Z2" and b) "TV_Z1 vs TV_Z2" spectrum in the case of NO_2 experiment.

III.1.3 Position on the Detector

The direct and proper way to calibrate the DLD detector is to measure the diameter of the detector, which we know well in millimeter, in number of channels. As was described in the paragraph II.4.2, the position coordinates (Z, Y) of the recoil ion on the DLD detector is calculated from the propagation time differences at both ends of the wires. In practice, we measured the propagation times as the difference between arrival times on the MCP and on the end of wires TVi:

$$Z = C_{DLD}(TV_1\_Z - TV_2\_Z) \qquad (3.\ 2)$$
$$Y = C_{DLD}(TV_1\_Y - TV_2\_Y)$$

As shown in figure III-4, both projections on Z and Y directions of the detector image is 306 channels in diameter, while the effective detector diameter limited by MCP is 81.25mm. Thus the obtained conversion coefficient from channels to length units is:

$$C_{DLD} = \frac{81.25 \pm 0.2}{306 \pm 2} = 0.266 \pm 0.01 \text{ mm/Channel} \qquad (3.\ 3)$$

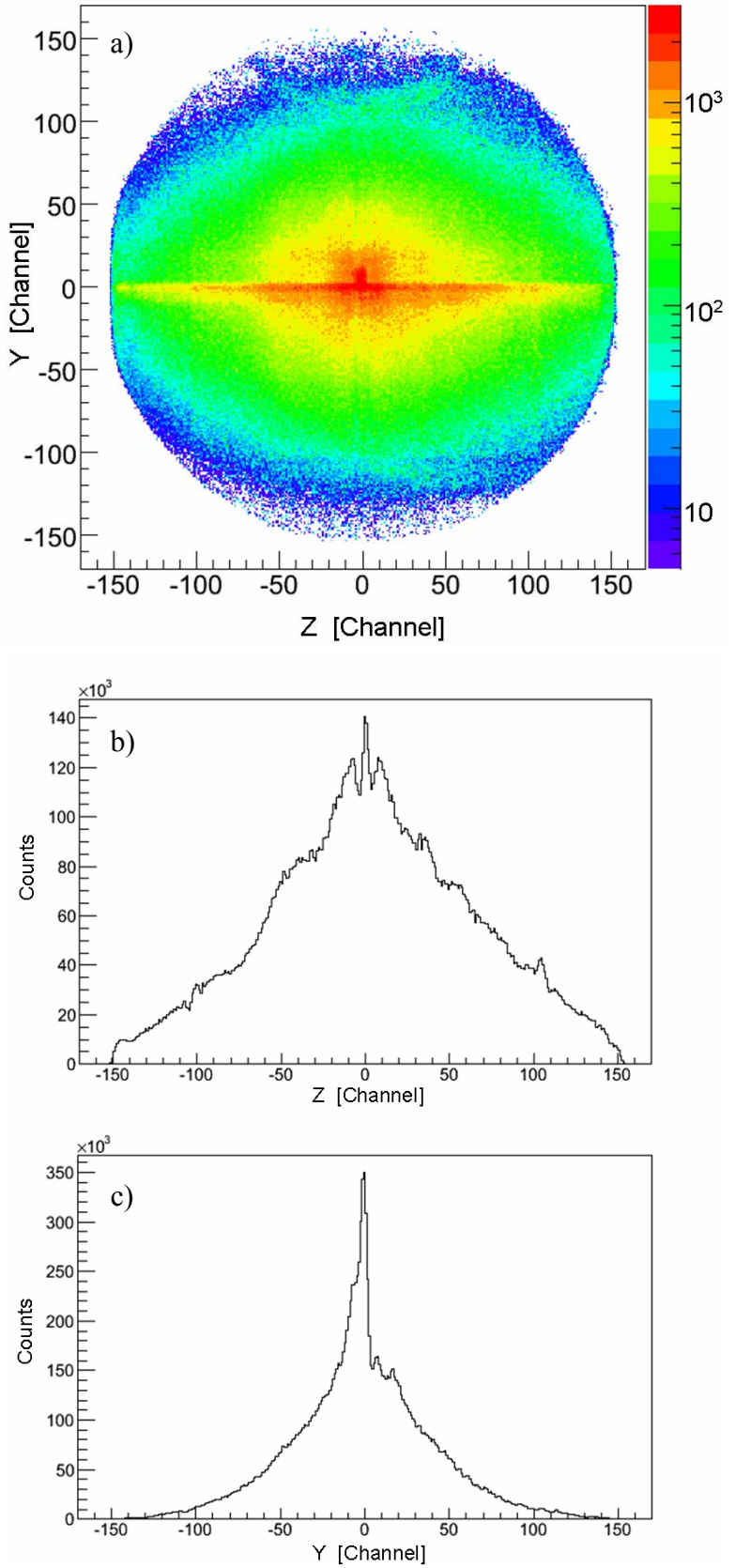

Figure III- 3 Detector image and its projections on Z and Y axis

III.2 Calibration of the NO_2 Spectrometer

The spectrometer geometry is always precisely measured during its construction before starting the experiment. The precise calibration of spectrometer is the key factor to obtain fragment velocity vectors.

III.2.1 Time Of Flight

To obtain absolute TOFs, as was mentioned in section II-4, the time origin (time-zero) has to be calibrated. Regarding the fact that the TOF depends on the square root of the fragment mass over its charge, the time-zero, called Toffset, is defined as the flight time for m=0. The time of flight for zero initial velocity (TOF_0) is calculated from equations (2.1)-(2.4):

$$TOF_{v0x=0} = \sqrt{\frac{m}{q}}\left\{\frac{1}{E_1}\sqrt{2E_1(L_1 - x_0)} + \frac{L_2}{\sqrt{2E_1(L_1 - x_0)}} + \frac{1}{E_3}\left(-\sqrt{2E_1(L_1 - x_0)} + \sqrt{2E_1(L_1 - x_0) + 2E_3L_3}\right)\right\} \quad (3.4)$$

where x_0 is the initial position of the fragment. This TOF equation is split into two parts: a term determined by the particle (mass and charge), and the other one depending only on the spectrometer characteristics:

$$TOF_0 = \sqrt{\frac{m_i}{q_i}}\alpha \quad (3.5)$$

$$\alpha = \frac{1}{E_1}\sqrt{2E_1(L_1 - x_0)} + \frac{L_2}{\sqrt{2E_1(L_1 - x_0)}} + \frac{1}{E_3}\left(-\sqrt{2E_1(L_1 - x_0)} + \sqrt{2E_1(L_1 - x_0) + 2E_3L_3}\right) \quad (3.6)$$

This simplicity makes it possible to determine the absolute time of flight of particles and the extraction filed strength.

We choose several peaks from the channel plate signal (TG_DI) spectrum and plot their channel number as a function of the square root of the corresponding mass over charge ratio. Of course, this calibration leads to a better precision if thin peaks are chosen since they lead to an easier and better determination of their position. These thin peaks are associated either to non-broken molecules or to fragments with nearly no initial velocity (smooth dissociation). Advantages can be

taken from the rest gas components as well. However, in the present experiment, NO_2^+ contribution consists not only of the charged parent molecule but also of the fragment from the charged N_2O_4 which is impossible to suppress completely from the target gas. Low recoil energy fragments are identified on the 2D spectrum on which is plotted the TOF as a function of the y component on the position sensitive detector (figure III-4). They correspond to the thin vertical lines which are associated to nearly no initial velocity along x axis (extraction axis). Since the supersonic gas jet propagates along the y direction, the displacement due to the jet velocity allows a filtering strongly reducing the background contribution. The filtered TG_DI spectra and selected ions peaks with a gaussian fitting are shown in figure III-5a,b. The calibration equation using those ions is then (III-6):

$$\text{TOF [sec]} = 989.95\sqrt{m/q}\ \cdot C_{TDC} \qquad (3.\ 7)$$

Toffset = 11891

C_{TDC} = 0.499998

In terms of resolution, the peak width of the NO_2^+ is 4channels while the mean value corresponds to 5170 in channels. The ultimate TOF resolution of this experiment is then 4/5170 ≈ 0.08%. From the above equation (3.3), the deviation of time is thus obtained as:

$$\frac{dTOF}{dm} = \frac{1}{2m}TOF \qquad \text{thus} \qquad \frac{dTOF}{TOF} = \frac{dm}{2m} \qquad (3.\ 8)$$

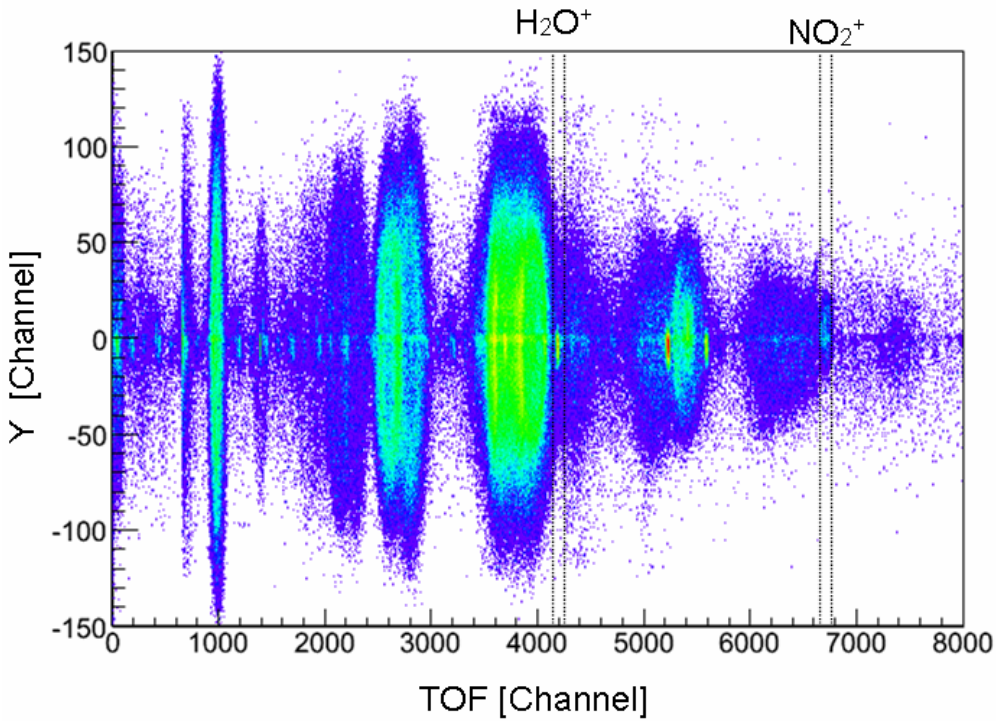

Figure III- 4 The fragment in the area -30<Y<20 was chosen to determine the absolute time zero. Detector images of H_2O^+ and NO_2^+ filtered by TOF are shown in figure III-7.

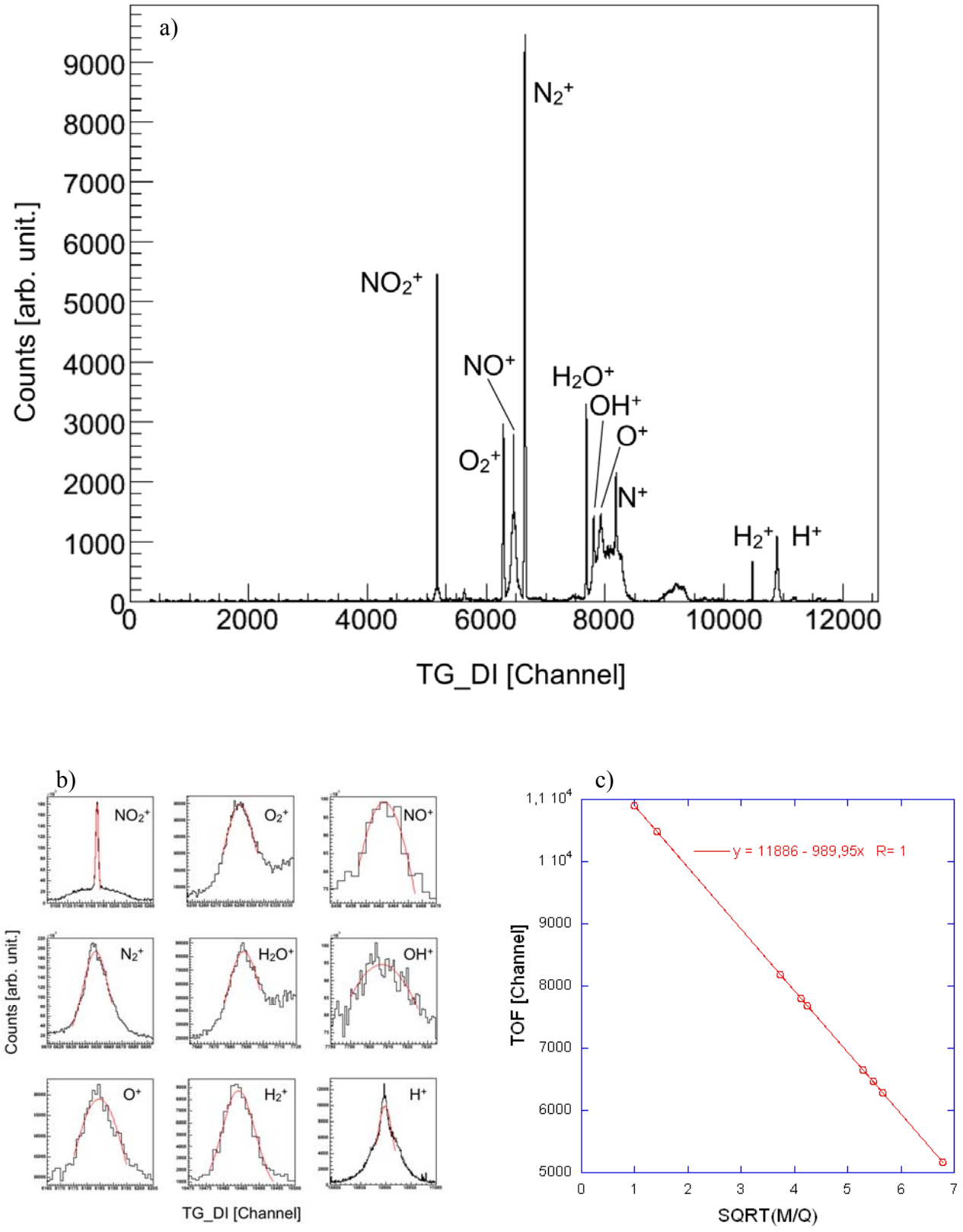

Figure III- 5 a) TG_DI spectrum of NO_2 experiment, b) selected peaks of recoil ions with a Gaussian fitting (red line), c) calibration equation using elected peaks

III.2.2 Electric Field

The extraction electric field determination is essential for high resolution measurement. To calculate the momenta of all detected ions, the extraction field strength comes directly in the equation. Though, all parameters that determine the electric field such as the spectrometer size, applied voltage, resistors in the spectrometer circuit were measured carefully, the calculated field strength is still 100V/m (≈0.5%) off. A more precise calibration done by using TOFs of recoil ions is described in the following sections.

III.2.2-a Influence of the Post-Acceleration

As it is relatively shorter distance with a higher electric field strength, the flight time in the post-acceleration zone is much smaller than across the above two regions. Let's first determine the influence of post-acceleration region on the TOF.

From the equation (3. 4), the dependence is calculated both on the extraction field E_1 and the post-acceleration field E_3:

$$\frac{dTOF}{dE_1} = \sqrt{\frac{m_i}{q_i}}\left\{\frac{1}{E_1^{\,2}}\sqrt{2E_1(L_1-x_0)} + \frac{1}{E_1}\frac{L_1-x_0}{\sqrt{2E_1(L_1-x_0)}} + \frac{(L_1-x_0)L_2}{(2E_1(L_1-x_0))^{3/2}} + \frac{1}{E_3}\left(\frac{L_1-x_0}{\sqrt{2E_1(L_1-x_0)}} - \frac{L_1-x_0}{\sqrt{2E_1(L_1-x_0)+2E_3L_3}}\right)\right\} \tag{3. 9}$$

$$\frac{dTOF}{dE_3} = \sqrt{\frac{m_i}{q_i}}\left\{-\frac{1}{E_3^{\,2}}\left(-\sqrt{2E_1(L_1-x_0)} + \sqrt{2E_1(L_1-x_0)+2E_3L_3}\right) + \frac{1}{E_3}\left(\frac{L_3}{\sqrt{2E_1(L_1-x_0)+2E_3L_3}}\right)\right\} \tag{3. 10}$$

By substituting the measured values shown in table III-1, the ratio is calculated as follows:

$$\frac{\frac{dTOF}{dE_3}}{\frac{dTOF}{dE_1}} \approx 5.0\cdot 10^{-4} \tag{3. 11}$$

The electric field of both extraction and post-acceleration region are calculated through the measured distances and the measured voltages from the High Voltage Supplier (C.A.E.N.) display. Since the TOF depends much less on E_3 than on E_1, this calculated value of E_3 is regarded as precise enough for the TOF calibration to obtain E_1 with a high precision.

L_1-x_0 [mm]	L_2 [mm]	L_3 [mm]	E_1 [V/m]	E_3 [V/m]
54.5	115.5	5.8	20300	275900

Table III- 1 Measured parameters of spectrometer for NO_2 Experiment

III.2.2-b Extraction Strength Determination for NO_2 Experiment

For a spectrometer with a field free region as we used for NO_2 experiment, extracting the E_1 from the TOF equation is not an ideal way to determine its value because of the complicity. What was done here is a least-square method. The electric field of the extraction region is given by the value minimizing the variation between the calculated TOF described as equation (2.10) and the measured one. In practice, using the values of the NO_2^+ and the H_2O^+, we kept the E_1 value which minimizes the sum of χ defined as follows:

$$\chi(E_1) = \sum \left(TOF_i^{mesured} - TOF_i^{calculated}(E_1) \right)^2 \qquad (3.\ 12)$$

The extraction strength E_1 finally deduced is 20350 ± 50[V/m].

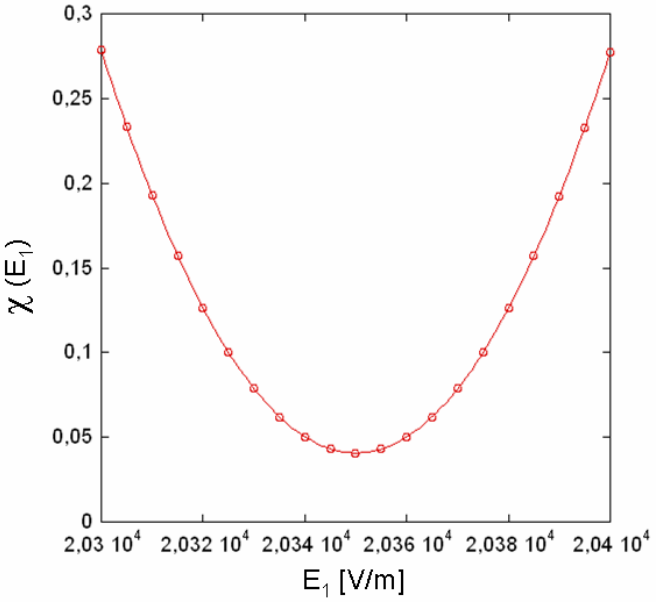

Figure III- 6 χ as a function of extraction field strength E_1

III.2.3 Collision Point

To obtain the fragment velocity vector components in the detector plane, i.e. along the projectile beam and the target supersonic gas jet, the collision point information is required. For the NO_2 experiment, the size and the position of the collision region for all events are estimated by the projection of detected ions on the position sensitive detector, in contrast to the position focusing experiment which can determine exactly where the parent molecule was when the collision occurs and for each individual event (see section III.3.2).

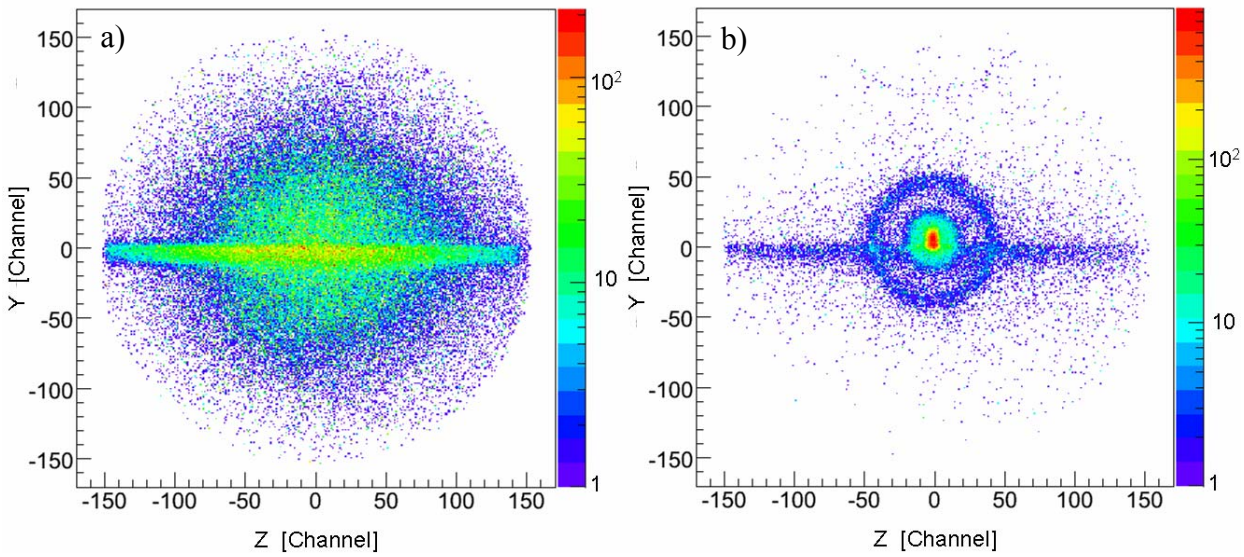

Figure III- 7 a) Detector image of H_2O^+, b) NO_2^+

The collision region width along Y axis corresponding to the projectile profile is estimated by the position distribution of the ions from target gas jet which is initially cold. However, since the target supersonic gas jet has a certain initial velocity along the Y axis, the mean position of the distribution of the ions from the target gas jet is shifted from the collision point center Y_0. The trace of the beam obtained through the ions from the residual gas in the reaction chamber has this Y_0 information, but not the width due to its initial thermal velocity. The residual gas encountered the projectile, mainly contains N_2, O_2 and H_2O. Thus as shown in figure III-8, we can observe those ions as the trace of the projectile beam on the recoil ion detector. The thermal velocity of the residual gas follows the Maxwell-Boltzmann distribution which provides the non-negligible velocity mean value, for example about 500m/s for H_2O at room temperature. In practice H_2O^+ is the only ion from the residual gas with enough statistics (N_2^+ and O_2^+ ions are mixed with the fragments from the target molecule NO_2 and N_2O_4). The non-dissociated ion from the supersonic gas jet, NO_2^+ in this case, is used to estimate the collision region width along to the Y axis. Although the NO_2^+, as a fragment produced by coulomb expansion of $N_2O_4^{2+}$ exists, we can clearly separate the NO_2 contribution from the N_2O_4 contribution due to its momentum difference (figureIII-7-b: ZY image of NO_2^+). However, as shown in the figure III-8, the distribution width of detected H_2O^+ and NO_2^+ along the Y axis is almost the same. This indicates that the size of the projectile beam was larger

than the thermal motion in this experiment. In fact that the projectile size was about 1.5 times larger than that of the previous experiment [ref. II.3]. On the other hand, for the target gas jet profile, both the position and its width are estimated by the Z axis projection of the NO_2^+ image on the detection. These values are shown in Table III.2.

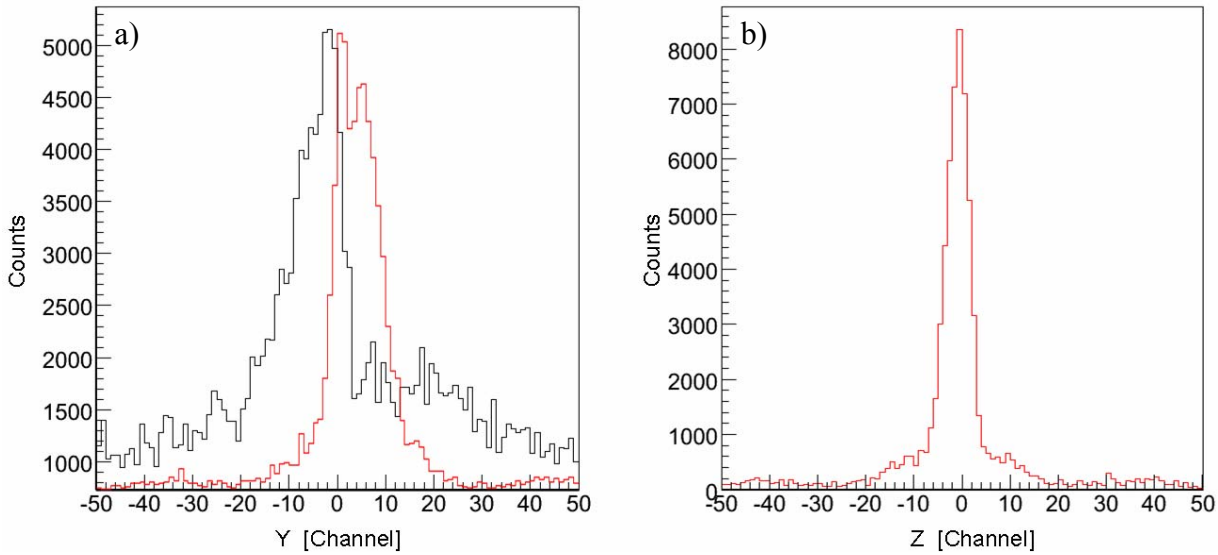

Figure III- 8 a) Projection along the Y axis of H_2O (black) and NO_2 (red), b) Projection along the Z axis of NO_2

Y0 [mm]	Y FWHM [mm]	Z0 [mm]	Z FWHM [mm]
-1.3	2.4	-0.3	1.5

Table III- 2 Size of collision region of NO_2 experiment (see table II-1 for expected theoretical calculation).

III.2.4 Velocity Components Determination

The absolute time of flight, the extraction field strength, and the different collision point location used to determine the velocity components of fragments. Considering the equation giving the time of flight (2.9), the determination of the component V_{0x} of the recoil ion along the extraction axis seems not so simple. In practice, though the V_{0x} can be numerically given, it is possible to obtain an approximate analytical solution, indeed. Because the electric extraction field is much larger than the initial kinetic energy of recoil ions, the time of flight equation (2.9) is simplified by the approximation to the square root terms. Then the evolution of the time of flight of recoil ions becomes a linear function of the initial velocity:

$$\frac{1}{2}m_i {V_{0x}}^2 \le \frac{1}{2}m_i {V_0}^2 << q_i E_1 (L_1 - x_0) \quad \text{then} \quad {V_{0x}}^2 << \frac{2q_i E_1 (L_1 - x_0)}{m_i} \tag{3. 13}$$

in this case, the time of flight equation can be expressed as

$$TOF_{i\_approx} = \frac{m_i}{q_i E_1}\left(V_{0x} + \sqrt{\frac{2q_i E_1 (L_1 - x_0)}{m_i}}\right) + \frac{L_2}{\sqrt{\frac{2q_i E_1 (L_1 - x_0)}{m_i}}} + \frac{m_i}{q_i E_3}\left(-\sqrt{\frac{2q_i E_1 (L_1 - x_0)}{m_i}} + \sqrt{\frac{2q_i E_1 (L_1 - x_0)}{m_i} + \frac{2q_i E_3 L_3}{m_i}}\right)\Bigg\} \tag{3. 14}$$

or

$$TOF_{i\_approx} = \frac{m_i}{q_i E_1} V_{0x} + TOF_{i0} \tag{3. 15}$$

where

$$TOF_{i0} = \frac{m_i}{q_i E_1}\sqrt{\frac{2q_i E_1 (L_1 - x_0)}{m_i}} + \frac{L_2}{\sqrt{\frac{2q_i E_1 (L_1 - x_0)}{m_i}}} + \frac{m_i}{q_i E_3}\left(-\sqrt{\frac{2q_i E_1 (L_1 - x_0)}{m_i}} + \sqrt{\frac{2q_i E_1 (L_1 - x_0)}{m_i} + \frac{2q_i E_3 L_3}{m_i}}\right)\Bigg\} \tag{3. 16}$$

then finally

$$V_{0x} = \frac{q_i E_1}{m_i}(TOF_{i\_approx} - TOF_{i0}) \tag{3. 17}$$

This linear approximation satisfies the time of flight equation with less than 0.5% error at 50eV initial kinetic energy. This error is smaller (larger) for lower (higher) kinetic energies.

The determination of the components V_{0y} and V_{0z} is more straightforward. Considering the flight time of recoil ion when they move on a distance of (Y_i-Y_0) and (Z_i-Z_0), the velocities are given as follows:

$$V_{0y} = \frac{(Y_i - Y_0)}{TOF_i} - V_{jet} \tag{3. 18}$$

$$V_{0z} = \frac{(Z_i - Z_0)}{TOF_i} \tag{3. 19}$$

where V_{jet} is the velocity of the target supersonic gas jet. This velocity can be calculated from the detected positions of target gas ions and from residual gas ions (figure III-7a). The non-dissociated

molecule NO_2^+ moved from the collision point along Y axis because of its initial velocity V_{jet}. By substituting the time of flight of NO_2^+, the measured value of Vjet is deduced in m/sec (see table II-1 for the excepted theoretical value):

$$V_{jet} = (4.3-(-5.0))\times 0.267\times 10^{-3}/(3.361\times 10^{-6}) \approx 734.0 \pm 160 \qquad (3.20)$$

III.3 Calibration of the 3D-focusing Spectrometer

Without field free region, the spectrometer calibration for HDO experiment is simpler than that for NO_2. The absolute time-zero, Toffset, and the extraction field strength can be calibrated together by the same procedure that uses a fitting function of recoil ion TOFs. The strong advantage of this setup is that each dissociation channel can be separated from the others only by the momentum conservation law, as long as all fragments are detected.

III.3.1 Time Of Flight and the Extraction Field Strength

The flight time of which initial velocity was zero (TOF_0) for this spectrometer setup is calculated from (2.6), (2.7):

$$TOF_{v0x=0} = \sqrt{\frac{m}{q}}\left\{\frac{1}{E_1}\sqrt{2E_1(L_1-x_0)} + \frac{1}{E_3}\left(-\sqrt{2E_1(L_1-x_0)}+\sqrt{2E_1(L_1-x_0)+2E_3L_3}\right)\right\} \qquad (3.21)$$

The same procedure as described in the section III.2.1 has been followed. We choose some ions from the TG_DI spectrum and plot the TOFs as a function of the square root of the mass over charge ratio. The raw TG_DI spectrum and the selected ions distributions are shown in figure III-9. a, b with gaussian fitting. It is clearly observed here that the flight time distribution in this experiment is about ten times wider than the NO_2 experiment. This is due to the missing ""time focusing" property of the spectrometer. The calibrated equation is then (figure III-9):

$$TOF_{v0x=0}[\mathrm{sec}] = 2012.7\sqrt{m/q}\cdot C_{TDC} \qquad (3.22)$$
$$T_{offset} = 16723$$

As was mentioned above, the flight time of post-acceleration zone (T_3) is much shorter than that of the extraction zone (T_1). The ratio of T_3 to T_1 in the case of zero initial velocity is given by:

$$\frac{T_3}{T_1}=\frac{E_1}{E_3}\left\{-1+\sqrt{1+\frac{E_3 L_3}{E_1 L_1}}\right\} \tag{3. 23}$$

Substituting the measured values, E_1=20.1V/cm, E_3=375000V/m, L_1=98.2mm, L_3=8mm, the contribution of the post-acceleration zone to the flight time of extraction zone is only 1.6%. This ratio obviously depends on the initial velocity in practice. The larger the initial velocity along the recoil ion detector direction (X axis) the fragment, the larger the contribution of the flight time of the post-acceleration. In the case of the HDO^{2+} fragmentation with 10eV of Kinetic Energy Release, if the dissociated H^+ ion has its velocity along the X axis, $v_{0x}=4.0\cdot 10^4 m/s$, then the ratio T_3/T_1 = 2.0%. To simplify the data treatment, we decide to use the average amount 1.6% for T_3 to calculate the extraction field strength.

In the case of the HDO experiment, it is rather simple to determine E_1 since the second term of TOF equation corresponding to the field free region is suppressed. From the above-mentioned discussion, we have the following equality

$$A\sqrt{\frac{m}{q}}\left\{\frac{1}{E_1}\sqrt{2E_1(L_1-x_0)}\right\}=2012.7\sqrt{\frac{m}{q}}\cdot C_{TDC}\cdot\frac{1}{1+0.016} \tag{3. 24}$$

where A is the conversion coefficient to MKSA unit. Then the obtained value for the extraction electric field strength is: 20.8 ± 0.1[V/cm].

III.3.2 Collision Point

As the experiment involves ion-ion coincidence, the collision point can be precisely calculated for each event. The basic idea behind is momentum conservation between fragment ions. The position resolution is not limited, as usual, by the overlap between the projectile beam and the supersonic gas jet but by the ultimate resolution of the position sensitive detector. The fragment ion momentum in the center-of-mass frame are given by

$$\begin{cases} P_{iz}=m_i(z_i-z_0)/T_i \\ P_{iy}=m_i\left\{(y_i-y_0)/T_i-V_{jet}\right\} \\ P_{ix}=\dfrac{m_i}{T_i}(L_1-x_i)-\dfrac{1}{2}q_i E_i T_i \end{cases} \tag{3. 25}$$

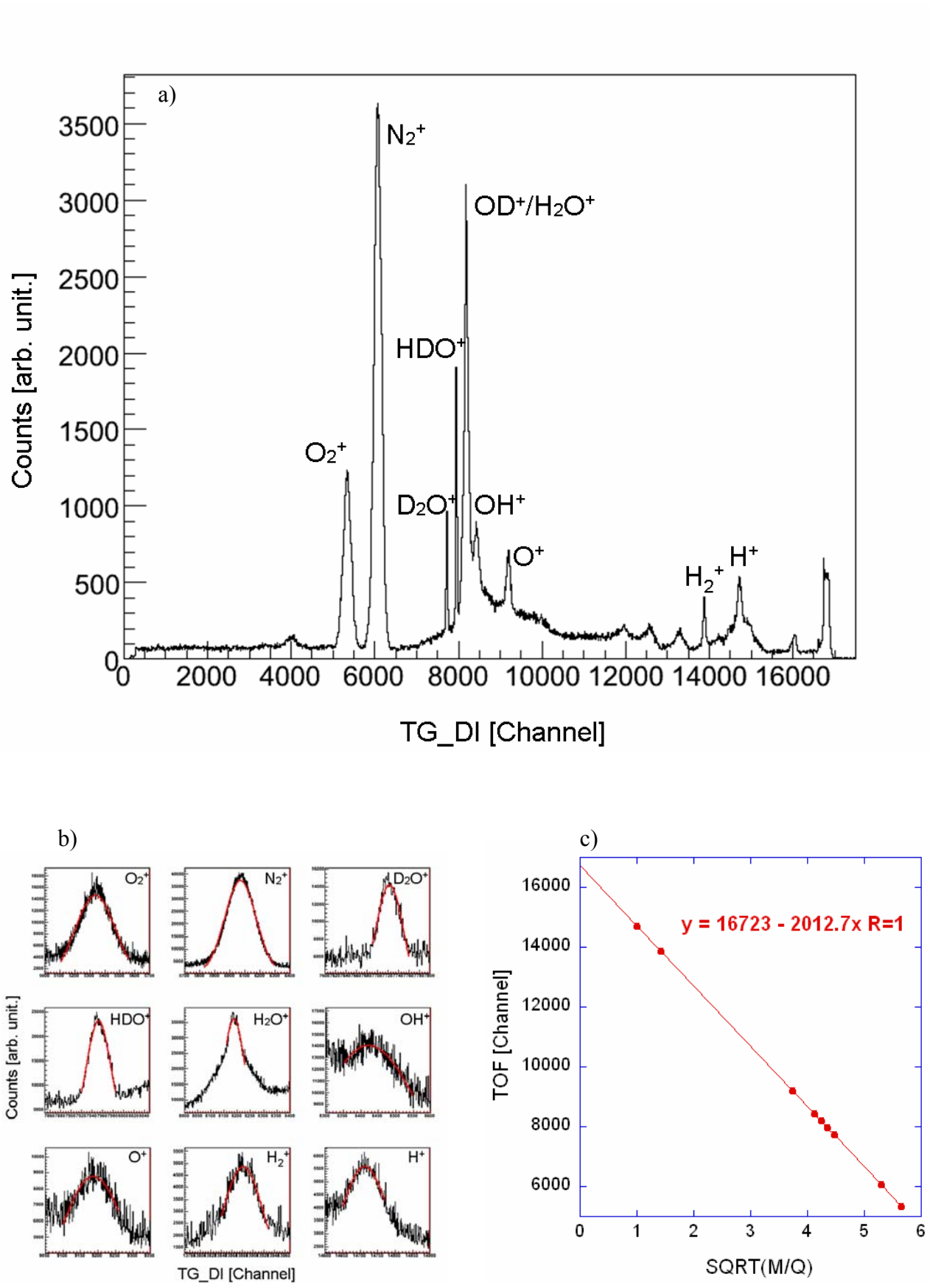

Figure III- 9 a) TG_DI spectrum of HDO experiment, b) selected peaks of recoil ions with a Gaussian fitting (red line), c) calibration equation using elected peaks

where index i indicates the fragment number. In the present experiment, since the target gas jet is very cold in the X and Z transverse directions, the center-of-mass velocity along these directions can be assumed to be zero. On the other hand, along the target gas direction (Y direction), fragments have the gas jet velocity V_{jet} as a center-of-mass velocity.

In the case of two-body fragmentation, the center-of-mass frame momentum conservation $\overline{P_1} = -\overline{P_2}$ allows elimination of the unknown parameters. In this experiment, the collision point z_0, y_0 and the absolute extraction length $L_0 = L_1 - x_i$ should be cancelled out to calculate the fragment momentum:

$$\begin{cases} P_{1z} = P_{2z} = \dfrac{m_1 m_2 (z_1 - z_2)}{m_1 T_2 + m_2 T_1} \\ P_{1y} = P_{2y} = \dfrac{m_1 m_2}{m_1 T_2 + m_2 T_1}\left\{ y_1 - y_2 - (T_1 - T_2) V_{jet} \right\} \\ P_{1x} = P_{2x} = \dfrac{m_1}{T_1} L_0 - \dfrac{1}{2} q_1 E_1 T_1 \end{cases} \tag{3. 26}$$

On the other hand, collision point coordinates can be provided by canceling out the momenta:

$$\begin{cases} z_0 = \dfrac{m_1 T_2 z_1 + m_2 T_1 z_2}{m_1 T_2 + m_2 T_1} \\ y_0 = \dfrac{1}{m_1 T_2 + m_2 T_1}\left\{ m_1 T_2 y_1 - m_2 T_1 y_2 - T_1 T_2 (m_1 + m_2) V_{jet} \right\} \\ L_0 = \dfrac{1}{2}\left(\dfrac{T_1 T_2}{m_1 T_2 + m_2 T_1} \right)(q_1 T_1 + q_2 T_2) E_1 \end{cases} \tag{3. 27}$$

These calculated collision point can be used as filters to perfectly identify a true event. Separating the target event from others is an essential of this experiment. In the COLTRIMS experiment, the dissociation channels of recoil ions are usually identified by coincident Time-Of-Flight map. However, as shown in figure III-10, the four dissociation channels of interest $H^+ + OD^+$, $D^+ + OH^+$, and $H^+ + OH^+$, $D^+ + OD^+$ have similar TOFs and are mixed with fragmentation channels coming from the background gas in the collision chamber. Considering the projectile-target collision point, most of the non-relevant events lead to wrong locations. In other words, proper events can be isolated by filtering the collision point distribution in three dimensions. Here the extraction of the $H^+ + OD^+$ dissociation channel is shown as an example (Figure III-10-12).

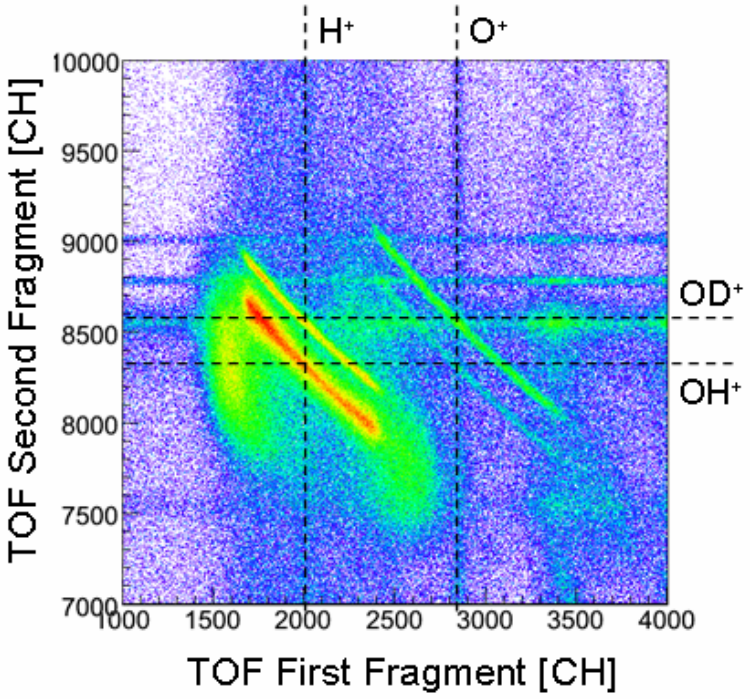

Figure III- 10 Time window for the dissociation channels of interest

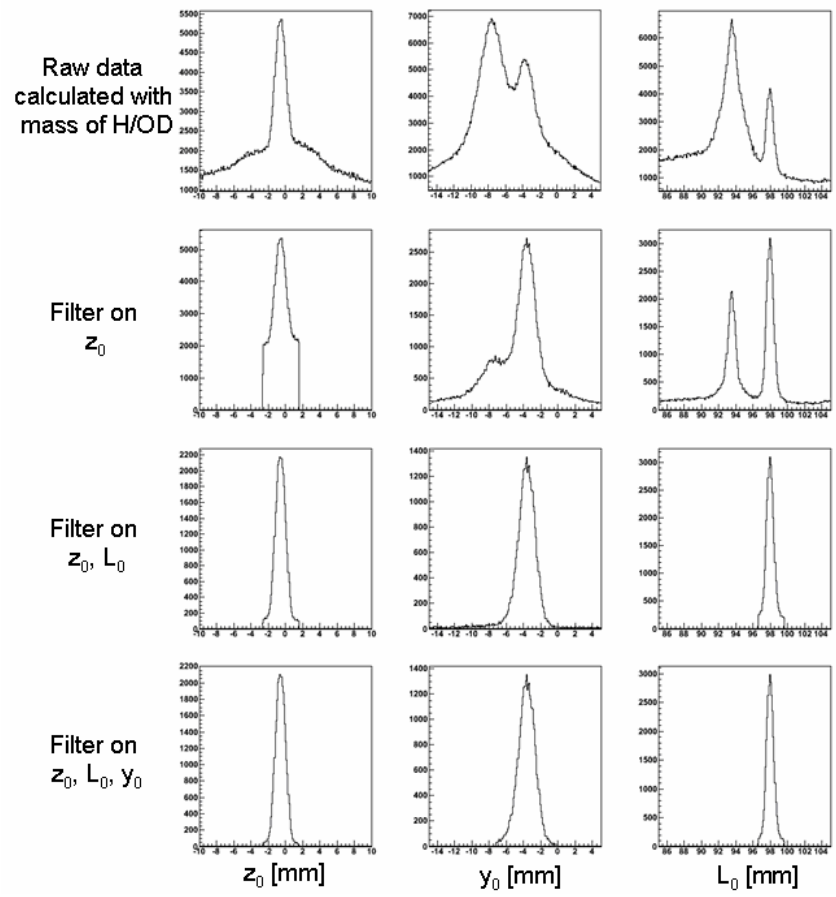

Figure III- 11 3D-filtering on collision point. The collision point components of events detected in the "time window (figure III-10)" are calculated with the mass H for the first fragment and OD for the second.

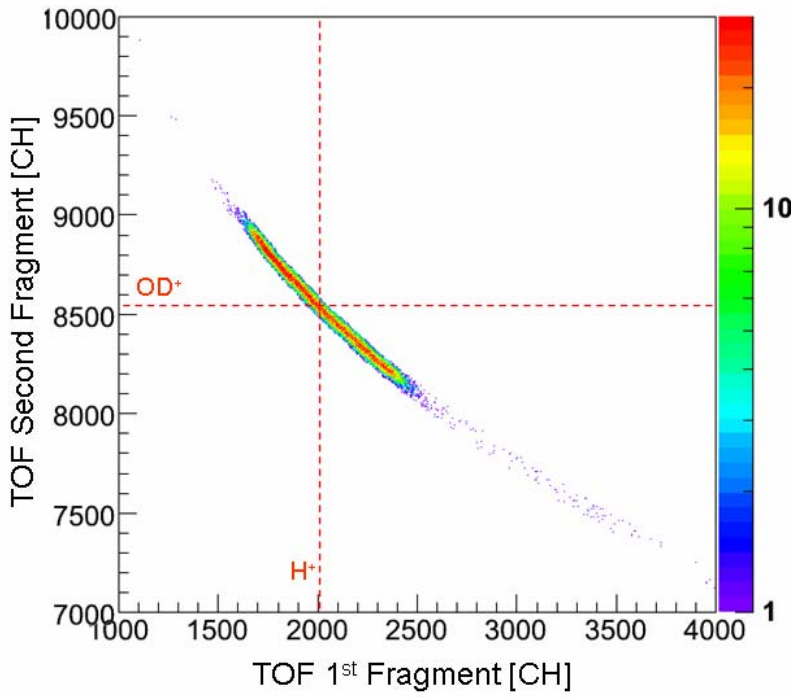

Figure III- 12 Extraction of the $H^+ + OD^+$ dissociation channels by 3D position filter (figure III-11)

This 3D filtering allows removing events arising from the residual gas as well as random coincidences i.e. the first and second fragment mass don't correspond to H and OD, respectively. We apply collision point filters one after the other on the total collected event in the "time window" shown in figure III-10. Based on the shape of distribution, Z_0 is the easiest component to start to filter condition. Then, considering the measured extraction length, L_0 should be distributed around 98mm. Then the y_0 distribution is cut to be Gaussian-like distribution. It is important to note that even z_0 is cleaned up by the following filters. Extra peaks shown in y_0 and L_0 spectra correspond to background molecules contribution and other dissociation channels (D^+/ OH^+, H^+/ OH^+ or D^+/ OD^+). The result is shown in figure III-12. In practice, the same steps with four different combination of fragment mass give four separated dissociation channels.

III.3.3 Low Energy Projectile Experiment HDO

The algorithm of data analysis process for the low energy experiment is subtly different. As was described in (section II-1.2), the trigger was generated by the projectile ion. Then the absolute time of flight of fragments is given by the timing differences between the projectile ion signal and the recoil ion signals:

$$TOF_i = T\_PROJ - TG\_DI_i + T_{offset} \quad (3.\ 28)$$

where T_{offset} is deduced to 1985.0.

Other parameters and observables are treated in same way as the HDO experiment with high energy projectile ion. It is important to note that of course the collision point filtering can be applied as well to this experiment.

§ IV NO_2 Fragmentation

Polyatomic molecule fragmentation has been attracting strong interest during the last years due to the advances in imaging techniques. The intent of our work was to address the atomic reactions involving nitrogen dioxide (NO_2), its dynamics, momentum sharing, geometrical structures and Kinetic Energy Release (KER). The current chapter is devoted to the presentation of the results of NO_2 fragmentation induced by fast ion impact (4.7MeV/u Ne^{8+}), and the comparison to linear triatomic molecule carbon dioxide (CO_2) presented in section I.3.

IV.1 Identification of dissociation channels

This identification of dissociation channels takes advantage of the coincident time of flight mass spectroscopy of the fragment. One of the most annoying drawbacks of this experiment is that the existence of nitrogen-nitrogen and oxygen-oxygen event from residual gas in the reaction chamber. At first glance, the Ion-Ion-Coincidence spectra (figure IV-1, 2, 3) from this experiment shows that the $NO_2^{2+} \rightarrow NO^+ + O^+$ (region (a) on the figure IV-1) is the most frequent event in this experiment. It shows also some intense regions as (b): (N^+/N^+), (N^+/O^+), (O^+/O^+) and (c): (N^{2+}/N^+), (O^{2+}/N^+), (O^{2+}/O^+). The sharp diagonal lines shown in the coincidence map of the first and the second fragment signify that the molecular momentum was shared equally between two fragments. These diagonal lines of (N^+/N^+) and (O^+/O^+) in the region (b) or (N^{2+}/N^+) and (O^{2+}/O^+) in the region (c), and also (N^{3+}/N^+) and (O^{3+}/O^+) evidence that the events come from the residual N_2 and O_2 gas fragmentation. On the other hand, the elliptical distribution is an existence proof of a third fragment. The ratio of the number of triple coincidence detected over double coincidence is only 6.3 percent[1]. These two regions can be recognized as the fragmentation channels from the target NO_2 gas jet even if some cleaning up is required. It has to be mentioned here that there is also the possibility of three-body breakups without detecting the third fragment, i.e. the fragmentation involving

[1] This does not mean the ratio of actual event of three-body breakups to two-body. Due to the detector efficiency, undetected rate of triple coincidence measurement is about 50% higher than double coincident measurement.

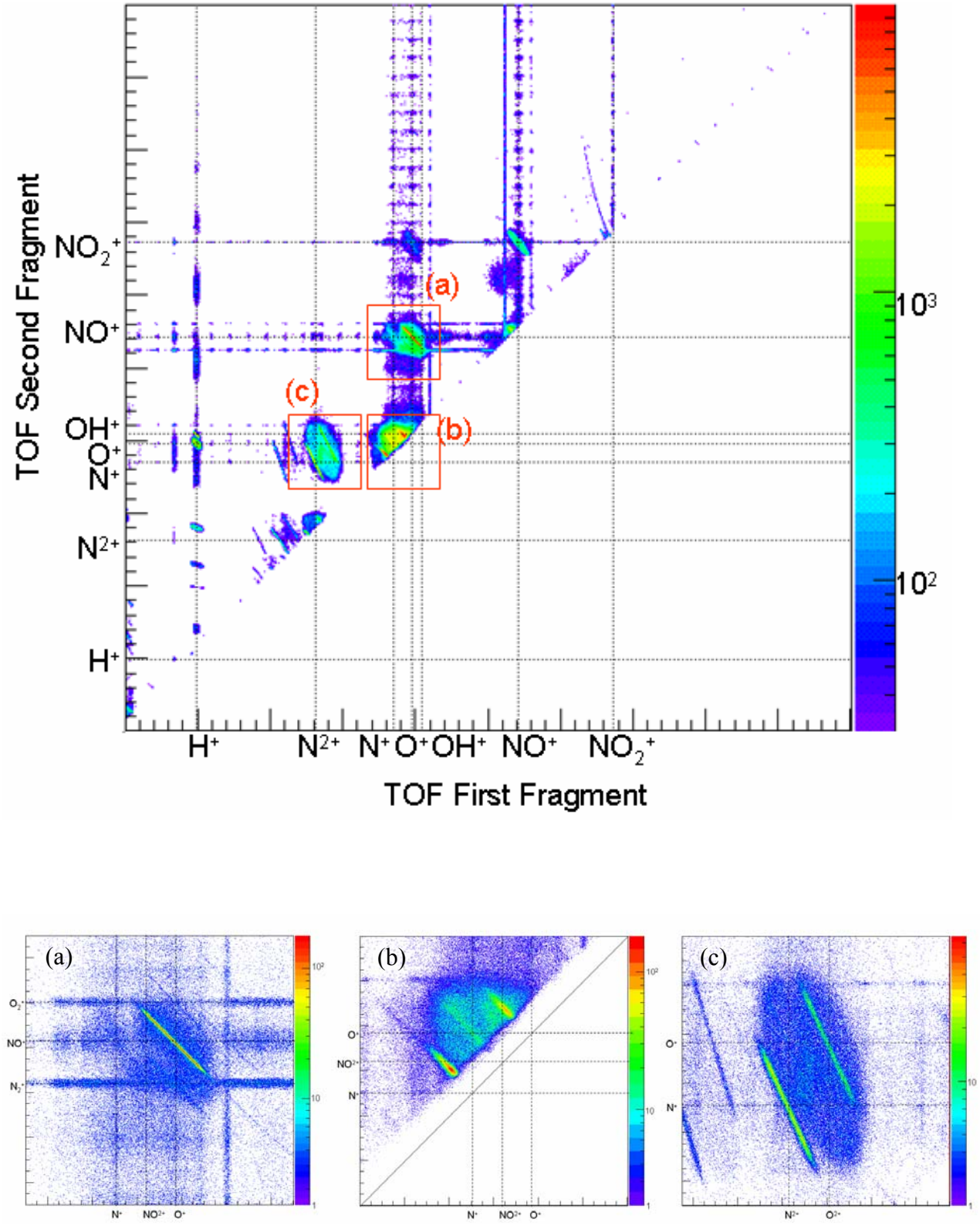

Figure IV- 1 Coincidence Map of the 1st and 2nd fragment emitted by NO_2 target molecule collision with 4.7MeV/u Ne^{8+}, when more than two fragments are detected. The TOF_0 (initial velocity along electric extraction field is zero) of fragments are indicated with dotted lines. False coincidence events measured by a cyclotron high frequency (≈90nsec) are also shown.
Bottom: magnified figures of the regions (a) O^+/NO^+, (b) N^+/N^+, N^+/O^+, O^+/O^+ and (c) N^{2+}/N^+, O^{2+}/O^+, N^{2+}/O^+, $O^{2+}/N+$.

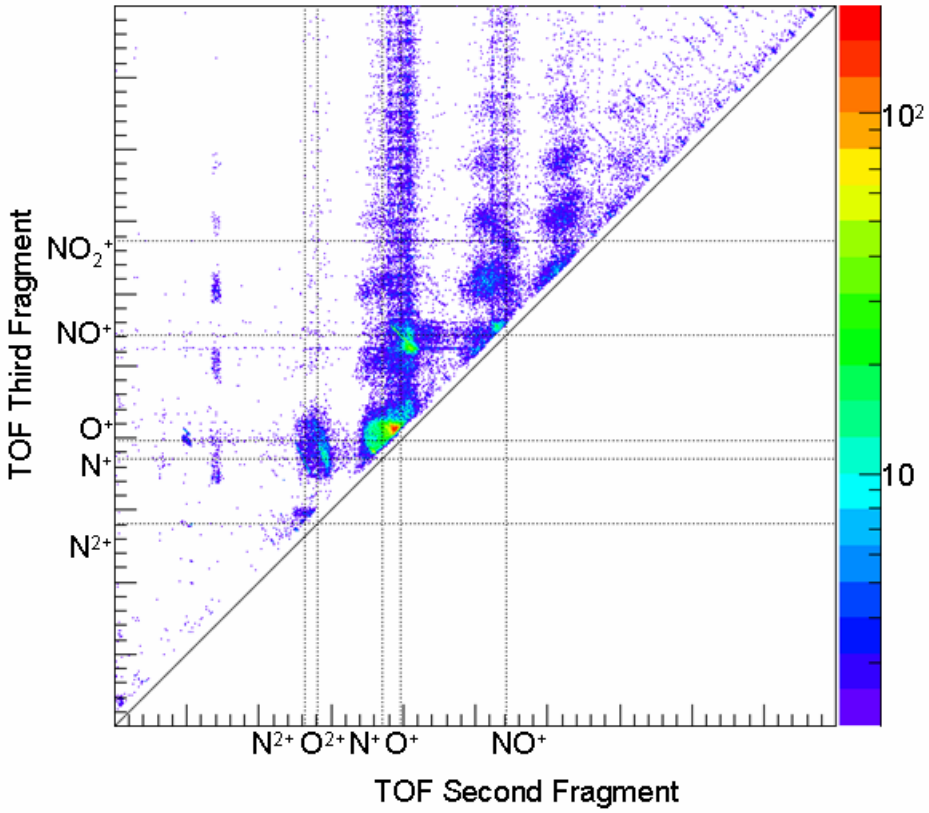

Figure IV- 2
Coincidence map of the 2nd and the 3rd fragments when more than three fragments are detected.

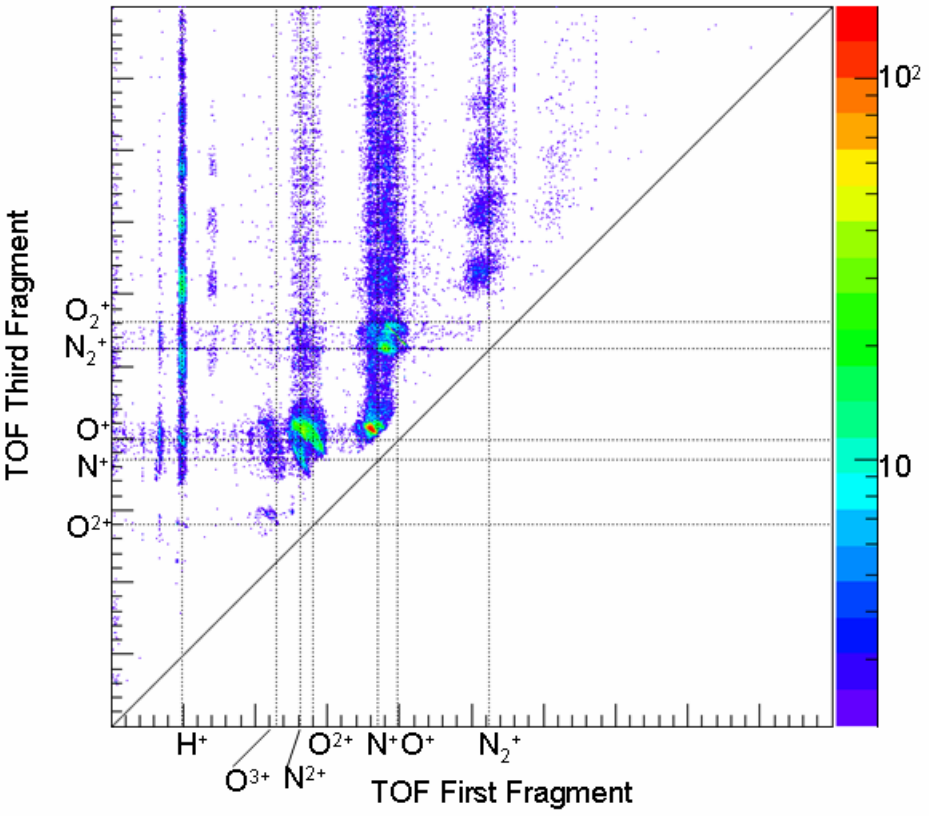

Figure IV- 3
Coincidence map of the 1st and the 3rd fragments when more than three fragments are detected.

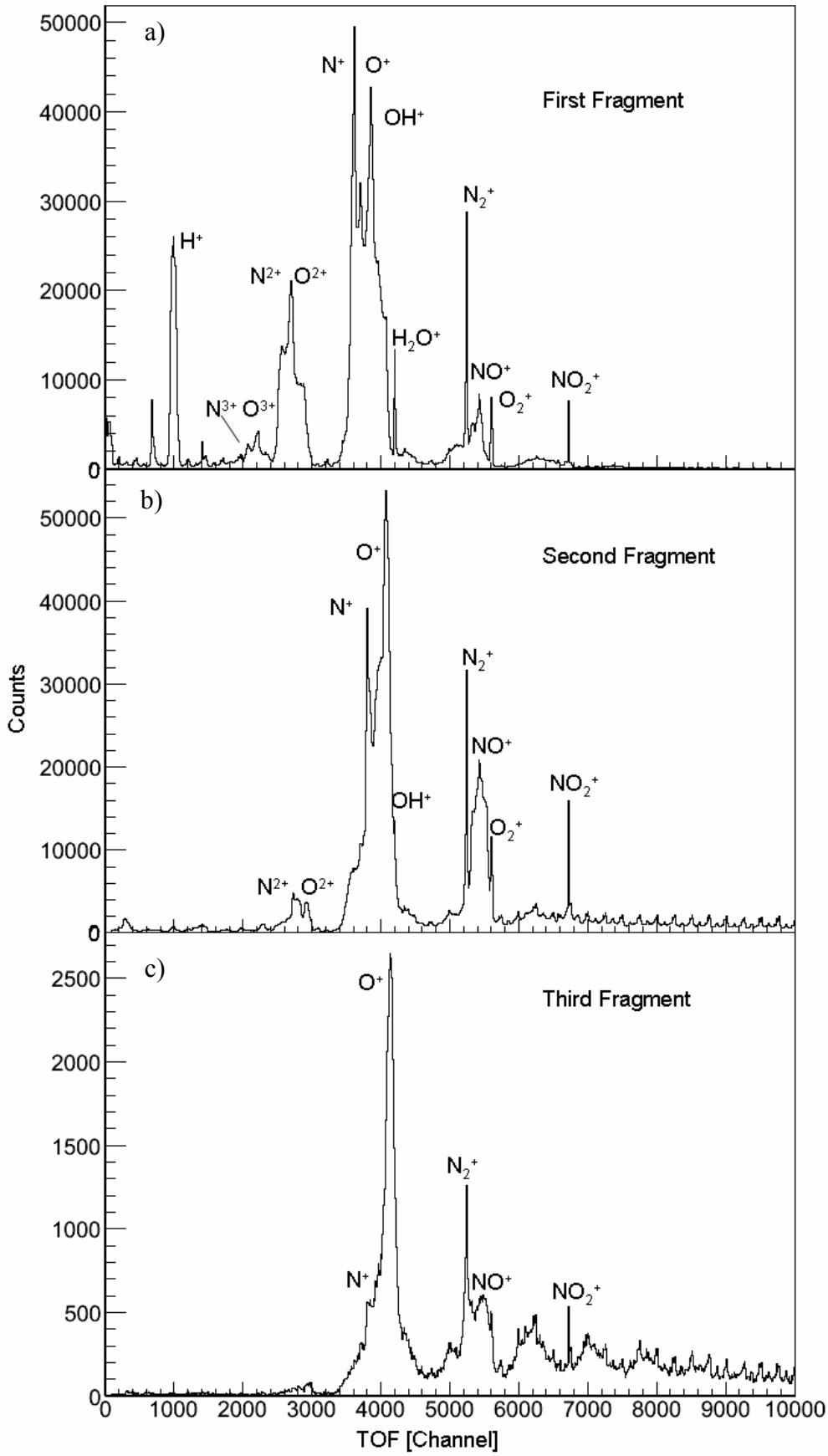

Figure IV- 4 1D time of flight spectrum of the 1st fragment a) and the 2nd fragment b) when more than two fragments are detected, and the third fragment when more than three fragments are detected.

a neutral particle. As was described in section II.2 and III.2, the presence of dimer (N_2O_4) in the target gas jet makes the analysis cumbersome and complicated (see Appendix A and B), as some of events detected in the region (a), (b) and (c) could come from N_2O_4 dissociation. The momentum conservation will help us to separate events involved in NO_2 from N_2O_4 only when all fragments of NO_2 are detected. It is not so simple to identify the dissociation channels generating a neutral fragment such as $NO_2^{2+} \rightarrow N^+ + O^+ + O$ as CO_2 experiment. The dissociation channels generated only by N_2O_4 are also detected such as (NO^+/NO^+), (NO_2^+/NO^+), (NO_2^+/NO_2^+). Figure IV-5 shows a zoom of coincidence map on this region. The interesting feature here is the long tail of NO_2^+/NO_2^+ dissociation channel unlike in the normal two-body breakup which shows sharp diagonal line. This wide distribution of time of flight is actually due to metastable $N_2O_4^{2+}$ ions which dissociates after certain time during its flight in the spectrometer. However, the singly charged parent fragment $N_2O_4^+$ ($TOF_0 \approx 9500$ch) wasn't observed.

Previously, a similar feature of a metastable molecular ion was observed at the ion-impact CO_2 experiment for the case of CO_2^{2+} dissociated into (CO^+/O^+) [ref.IV.1]. This dissociation channel was also measured by the photoionization [ref.IV.2] and electron impact [ref.IV.3]. The lifetime of the metastable molecular ion CO_2^{2+} was estimated to 900nsec.

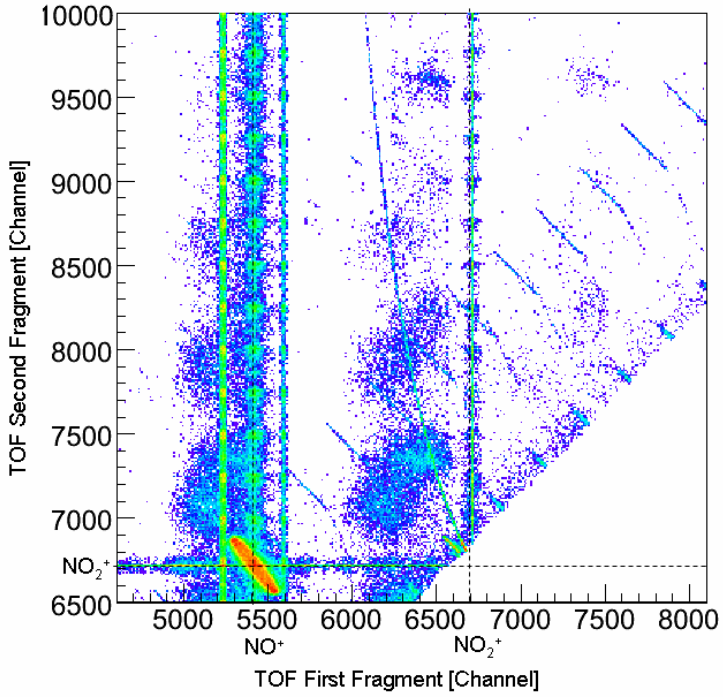

Figure IV- 5 Magnified figures of coincidence map of the 1st and the 2nd fragments. The dissociation channels from dimer N_2O_4 into (NO_{2+}/NO_2^+), (NO^+/NO_2^+) are observed

IV.2 NO^+/O^+ dissociation channel

The analysis of this double ionized two-body dissociation channel gives not only the scientific result of interest but also an indication of cleaning-up techniques to obtain proper results of three fragment systems. As was shown in figure IV-1, the detected events of NO^+/O^+ contain part of the fragment from N_2O_4. The correlation vectors described in the previous chapter make it possible to solve this problem. The proper gate is generated by calculating the sum of each momentum components of two fragments:

$$\sum_i P_i(x,y,z) = \sum_i (m_i \cdot v_i(x,y,z)) = 0$$

If a parent molecule after collision consists only of NO^+ and O^+, the sum of their momentum vectors will be distributed around zero following momentum conservation law. Otherwise the parent molecule has larger mass than NO_2. Figure IV-6 shows the momentum sum of (NO^+ /O^+) with and without filters (solid line and dotted line, respectively). The first gate is set to the momentum sum along extraction field which corresponds to the broadness of coincidence spectrum (sum of flight time) recognized visually in figure IV-7. Then the gates for momenta along Z and Y axis are set as explained in section III.5 and results are shown in figure IV-6. These distributions are obviously reflecting the target and projectile beam width respectively, and the full width of half maxima (FWHM) of momentum distributions (16.9 for Pz and 30.0 for Py) show the same ratio as the actual beam size described in the section III-2.

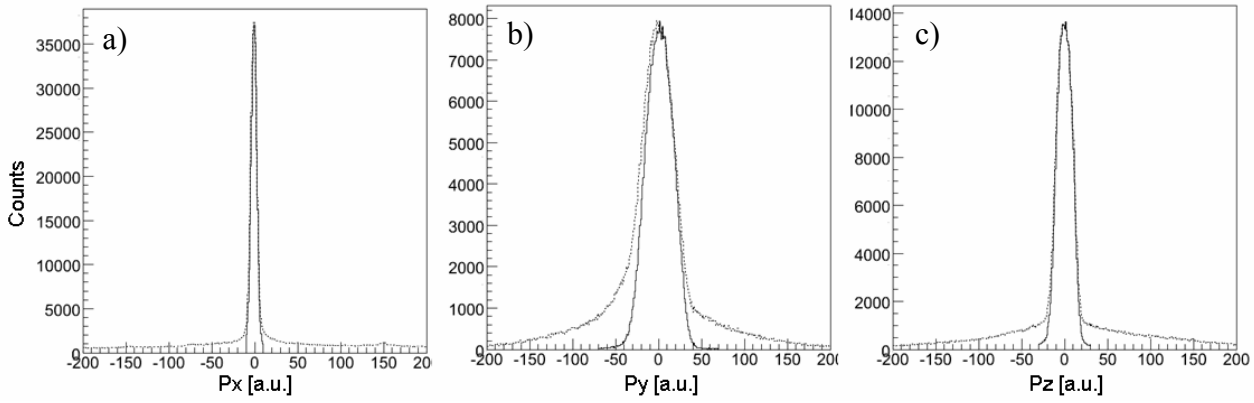

Figure IV- 6 Momentum sum of the fragments (NO^+ /O^+) without filter (dotted line) and after filtering on the three of components (solid line). First the gate was set on the P_x (along the extraction electric filed direction), then P_z (projectile beam direction), then P_y (target gas direction) were decided one by one.

The mean value of kinetic energy release of this dissociation channel has been reported by J. H.D. Eland [ref.IV.4] and also by T. Masuoka and A. Kobayashi recently [ref.IV.5]. He only measured time of flights of fragments induced by photoionization dissociation. Thus the KER was calculates only by one momentum components. Their estimated mean KER value was 6.7±0.5eV. Our

measurement here, the momentum components of all the fragments can be measured by multi-hit flight time and position detection technique. Then the KER of the system can be obtained from the sum of kinetic energy of fragments:

$$KER = \frac{1}{2}\sum_i \frac{P_i(x,y,z)^2}{m_i}$$

The energy spectrum of $NO_2^{2+} \rightarrow NO^+ + O^+$ is shown in figure IV-8. The reaction begins to appear about 2eV of KER then has a maximum peak at 6.7eV which agrees with Elands' result, and then decreases gently. It has to be noted that the fragments having larger kinetic energy than 11eV could not be under estimated because the fragments may arrive outside of the detector surface. This KER distribution will be used while discussing the dynamics of doubly charged three-body fragmentation in the section IV.5. The resolution of KER at 7eV is estimated to be around 250meV by the resolution of momentum.

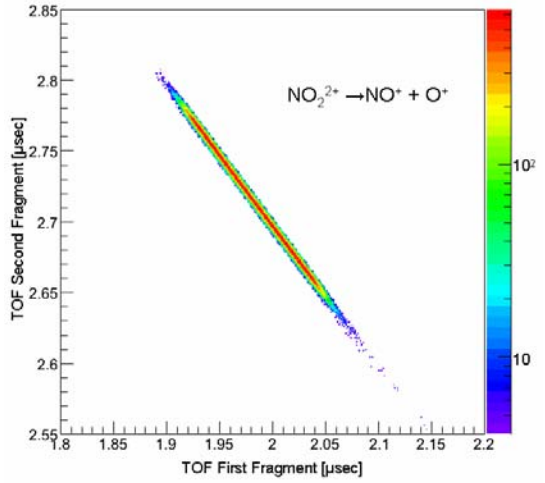

Figure IV- 7
Magnified figures of coincidence map of the 1st and the 2nd fragments of the region of $NO_2^{2+} \rightarrow NO^+ + O^+$ dissociation channel after filtering. The proper events are extracted by the filters on the momentum sum.

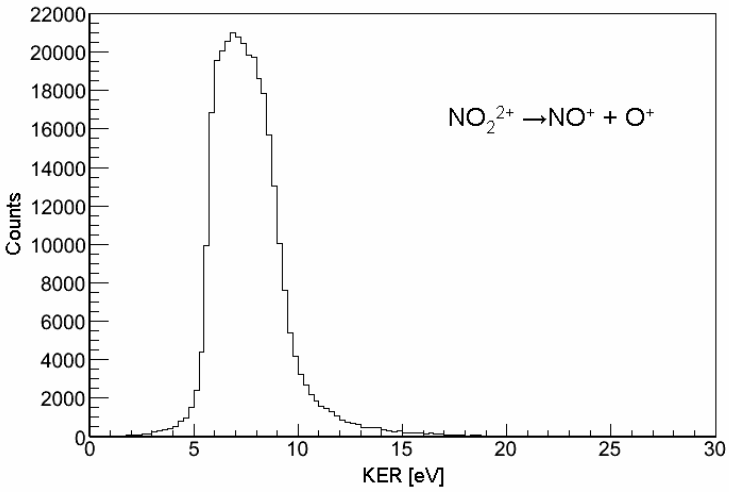

Figure IV- 8
KER distribution of dication two-body dissociation channel induced by 4.7MeV/u Ne^{8+}. The events having large KER (KER>11eV) might arrive outside of the MCP surface then not be detected.

IV.3 Analysis Method of Three-Body fragmentation of Triatomic Molecules

To reveal the dynamics of triatomic molecule fragmentation into three charged fragments or two charged and one neutral particle, momentum correlation of three particles has to be represented. The purpose of this paragraph is to provide the representation methods we adopted: 1. angular distribution, 2. Newton diagram, and 3. Dalitz plot.

IV.3.1 Angular Distributions

The geometry of this three particle system is defined by the angle between velocity vectors of two oxygen particles (O^+ /O^+or O^+/O) named θ. The fragments are numbered in order of arrival time i.e. 1. N^+, 2. first O^+, 3 second O^+ or undetected neutral O.

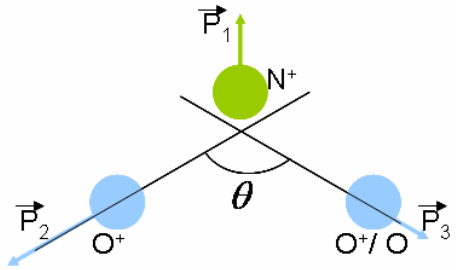

$$\theta = \cos^{-1}\frac{\vec{P}_2 \cdot \vec{P}_3}{\left|\vec{P}_2\right|\left|\vec{P}_3\right|}$$

Figure IV- 9 Definition of the angle θ

The angle θ is obviously related to the bond angle of the neutral molecule which is 134 degrees for nitrogen dioxide. If the fragmentation is synchronous concerted type, it is expected that the distribution of θ will be around this bond angle.

IV.3.2 Newton Diagram

In order to study the vector correlations among fragments, the Newton diagram is commonly used. This diagram is a representation of momentum vectors of each fragment in the momentum space defined by the axes P_x and P_y. In the present work, the momenta are represented in molecular frame and its axes are operationally defined resulting in canceling the sum of each momentum component in the diagram. Considering the symmetric geometry of neutral nitrogen dioxide, i.e. a nitrogen atom in between two oxygen atoms, we choose the N^+ momentum direction as Px axis of the diagram. Then the second fragment (or detected oxygen ion for N^+/ O^+ double coincident events) defines Py positive half plane. Each momentum components are then converted as follows:

$$P_{1x} = P_1 \qquad P_{1y} = 0$$

$$P_{2x} = P_2 \cos\varphi_2 = m_2 \frac{\vec{v}_1 \cdot \vec{v}_2}{|\vec{v}_1|} \qquad P_{2y} = P_2 \sin\varphi_2 = \sqrt{P_2^{\,2} - P_{2x}^{\,2}}$$

$$P_{3x} = P_3 \cos\varphi_3 = m_3 \frac{\vec{v}_1 \cdot \vec{v}_3}{|\vec{v}_1|} \qquad P_{3y} = P_3 \sin\varphi_3 = -\sqrt{P_3^{\,2} - P_{3x}^{\,2}}$$

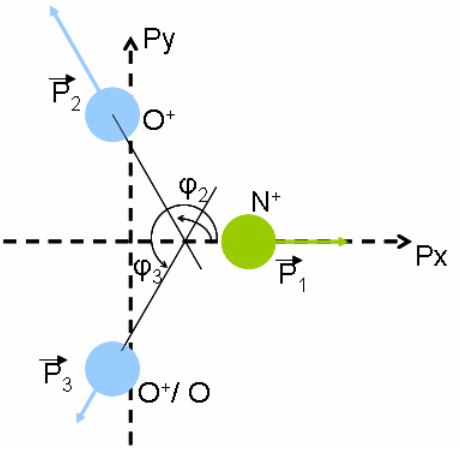

Figure IV- 10 Definition of the Newton diagram

where φ_i is the angle defined by the momentum direction respect to N^+ direction. Hereby the momentum distributions of three fragments are contained in a diagram.

IV.3.3 Dalitz Plot

Another approach to understanding energy correlation of three fragments called Dalitz plot is adopted [ref.IV.6-9]. This new reference frame represents also the geometric distribution of fragments. We first define reduced energy of fragment in molecular frame:

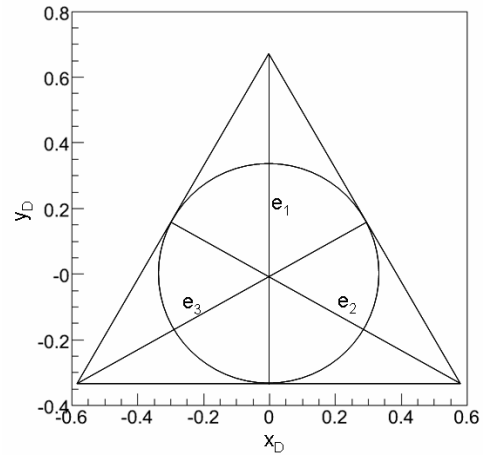

$$e_i = \frac{|P_i|^2}{\sum_i |P_i|^2}$$

Figure IV- 11
Definition of the Dalitz plot.

Due to the linear dependence of three fragments: $\sum_i e_i = 1$, the energy correlation can be represented in the 2D Cartesian coordinate system defining following axes (see figure IV-11):

$$x_D = \frac{e_2 - e_3}{\sqrt{3}}, \quad y_D = e_1 - \frac{1}{3}$$

The coordinates (x_D, y_D) are defined so that the configuration (0, 0) corresponds to the case of an equal sharing of the KER on the three fragments. The kinetic energy axes e_i are then shown as three bisectors of the equilateral triangle crossing at its center with an angle 120 degrees. Due to the momentum conservation among the fragments, the kinetic energy is distributed inside a circle in the equilateral triangle whose contour corresponds to the modes of dissociation where the molecule is perfectly linear. Figure IV-12 shows the corresponding configurations of momentum vectors of fragments on Dalitz plot [ref.IV.10,11]. The case A on figure V-12 corresponds the symmetrical breakup leaving the fragment 1 surrounded by fragments 2 and 3 on both sides (3-1-2) without any momentum. The case E and D indicate same mechanism but different order of fragment as 1-3-2 and 3-2-1, respectively. The fragmentation of three particles into two-body is shown at B: 2-(1-3), C: 3-(1-2) and F: 1-(2-3), as well.

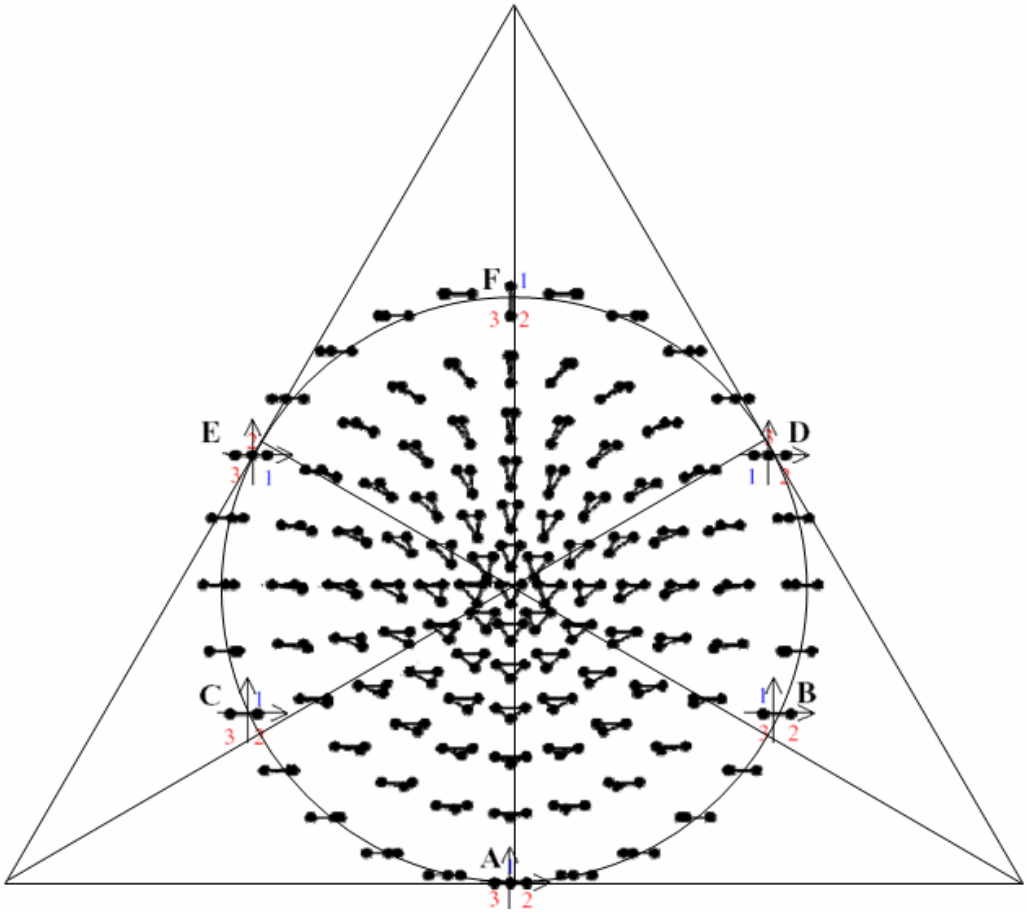

Figure IV- 12 The configurations of momentum vectors of fragments on Dalitz plot based on the explosion image.

IV.4 $N^+/ O^+/ O^+$ dissociation channel

This fragmentation channel can be identified clearly due to triple coincident measurement: N^+ detected as the first fragment and two O^+ as the second and third fragment. We have revealed the fragmentation aspects of this channel by several analysis methods presented in the previous paragraph.

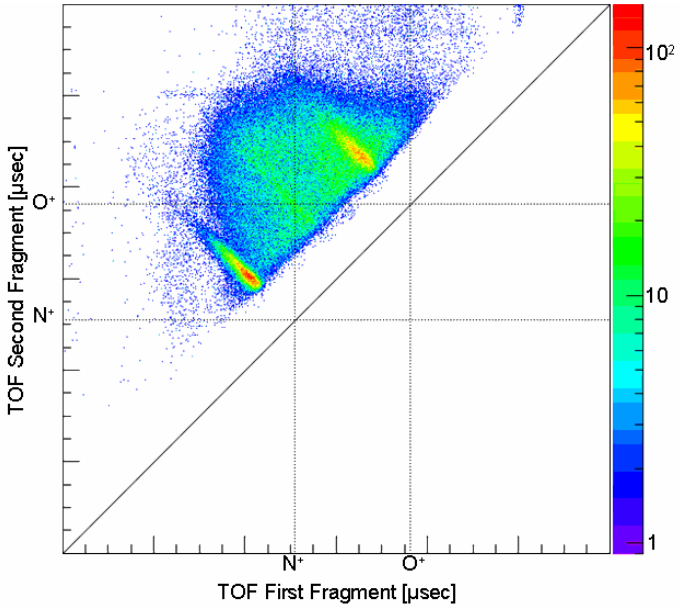

Figure IV- 13 Magnified coincidence map of the 1st and the 2nd fragment.

IV.4.1 Identification of the dissociation channel

Because of random coincidence, ($N^+/ O^+/ O^+$) are detected not only as the first to third hits but sometime as the second-fourth or third to fifth fragments when some lighter particles hit the detector. To make maximum use of triple coincident event, the following analysis is applied to the case when three fragments are detected in the time window shown in figure IV-13. One of the difficulties of detecting N^+ and O^+ ions come from their closely distributed time of flight. The involved events for which N^+ ions emitted in the opposite direction to extraction field ($v_x<0$) can not be detected easily. This is because flight times of backward-emitted N^+ and forward-emitted O^+ ions almost overlap. Thus the time difference between two fragments is smaller than the dead time of the TDC. Nevertheless this fact doesn't cause a crucial problem in studying the fragmentation dynamics of triple ionized three-body dissociation since these events are distributed isotropically. The time of flight distribution and coincidence map of effective events filtered by the sum of momentum components are presented in figure IV-14 and IV-15.

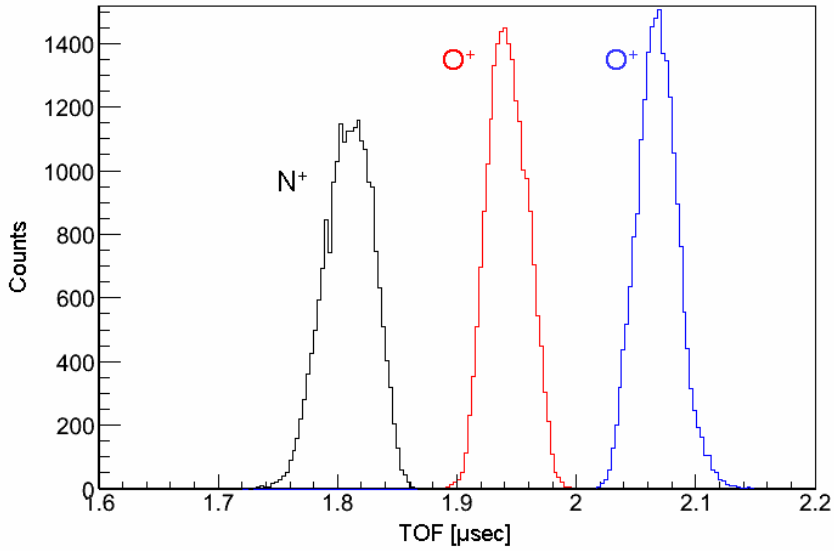

Figure IV- 14 Filtered Time Of Flight spectra of the N^+ (black), O^+ (red) and O^+ (blue) fragment when three fragments are detected on the window (figure IV-13).

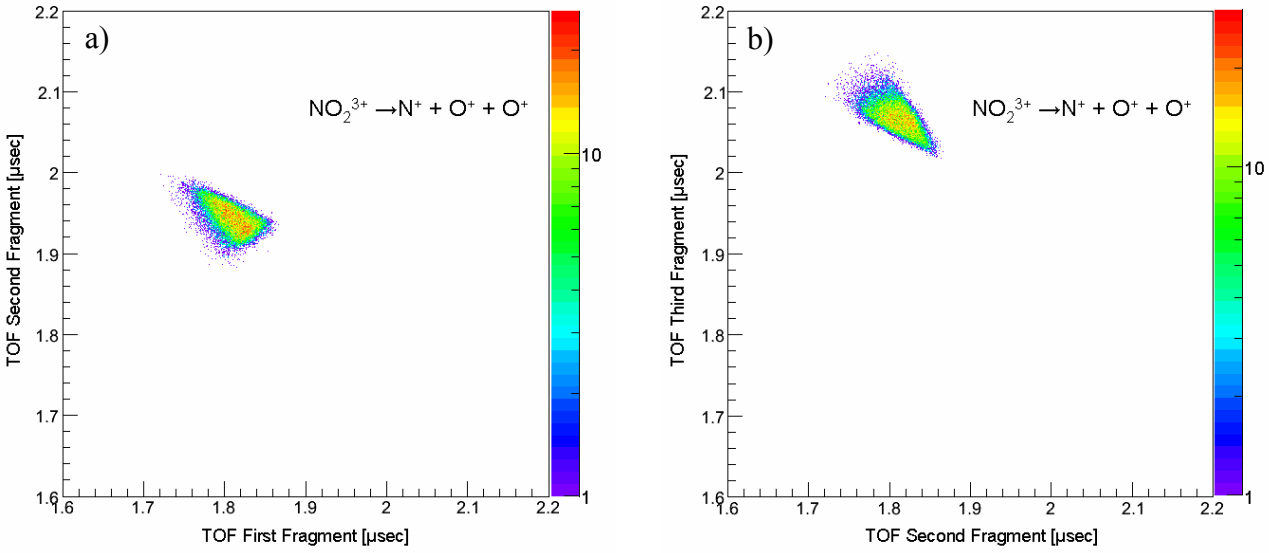

Figure IV- 15 Coincidence map of the NO_2^{3+} fragmentation of a) the 1st and the 2nd fragments and b) the 2nd and the 3rd fragments after filtering by momentum sum.

IV.4.2 Angular Distribution

Since these fragments correspond to a high charge state of the transient molecular ion (NO_2^{3+}), it can be expected that the system keeps the bond angle close to the one for neutral NO_2:

134 degrees. Figure IV-16 represents the measured angular distribution θ defined as the angle between the momentum vectors of the two oxygen ion fragments. It has to be pointed out that the mean value of measured θ is about 4% smaller than the ground-state bond angle. It is in fact due to the presence of repulsion among fragments expected from a Coulomb explosion. The same order of disagreement has been revealed in CO_2^{3+} dissociation into (C^+/ O^+/ O^+). Normally the linear molecule CO_2 has four normal vibrational modes and this configures bond angle distribution of CO_2 ground state (thick line in figure IV-16.b) shift from 180dgree to 172.5degree [ref.IV.12]. This distribution supports the idea that the triple-ionized three-body fragmentation behaves as a synchronous concerted fragmentation.

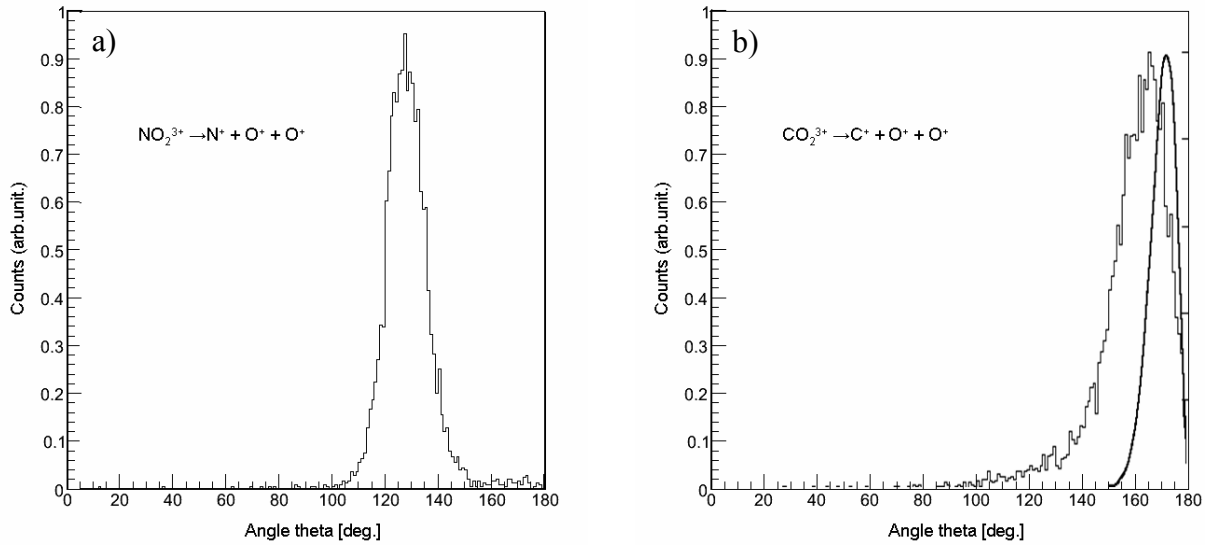

Figure IV- 16 Angular distribution of triple ionized dissociation channel for the case of a)NO_2 collision with 4.7MeV/u Ne^{8+} and b) CO_2 collision with 8MeV/u Ni^{24+} with the calculated bond angle of the neutral ground state (thick line).

IV.4.3 Newton Diagram

Figure IV-17 shows the resulting Newton diagram of $NO_2^{3+} \rightarrow N^+ + O^+ + O^+$ breakup channel. Note that the y positive plane of the diagram is defined by the O^+ fragment having the larger kinetic energy. This is because if dissociation produces two identical fragments (two O^+ for the present study), the Newton diagram defined only by their time of flight creates an "artificial" symmetry. Indeed the difference between fragments having shorter and longer flight time comes solely from emission direction with respect to the detector, which plays of course no role in dissociation dynamics of interest.

The 1D momentum distribution of N^+ is also presented in the figure. The diagram clearly shows that two O^+ surround N^+ fragments on both side keeping a certain angular distribution (figure IV-16). The momentum values themselves of both O^+ fragments are similar to CO_2^{3+} dissociation channel. However, as was expected based on the momentum conservation law, the center fragment N^+ has a finite value (distributed between 100-200a.u.) in opposite direction to the two O^+ frag-

ments while C^+ in (C^+/ O^+/ O^+) system is nearly at rest (figure I-3). The diagram shows also that momentum of both O^+ fragments compensates each other in y direction. The dynamics of this dissociation channel is thus classified into the case of simultaneous N-O bond breakage named synchronous concerted fragmentation.

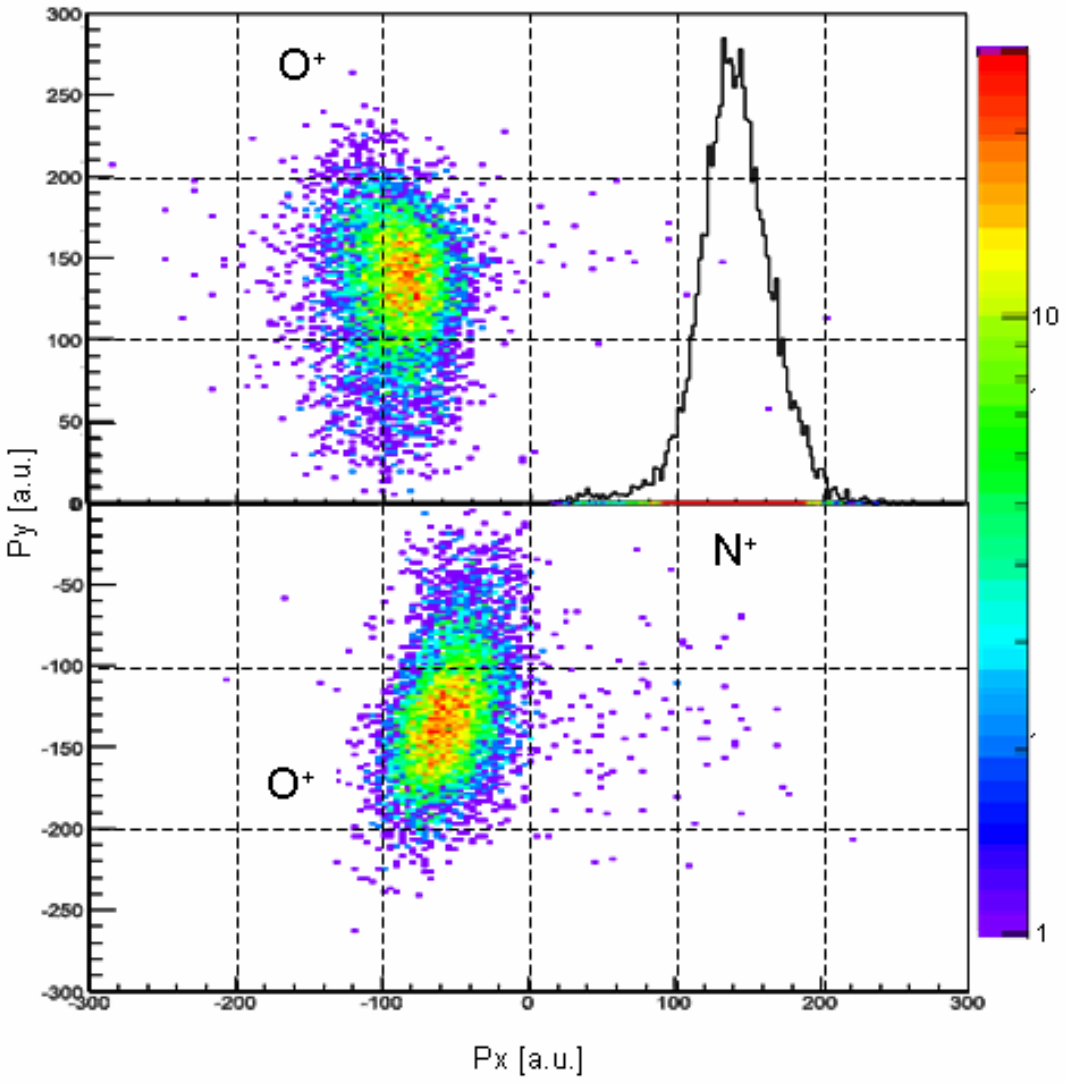

Figure IV- 17 Newton diagram of the NO_2^{3+} dissociation channel into $N^+/O^+/O^+$.

IV.4.4 Kinetic Energy Release

The KER of the $NO_2^{3+} \rightarrow N^+ + O^+ + O^+$ dissociation channel calculated as section IV.2 extends this KER from 10.5eV (minimum) to 84.0eV (maximum) with a peak centered around 33.5eV and an average energy of 35.8eV. It should be mentioned that all fragments remains within the detector aperture even at the maximum KER. In the following, more detailed dissociation patterns of the system as a function of KER will be presented.

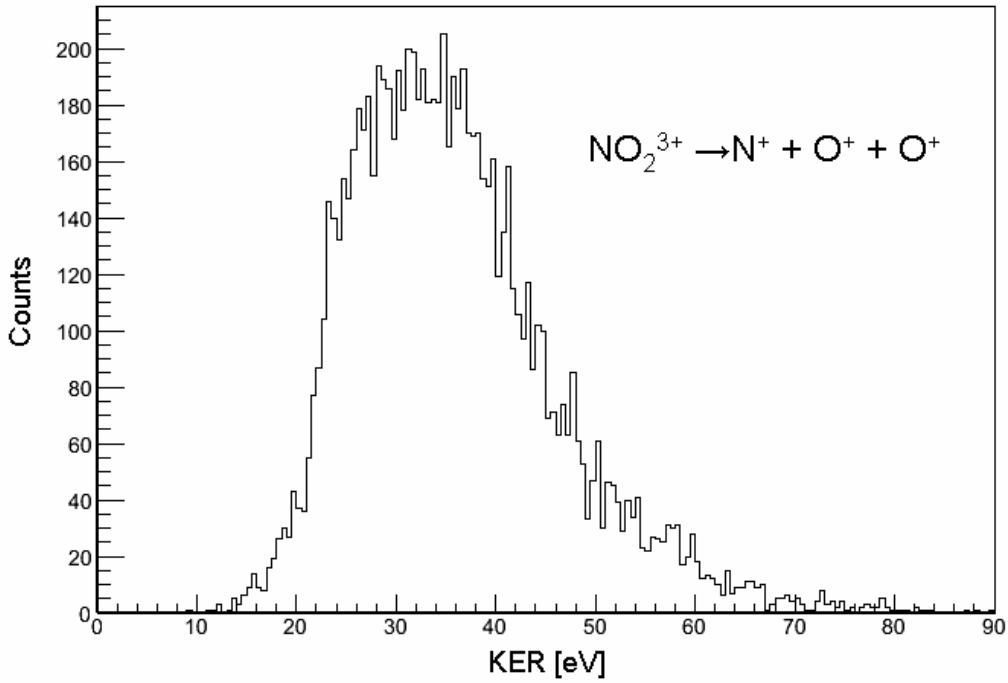

Figure IV- 18 Kinetic Energy Release distribution of the triply ionized three-body dissociation.

IV.4.5 Dalitz Plot

Other evidence of the simultaneous bond breakage keeping the angular distribution just after the collision is shown in figure IV-19. The Dalitz plot of $(N^+/ O^+/ O^+)$ channel is defined only on the x_D positive plane by definition, the second fragment is the O^+ ion having more energy than the other. One can clearly see that in most of the cases, events are distributed on the half circle centered at x_D=0, y_D=-0.1 corresponding to the bond angle≈134degree. This is in perfect agreement with the assumption of synchronous concerted fragmentation of the bent molecule NO_2. However, not all the events are gathered at this configuration, showing subtle structure at the upper right side and the center bottom on the circle. Considering the corresponding configurations of momentum vectors of fragments (figure IV-12), the upper right side structure indicates that the fragments 1 (N^+) and 3 (less energetic O^+) rotate as to be reversed position in the momentum space during the dissociation. In practice, taking a look to the filtered Newton diagram, the more energetic O^+ ion is repelled strongly and the other O^+ has very little impulse along N^+ momentum axis. One can thus suppose that some of breakups follow a particular dissociation scenario producing (NO^{2+}/O^+) intermediate step after the first bond breakage. Then the second bond breakage of $NO^{2+} \rightarrow N^+ + O^+$ occurs with rather long lifetime so that metastable molecular ion NO^{2+} has a time to rotate. The different life-time give the line structure along the e_2 axis. The question involved here is whether or not there is a

condition to select the dissociation scenario: simultaneous or sequential. The evolution of Dalitz plot with respect to KER answers this question. Figure IV-20 shows the Dalitz plots for different KER values of every 5eV. One can see that the "nose" structure corresponding to the sequential dissociation appears only at lower KER values (below 35eV). Thus the KER spectrum of (N^+/ O^+/ O^+) is made up of at least two overlapping components. The other structure at the center bottom region on the Dalitz plot comes obviously from dimmers N_2O_4. In the Dalitz plot of (N^+/ O^+/ O^+) for the case of the higher pressure target (5 bars compared to 2 bars), notably higher distribution is observed at the center bottom region (See Appendix A for more information).

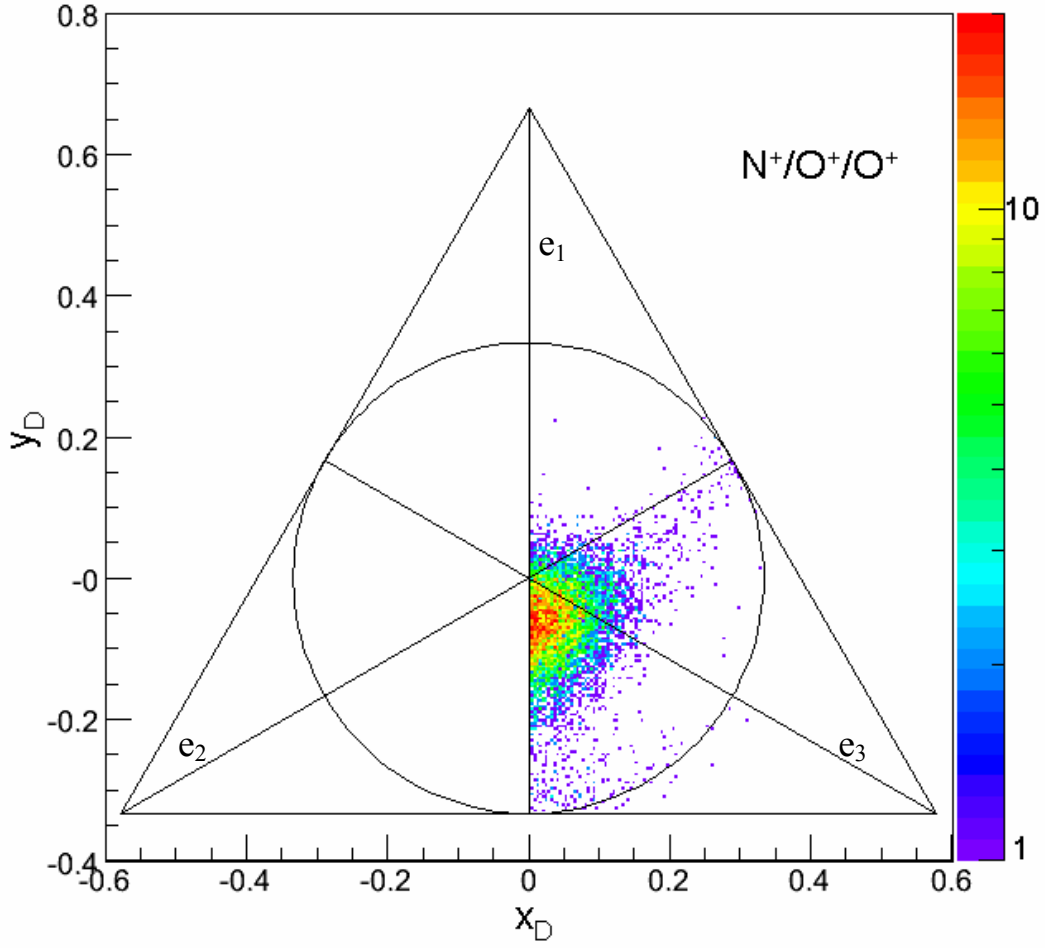

Figure IV- 19 Dalitz plot of triply ionized three-body dissociation N^+/ O^+/ O^+. The only the x_D positive plane is defined since the second fragment is the O^+ ion having more energy than the other.

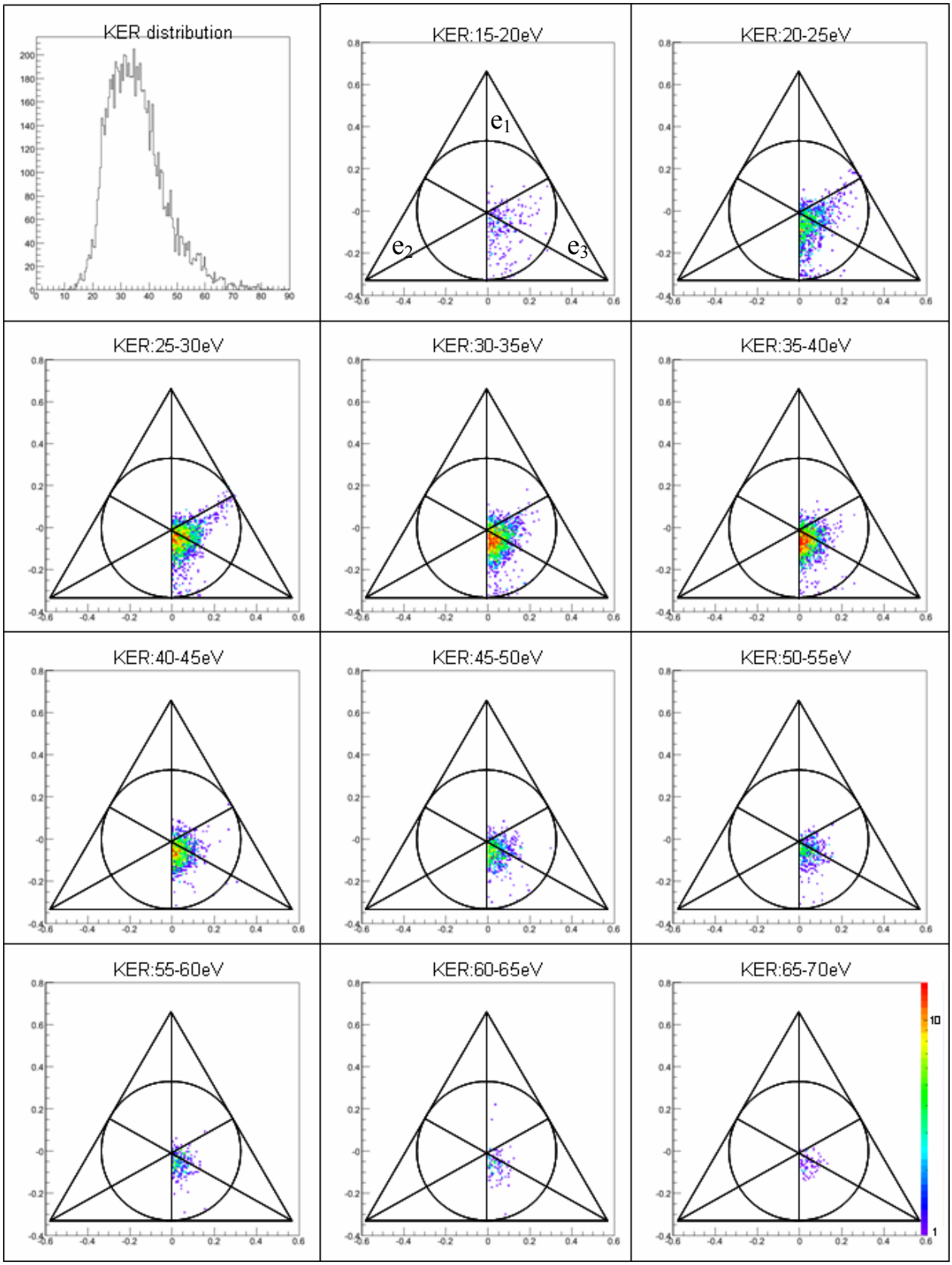

Figure IV- 20 Dalitz plots of ($N^+/O^+/O^+$) dissociation process for different values of KER. The KER distribution of this dissociation process is represented (black line) as well for guiding.

IV.5 $N^+/ O^+/ O$ dissociation channel

Identification of the fragmentation channel ($N^+/ O^+/ O$) is not as easy as other channels (without neutral fragment) because the neutral fragment is not detected by the MCP detector. What we can do for determining the characteristics of third fragment to study dissociation mechanisms of system is to use the momentum conservation which is a great advantage of fast ion impact experiment.

$$P_3(x,y,z) = -(P_1(x,y,z) + P_2(x,y,z))$$

One can then obtain momentum components of one neutral fragment by detecting two charged particles. In practice however, double coincidence measurement (N^+/O^+) does not equally correspond to the case of the dissociation channel ($N^+/ O^+/ O$). Due to the detector efficiency for MCP (≈50%), even when we detect N^+ and O^+ ion, the third fragment ion O^{q+} ($q \geq 1$) may not be detected. In the present experiment, we have to take into account the cases of ($N^+/ O^+/ O^+$) or ($N^+/ O^+/ O^{2+}$) as double coincidence events in which one of the fragment is missing. Note that the count rate of ($N^+/ O^+/ O^{3+}$) or other cases with higher charged fragment is negligibly small (see Figure IV-3). Moreover, the existence of fragments from N_2O_4 and residual N_2 and O_2 gas in the reaction chamber make it even more complicated. Actually it could be impossible to separate perfectly the ($N^+/ O^+/ O$) case from other events in the present configuration. The following section presents the identification method making maximum use of the detected events.

IV.5.1 Identification of the dissociation channel

As was described at IV.4-a, we start again from the coincidence map of N^+ and O^+ detection region. The main difference here is that the proper gate is generated with the condition of double-hit event only (figure IV-21(a)). In this region, possible combinations of detected first and second fragment are: (N^+/ O^+) as part of three fragments and (NO^{2+} / O^+) as triple-ionized two-body breakup channel[2] and also (N^+/ N^+), (O^+/ O^+) from residual gas in the reaction chamber. To be consistent with the ($N^+/ O^+/ O^+$) case, the events for which the 1st fragment is emitted in the backward direction are not taken into account. Then we calculate the sum of each momentum component of the two detected fragments with the mass of nitrogen for the first fragment and oxygen for the second. Here, fragments from residual gas which actually correspond to (N^+/ N^+) or (O^+/ O^+) show clear peaks far from zero, then one can eventually clean up events of (N^+/ N^+) and (O^+/ O^+) (See Appendix B for details). Figure IV-21(b) shows the obtained coincidence map after these tratments.

After filtering two-body breakup channels, the resulting data include still several dissociation channels such as $N^+ + O^+ + O$, $N^+ + O^+ + O^+$ and $N^+ + O^+ + O^{2+}$. The obtained spectra from (N^+/ O^+) double coincident measurement are thus a superposition of these three dissociation chan-

[2] It is highly unlikely that (N^+/O_2^{2+}) is produced from NO_2^{3+} two-body breakup due to its geometrical configuration.

nels. Even one can not separate one from the other in double coincidence measurement, the latter two cases can be also measured in triple coincidence and be identified perfectly. Thus by comparing spectra obtained from triple coincidence measurements to that of the double coincidence, the relative distribution for $(N^+/\ O^+/\ O)$ can be extracted.

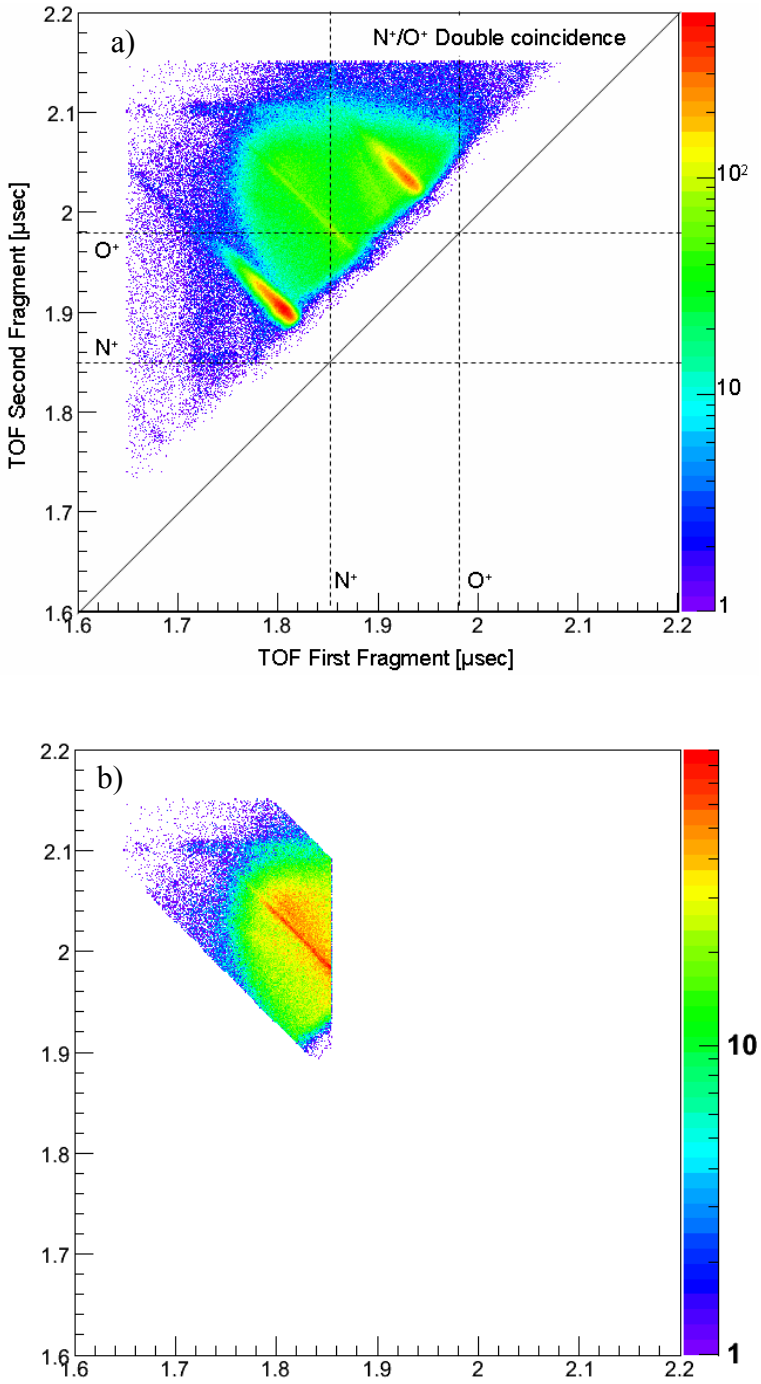

Figure IV- 21 Magnified coincidence map of the 1st and the 2nd fragments in the case of a) double coincidence and b) after filtering (see also Appendix A and B)

IV.5.2 Angular Distribution

Figure IV-22 shows the distribution of the angle between the two oxygen fragment momenta for double coincidence measurement. Note that the calculated angle does not directly correspond to the bond angle of the transient molecule in contrast to the case of the higher ionized states which can be better described by the Coulomb explosion model.

Three specific features are shown in the case of $NO_2^{2+} \rightarrow N^+ + O^+ + O$ (figure IV-22(a)): 1. main peak at 130 degree as for triply ionized NO_2 dissociation, 2. sub-peak at larger angle (140-180 degree) and 3. distribution at the small angle region. These distributions 2 and 3 are not observed in the case of CO_2^{2+} dissociation (figure IV-22(b) [ref.IV.13]). For understanding the angular distribution of doubly ionized dissociation, some studies have been reported by Osaka City University group by using photoionization for triatomic molecules (CO_2, OCS, SO_2). Although the authors found a partially successful explanation for linear molecules or for molecules with cylindrical symmetry, they concluded that the dynamical effects such as asymmetric bending or stretching motion of the molecules may provide a satisfactory model for understanding the observed behaviors [ref.IV.14,15,16]. In following sections, the dynamics of the NO_2^{2+} dissociation are discussed with its released kinetic energy and angular distribution.

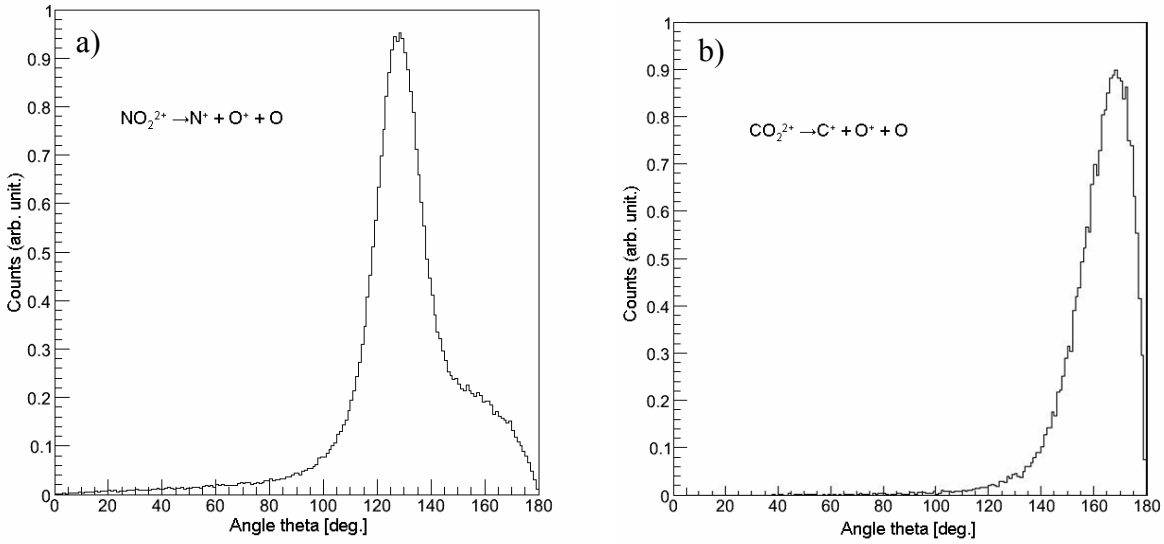

Figure IV- 22 Angular distribution of doubly ionized dissociation channel for the case of a)NO_2 collision with 4.7MeV/u Ne^{8+} and b) CO_2 collision with 8MeV/u Ni^{24+}.

IV.5.3 Kinetic Energy Release

We now start from KER spectrum since the released energy associated to each dissociation channel should show different distribution. KER spectra of (N^+/O^+) double coincidence, (N^+/ O^+/

O^+) and (N^+/ O^+/ O^{2+}) triple coincidence measurements are shown in figure IV-23. To emphasize the contribution of (N^+/ O^+/ O^+) and (N^+/ O^+/ O^{2+}) channels on double coincidence spectrum, peak heights of both spectra are adjusted to match the high KER tail of the distribution. What one can see here is that KER of doubly ionized dissociation channel $NO_2^{2+} \rightarrow N^+ + O^+ + O$ has a sharp peak around 9 eV then a broad distribution extending up to 40 eV. In this region figure IV-23 shows that one has to only take into account the contribution of (N^+/ O^+/ O^+). If we assumed that the high KER values are due to NO_2^{3+} and NO_2^{4+} fragmentation, the lower KER region (<20 eV) consists then only of doubly ionized dissociation forming (N^+/ O^+/ O).

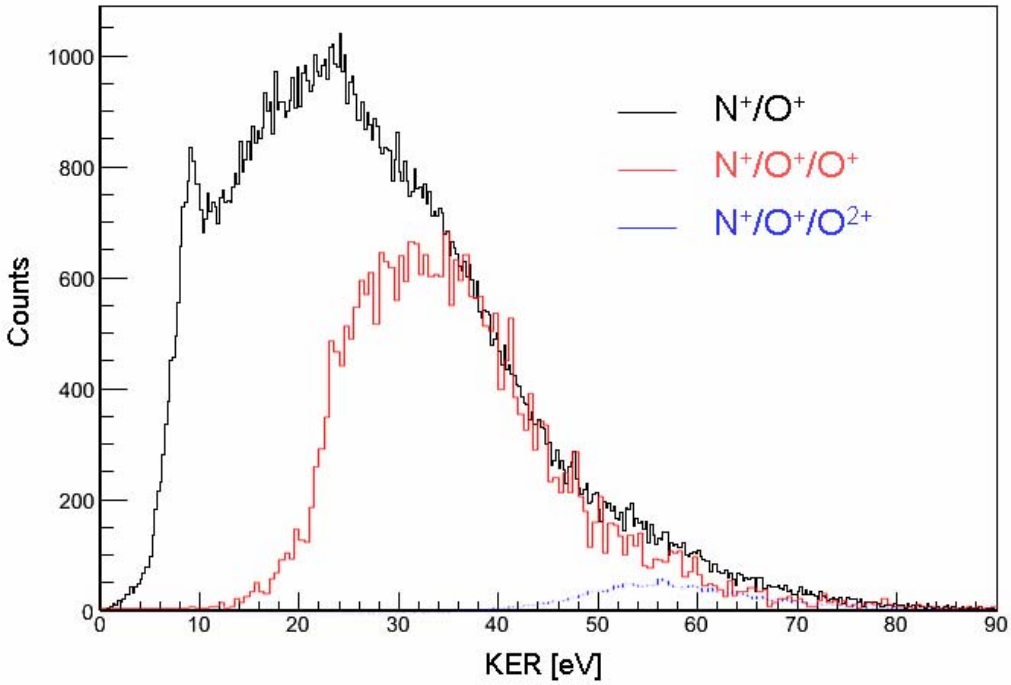

Figure IV- 23 Kinetic Energy Release distribution calculated by the double coincidence measurement (N^+/ O^+) (black) superposed with the KER of high ionized dissociation channels (N^+/ O^+/ O^+) (red) and (N^+/ O^+/ O^{2+}) (blue) measured by triple coincidence. The peak heights of both spectra are adjusted to match the high KER tail of the distribution.

IV.5.4 Newton diagram

By calculating momentum components of the third fragment from the detected two, the full Newton diagram can be reconstructed.

$$P_{1x} = P_1 \qquad P_{1y} = 0$$

$$P_{2x} = P_2 \cos\varphi_2 = m_2 \frac{\vec{v}_1 \cdot \vec{v}_2}{|\vec{v}_1|} \qquad P_{2y} = P_2 \sin\varphi_2 = \sqrt{P_2^{\,2} - P_{2x}^{\,2}}$$

$$P_{3x} = -(P_{1x} + P_{2x}) \qquad P_{3y} = -\sqrt{(P_3^{\,2} - P_{3x}^{\,2})}$$

As was discussed in previous paragraph, figure IV-24 shows superposed spectra of (N^+/ O^+/ O), (N^+/ O^+/ O^+) and few (N^+/ O^+/ O^{2+}) dissociation channels. One of the most remarkable feature in this diagram is a peaked distribution of the third fragment at "zero" momentum. Moreover, the third fragment may be emitted towards N^+ fragment as was observed in the case of $CO_2^{2+} \rightarrow C^+ + O^+ + O$ (figure I-4). Another difference from triple ionized dissociation channel at first glance is that N^+ fragment has lower and wider distributed momentum. On the other hand, the main peak shown at P_x(-100:0), P_y(±100:±200) for both second and third fragments may come mainly from $N^+/O^+/O^+$ dissociation channel (see figure IV-17).

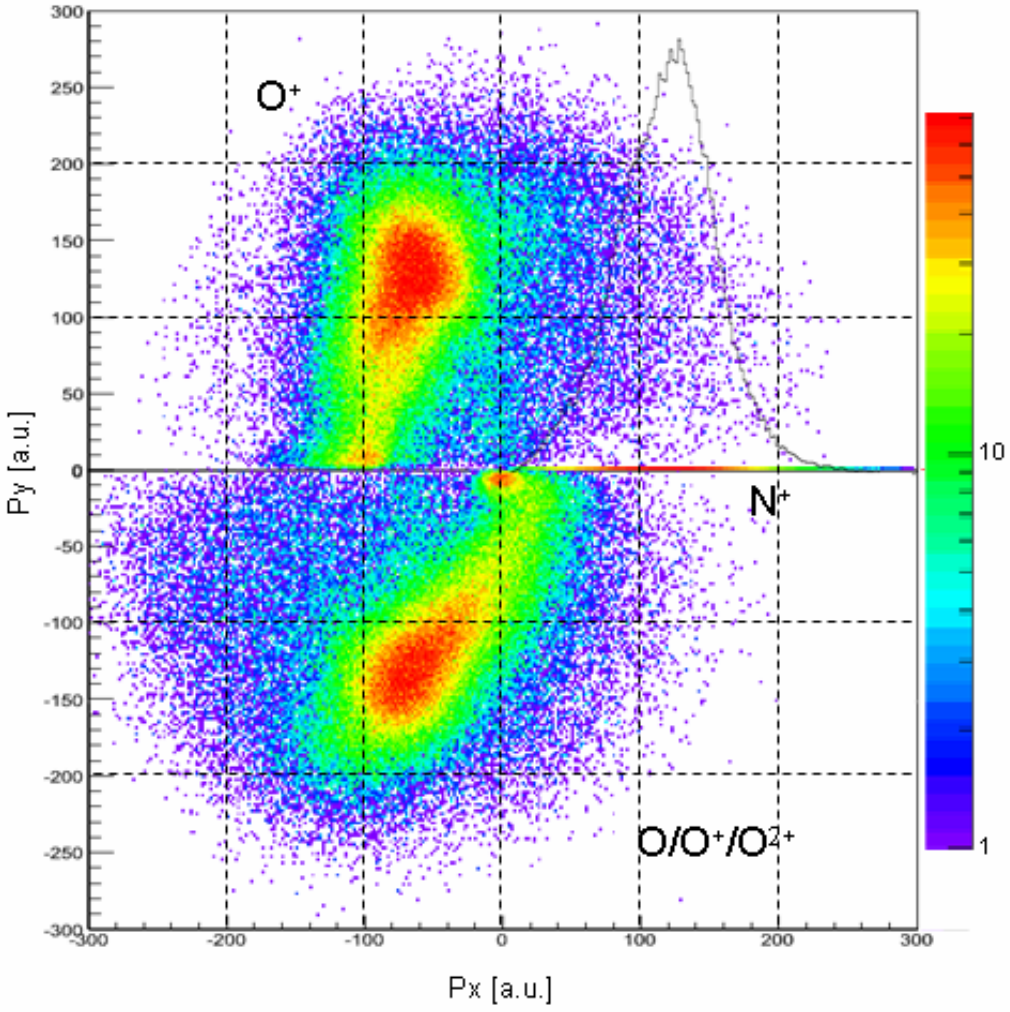

Figure IV- 24 Newton diagram of the filtered double coincident measurement (N^+/O^+).

The simplest and proper way to have a more detailed analysis is to represent the diagram as a function of KER (figure IV-24). One can see the evolution of momentum sharing among three fragments from a KER of 2.5 eV to 30 eV in 2.5 eV steps. The rough analysis of this evolution shows two different behaviors depending whether the KER is high or low. At high KER values (KER>25 eV), the Newton diagram reveals the same symmetric distribution as already observed for the ($N^+/O^+/O^+$) dissociation channel. At low energy region (KER≤20 eV) the resulting momentum sharing processes among fragments in the case of doubly ionized dissociation can be categorized by three distinct aspects as follows:

1. The neutral oxygen atom may be emitted towards nitrogen ion.
2. The neutral oxygen atom may be nearly at rest and momentum is shared between singly charged nitrogen and oxygen ions.
3. The charged and neutral oxygen fragments may have same momenta in which sum is compensated by the nitrogen ion.

The dissociation process 1 shows similar aspects to CO_2^{2+} dissociation into ($C^+/O^+/O$). By neglecting other features, one can see half-moon-shaped distribution in Newton diagram as was reported for CO_2^{2+} dissociation channel [ref.IV13, 17]. Considering that N^+ and O are emitted against the O^+ direction, the dissociation scenario resembles sequential fragmentation forming intermediate (NO^+/O^+) state. This reaction sequence is named "initial charge separation" [ref.IV.4]

The process 2 can be observed even in the high KER region. A possible interpretation of this dissociation channel is that the first bond breakage forms (NO^{2+} + O) then two singly charged fragments N^++O^+ repulse as Coulomb explosion. The zero momentum of the neutral oxygen atom indicates that first the NO^{2+}-O bond breaks very softly then N^+-O^+ reacts repulsively. This sequential fragmentation is named "deferred charge separation".

$$NO_2^{2+} \rightarrow NO^{2+} + O$$
$$\rightarrow N^+ + O^+ + O$$

The TOF coincidence map of this reaction channel shows a sharp diagonal line centered at (N^+/O^+) crossing point (figure IV-21). The reaction is clearly observed at a KER between 5.0-15eV. This energy region corresponds in fact the Coulomb repulsion energy of the second reaction which is calculated to be about 12eV with using a neutral bond length r_{NO}=1.197Å.

Another interesting distribution, the process 3 can be mainly seen at a KER of 10-15eV where charged O^+ ion and neutral O atom are emitted to same direction having small momentum in the perpendicular (P_y) direction. This shows also sequential fragmentation behavior with initial charge separation via an intermediate step (N^+/O_2^+). However, in contrast to the case1, none of the events corresponds to the intermediate (N^+/O_2^+) channel are observed. This means that the O_2^+ fragment lifetime has to bemuch shorter than the time spent in the extraction region (≈1nsec).

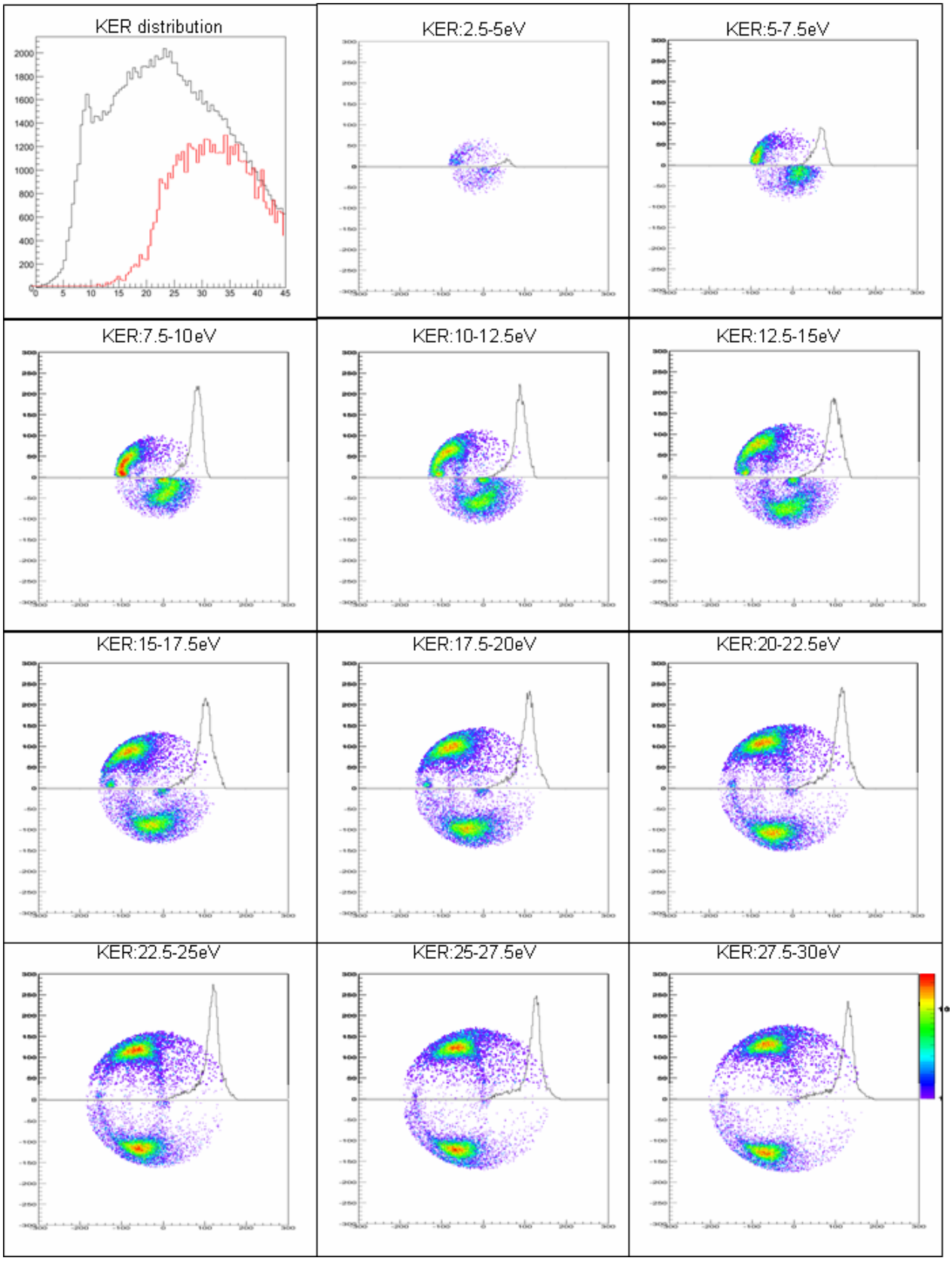

Figure IV- 25 Newton diagrams of double coincident measurement for different values of KER. The KER distribution of double coincident measurement is represented (black line) with the spectrum of ($N^+/O^+/O^+$) case for guiding.

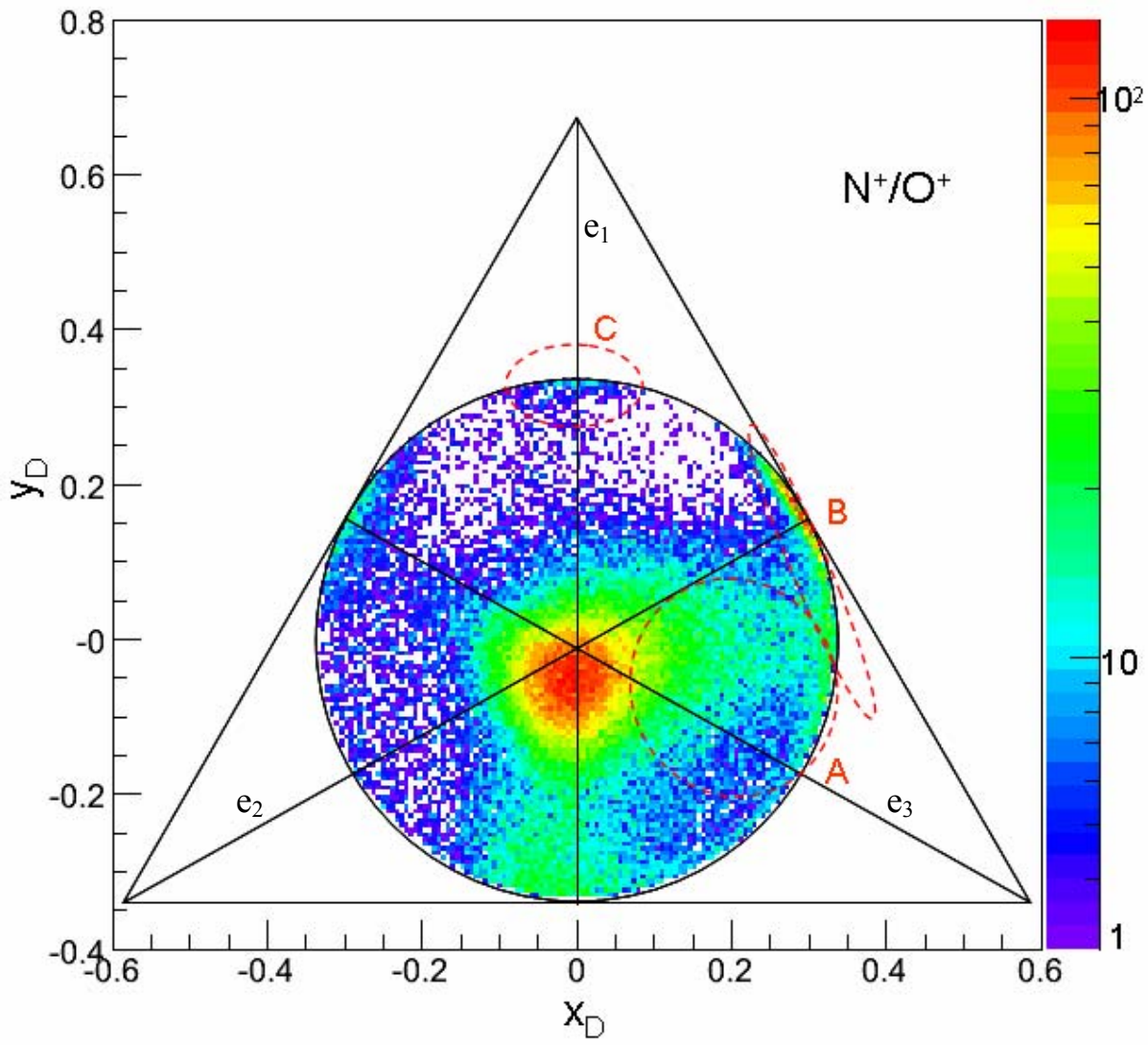

Figure IV- 26 Dalitz plot of filtered double coincidence measurement N^+/ O^+. Specific features are named A, B and C for comparing to the corresponding distributions on Newton diagram.

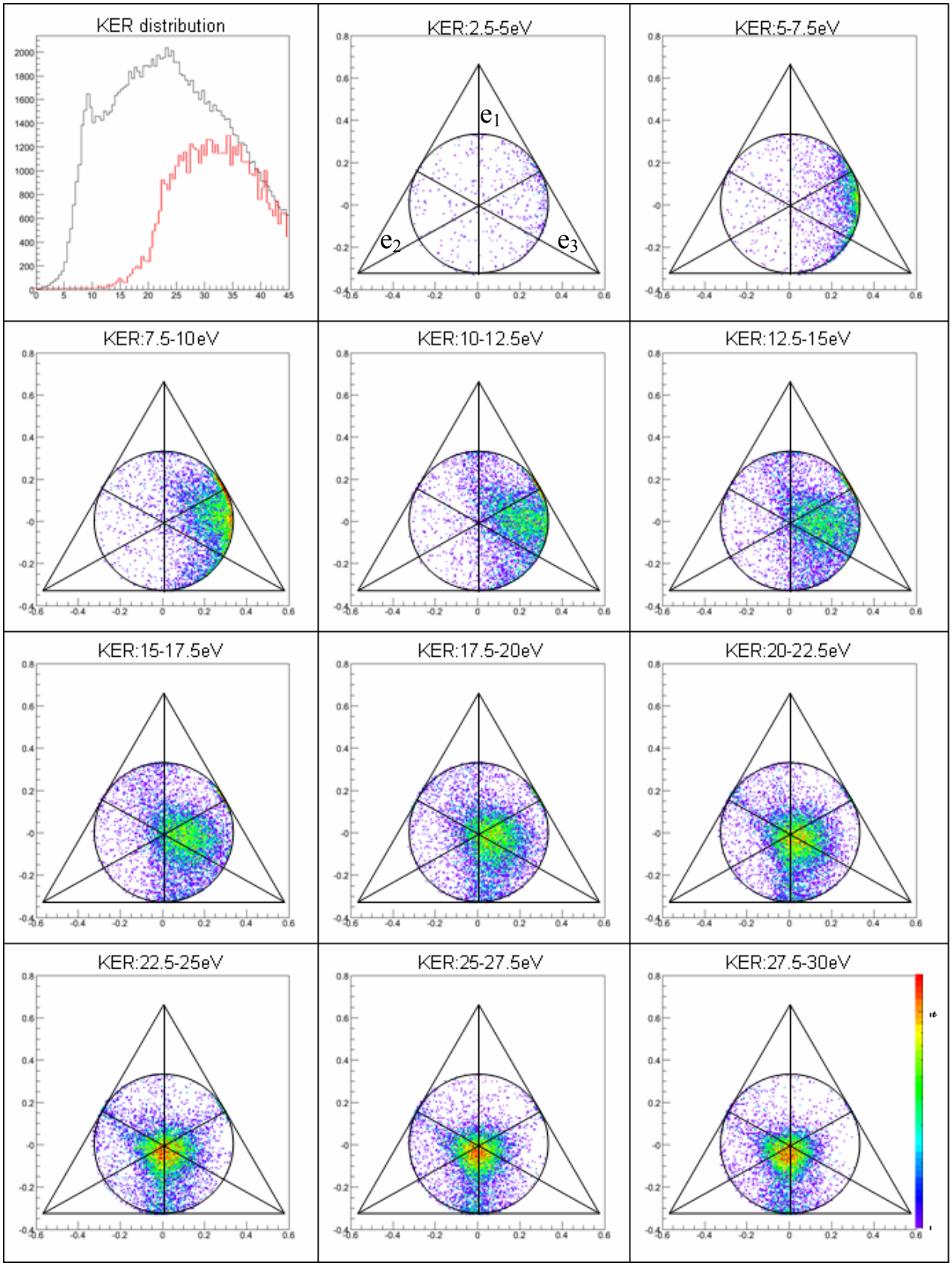

Figure IV- 27 Dalitz plots of double coincident measurement for different values of KER. The KER distribution of double coincident measurement is represented (black line) with the spectrum of ($N^+/O^+/O^+$) case (red line) for guiding.

IV.5.5 Dalitz Plot

The Dalitz plot gives another confirmation for these scenarios. Figure IV-26 shows combined Dalitz plot of (N^+/ O^+) double coincidence measurements corresponding to the Newton diagram presented in figure IV-24. The negative x_D half plane appears here since all three particles are separated. From section IV-4, one can attribute the main peak just below the center of the circle to ($N^+/O^+/O^+$) dissociation channel. The evolution of Dalitz plot as a function of KER (figure IV-26) shows that other peaked distributions marked with indices A, B, C correspond in fact the reaction processes 1-3, respectively. Only the dynamics for KER values below 20 eV will be discussed again since above this value the contribution of the channel ($N^+/O^+/O^+$) dominates.

The wider distribution at region A is observed at a KER up to 20 eV just before triply ionized dissociation comes into play. The corresponding configuration on the Dalitz plot shows asymmetric stretch of N^+-O and N^+-O^+ distances. Moreover, the released kinetic energy is found to depend on the angle between O^+ and NO^+. As the KER increases, the angle becomes more similar to the neutral NO_2 molecule bond angle.

The distribution in region B along to the edge of the circle indicates that the neutral oxygen has no momentum. The region B having a strong peak at a KER between 5-15 eV corresponds to the dissociation keeping neutral oxygen at rest.

The configuration of molecule following the Dalitz plot definition of region C is, the case for which both neutral and singly charged oxygen fragments have momenta in opposite direction with respect to the first fragment N^+ as if the dissociation forms (N^+/O_2^+). The corresponding KER, obtained from figure IV-27, is in the range 7.5-20 eV (mainly 10-15 eV) where O^+ and O emission in the same direction is observed in Newton diagram.

IV.6 Conclusion

By ion-induced "PIPICO" measurements, we have revealed some specific dynamics of multiply charged NO_2 dissociation. The case of NO_2^{3+} dissociation into ($N^+/O^+/O^+$) shows clear evidence of synchronous concerted fragmentation similarly to the case of the linear molecule $CO_2^{3+} \rightarrow C^+ + O^+ + O^+$. The geometry differences have significant, but straight forward effects on the dissociation dynamics: the central atom also has a momentum in the case of NO_2. The KER of the NO_2 shows mono-kinetic distribution peaked at 35 eV in the present energy resolution (≈250 meV).

On the other hand, the case of NO_2^{2+} dissociation shows several additional specific features. In the case of doubly charged two-body dissociation $NO_2^{2+} \rightarrow NO^+ + O^+$, the obtained KER values are in a good agreement with previous works [ref.IV.4,5], (figure IV-29). For the complete three-body breakup, it was not possible to separate perfectly the doubly ionized dissociation events from higher ionization degrees. However, it was found that the dissociation channels forming

($N^+/O^+/O$) is dominant as far as the KER stays below 20 eV (figure IV-27, 28). In this region, three different dissociation processes were observed:

$$NO_2^{2+} \rightarrow NO^+ + O^+ \rightarrow N^+ + O^+ + O$$
$$NO^{2+} + O$$
$$N^+ + O_2^+$$

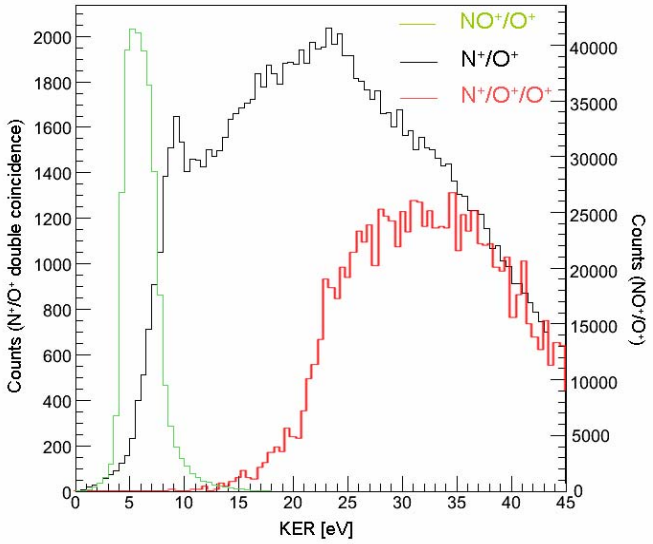

Figure IV- 28
KER distribution of double coincident measurement (black line) superposed with $NO_2^{2+} \rightarrow NO^+ + O^+$ (green line) and $NO_2^{3+} \rightarrow N^+ + O^+ + O^+$ (red line) dissociation channels. The peak height of the triply ionized dissociation spectrum is adjusted to match the high KER tail of the double coincidence KER distribution.

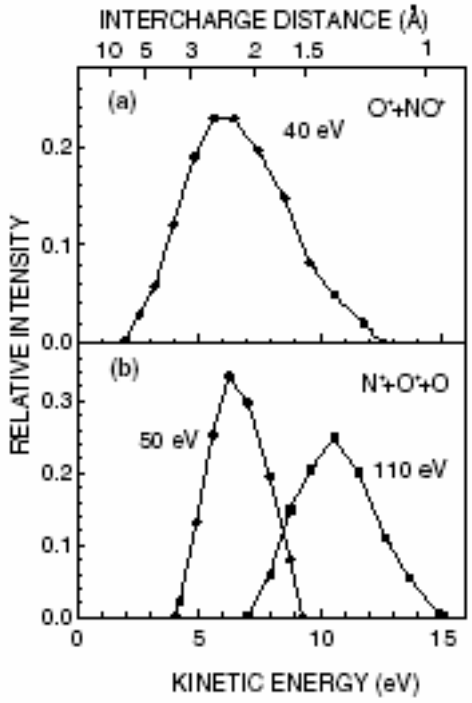

Figure IV- 29
KER distributions in the NO^+/O^+ channel at 40eV of photon energy (a) and in the N^+/O^+ channel at 50 and 110eV [IV.ref.5]

The sharp peak at 9 eV shown in KER distribution of double coincidence measurement (figure IV-28) corresponds to the differed charge separation dissociation channel forming NO^{2+} intermediate state and leaving an O atom at rest. This dissociation channel can be observed even when NO^+/O^+ partial dissociation channel exists. KER distribution in this region of doubly charged NO_2 fragmentation has also been reported by Masuoka and Kobayashi [ref.IV.5] in photoionization experiments. Note that their result for (NO^+/O^+) KER distribution agrees with our result (and also with reference [ref.IV.4]). However, they found that the KER distribution in the (N^+/O^+) channel depends on photon energy (figure IV-29). Their explanation is that this dependence is due to emitted electrons from different orbitals. In the case of fast ion collision, different impact parameters are involved leading to a broad range of energies transferred to the molecule. This would correspond to a broad band photo-ionization experiment.

Characteristic dynamics can be located on the Dalitz plot as shown in figure IV-30. The initial charge separation ($NO_2^{2+} \rightarrow NO^+ + O^+$) is located at point A. The differed charge separation ($NO_2^{2+} \rightarrow NO^{2+} + O$) is located at point B. These two processes may be associated to sequential fragmentation. Finally, the synchronous concerted process is located at the center of the circle (point C).

The general behavior observed is that all the dynamics is contained inside the triangle determined by these three points. Thus the conclusion of doubly ionized three-body dissociation is that the dynamics of this channel is a continuum of momentum sharing between the three fragments. This is obviously the signature of an asynchronous concerted fragmentation process.

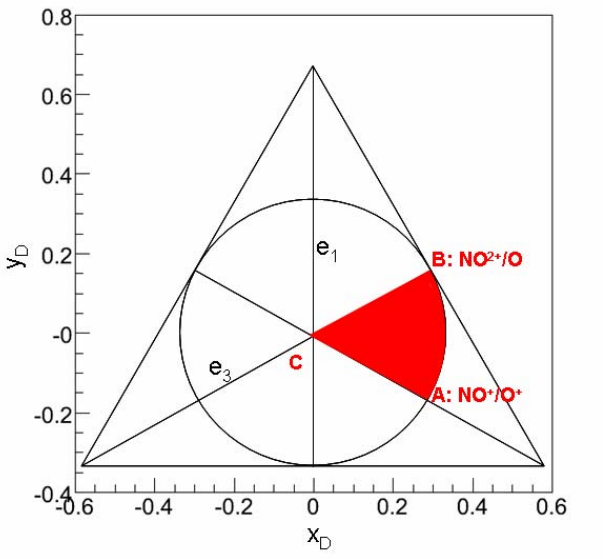

Figure IV- 30
Definition of Dalitz with the specific configuration for doubly ionized three-body dissociation process. For this dissociation channel, most of the observed events are distributed red triangle region.

§ V Water Dication Fragmentation

In this chapter, obtained results of the dication water molecule fragmentation are presented. One of the main interests of this work is to compare the dissociation mechanism of HDO^{2+} fragmentation induced by fast and slow heavy ion impact. Both $H^+ + OD^+$ and $D^+ + OH^+$ dissociation channels and also symmetric water molecule (D_2O, H_2O) break up channels are analyzed with calculation results.

V.1 Identification of dissociation channels

As the very first step of the analyses, the dissociation channels of interest are to be identified. The fragments Time Of Flight (TOF) measurement in Coincidence (PIPICO type spectrum) allows to separate and identify the various channels of dissociation. Figure V-1 shows such a spectrum, named coincidence map in the present work, for an HDO target with the final dissociation channels labeled. The proper gates to identify fragments are generated by calculating the flight time of fragments with no initial velocities. The crossing point of the calculated TOF for the first and the second fragments corresponds to the center of the TOF distribution of a certain channel. For symmetric dissociations, as $N_2^{2+} \rightarrow N^+ + N^+$ ions or any case of dissociation leading to identical mass fragments, some of events are hidden due to the dead time of the acquisition which is of the order 65nsec in this experiment. Because of the low extraction field, the coincidence spectra have such "banana shape" in contrast to the NO_2 experiment. It is easily seen that signals from residual gas components ($N^+ + N^+$ / $O^+ + O^+$ for example) were detected with a higher rate than that from the target gas. This is due to the poor density of the supersonic gas target. In order to reach sufficient statistics, a high projectile beam current was used. As a consequence, random coincidences start to show up on the spectra. Thanks to the efficient sorting algorithm, they are removed from the final results. In this experiment, more than 90% of the multi-hit events were double-hit events. Here we focus on doubly- charged two-body dissociation of water molecules (HDO, H_2O, D_2O).

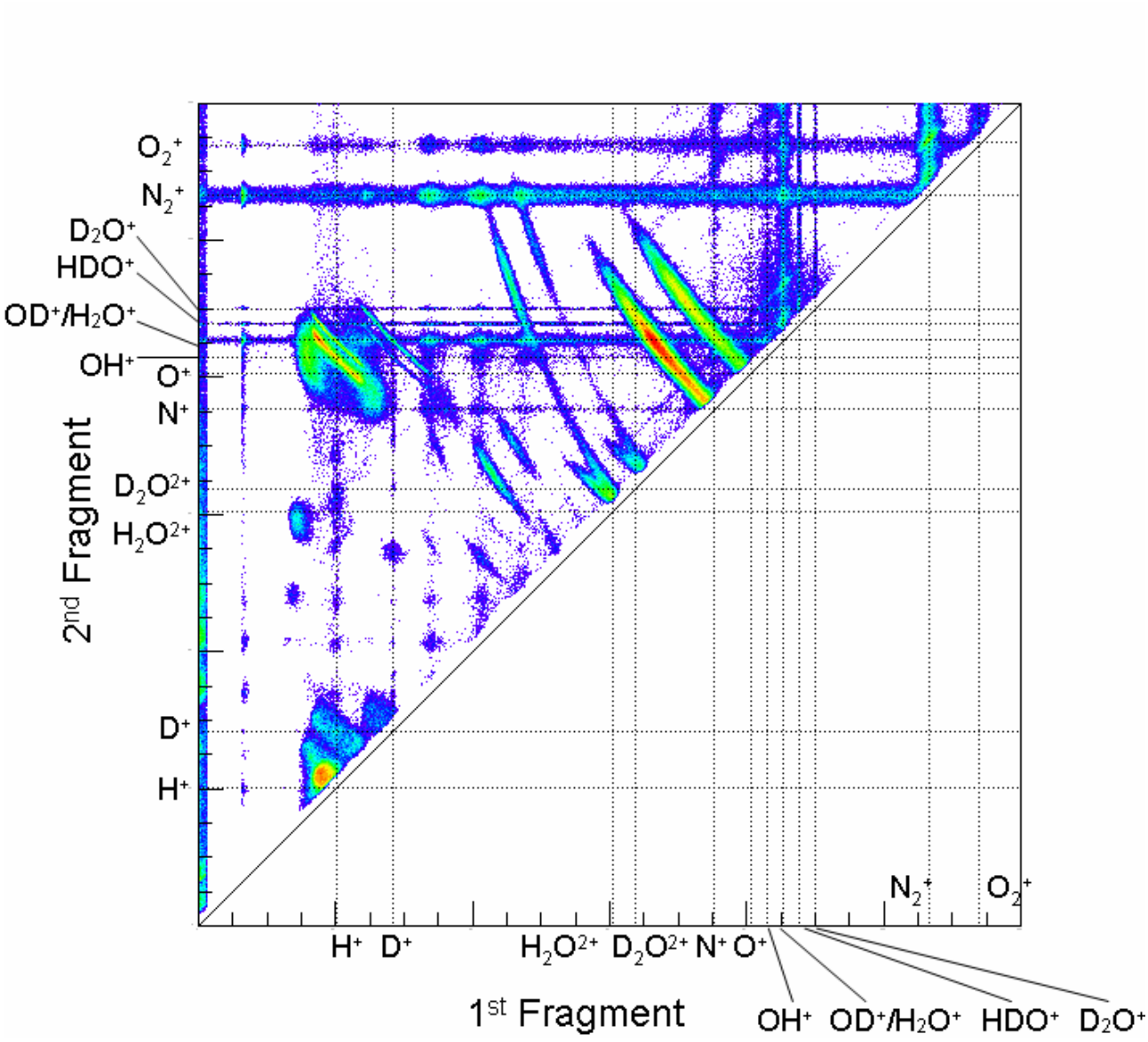

Figure V- 1 Identification of dissociation channels by coincidence Map of 1st and 2nd fragment.

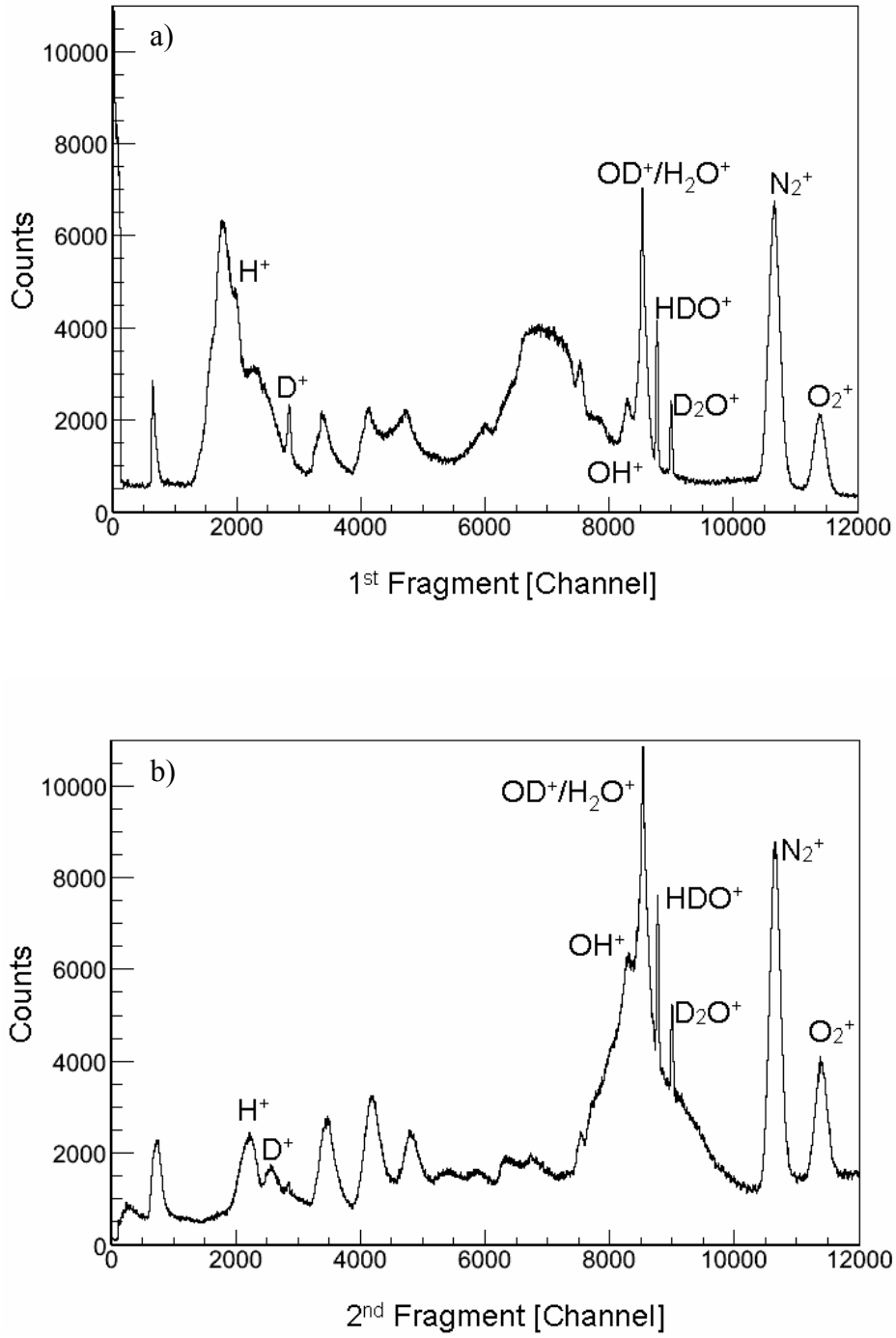

Figure V- 2 1D time of flight spectrum of the 1st fragment a) and the 2nd fragment b) when more than two fragments are detected.

V.2 Fragmentation of dication water molecules

As was described in III-3.2, the four dissociation channels of dication water molecules can be clearly separated by the collision point filtering. The coincidence map shown below results from the superposition of four dissociation channels after cleaning up by the z_0, y_0 and L_0 filters. Four Reaction channels of dication water molecules are as follows:

$$HDO^{2+} \rightarrow H^+ + OD^+$$
$$HDO^{2+} \rightarrow D^+ + OH^+$$
$$H_2O^{2+} \rightarrow H^+ + OH^+$$
$$D_2O^{2+} \rightarrow D^+ + OD^+$$

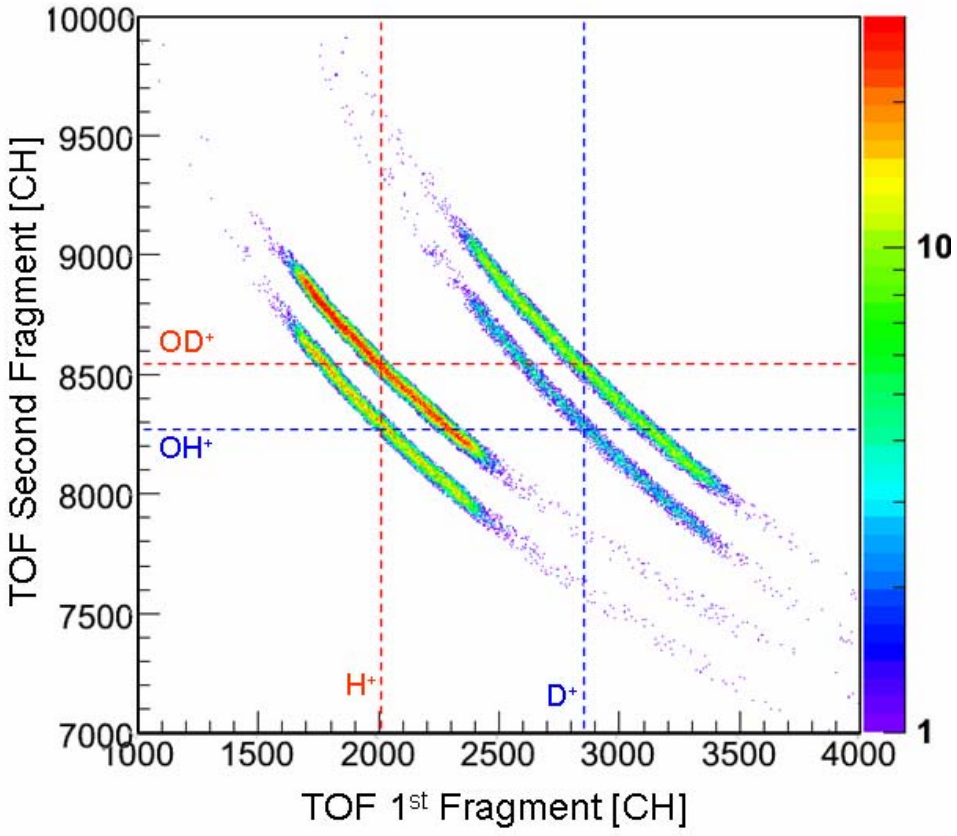

Figure V- 3 Superposition of four dissociation channels of interest after 3D position filtering

The distribution extensions of both dissociation channels which generate the H^+ ion fragment are shorter than that of the channels with D^+ fragment. This distribution corresponds to the difference of TOF of the first and the second fragment (TOF1 and TOF2). This indicates that O-D bond breaking channels lead to a wider momentum distribution than the O-H bond breaking channels. More detailed momentum analyses done by the equation (3. 26) are shown in figures V-4 – V-7 as two-dimensional momentum diagrams and total momentum distribution in the center-of-mass frame. All momentum "spheres" for the four dissociation channels look perfectly round, which agrees with an isotopic breakup. On the other hand, the width of the "banana" contains the initial momentum distribution. The sharp distribution of this direction here proves that the momentum transfer from projectile into the target molecule is negligibly small.

V.3 Branching ratios and Kinetic Energy Release

HDO^{2+} deuterated water dication fragmentation has been given special attention in recent experiments [ref. V.1-4]. The strong isotopic preference has been observed in favor of the cleavage of OH bond over OD bond in HDO^{2+}. Two values of the branching ratio $(H^+ + OD^+) / (D^+ + OH^+)$ have been measured by different experimental method and disagree by 25% ([ref. V.1]: 6.5 ± 0.5, [ref. V.2]: 5.2 ± 0.3). In the present experiment, we have obtained an intermediate value. Using imaging techniques and an improved spectrometer, specially designed for this experiment, also makes it possible to have an access to high resolution KER distributions for each of these two channels. Moreover, in order to be as complete as possible, H_2O^{2+} and D_2O^{2+} dissociation were analyzed in the same way as HDO^{2+} giving a direct calibration of relative cross sections.

Total number of counts and branching ratios for 13.7MeV/u S^{15+} ion impact experiment are shown in table V-1. The uncertainty comes from filter settings. When setting simple filters that limits the initial position z_0, y_0 and L_0, one must verify that the filters do not cut the true events for all four dissociation cases. The O-H bond is then found to be 5.7 times more preferable to be broken than the O-D bond. The ratio of the channel $(H^+ + OH^+)$ over $(D^+ + OD^+)$ is as expected from the equal mixing of liquid H_2O and D_2O in the oven. This gives confidence in the filtering procedure which has to remove the contribution of the residual water vapor. Thus, the ratio of the parent molecule represents well the initial gas target composition i.e. HDO: H_2O: D_2O = 2:1:1.

Dissociation Channel	Total Counts	Ratio to $(D^+ + OH^+)$
$H^+ + OD^+$	29984	5.7 ± 0.1
$D^+ + OH^+$	5294	1
$H^+ + OH^+$	16830	3.2 ± 0.1
$D^+ + OD^+$	17222	3.3 ± 0.1

Table V- 1 Obtained total counts of four dissociation channels and branching ratios

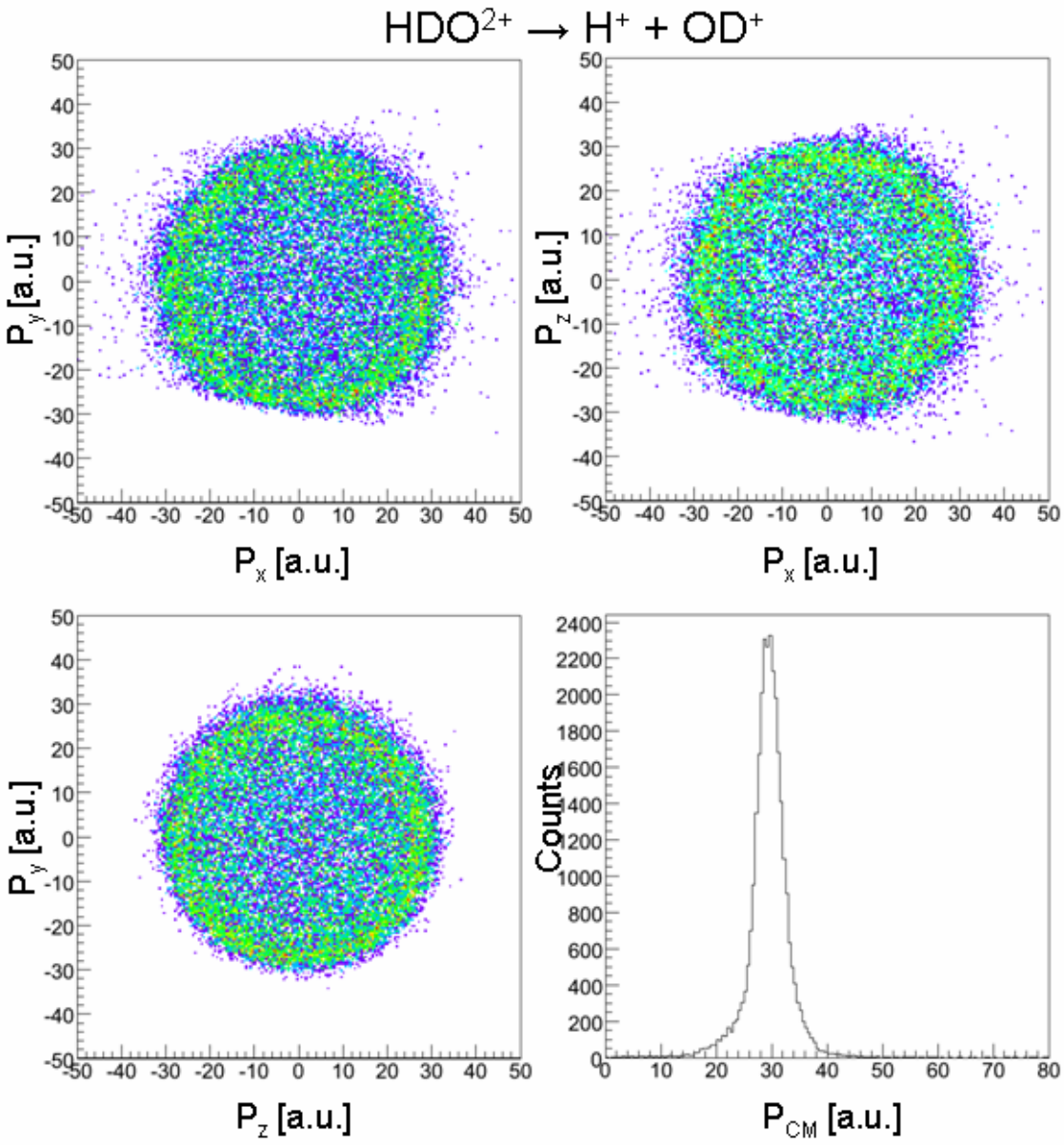

Figure V- 4 Fragmentation momentum in the center-of-mass frame of $HDO^{2+} \rightarrow H^+ + OD^+$ dissociation channel.

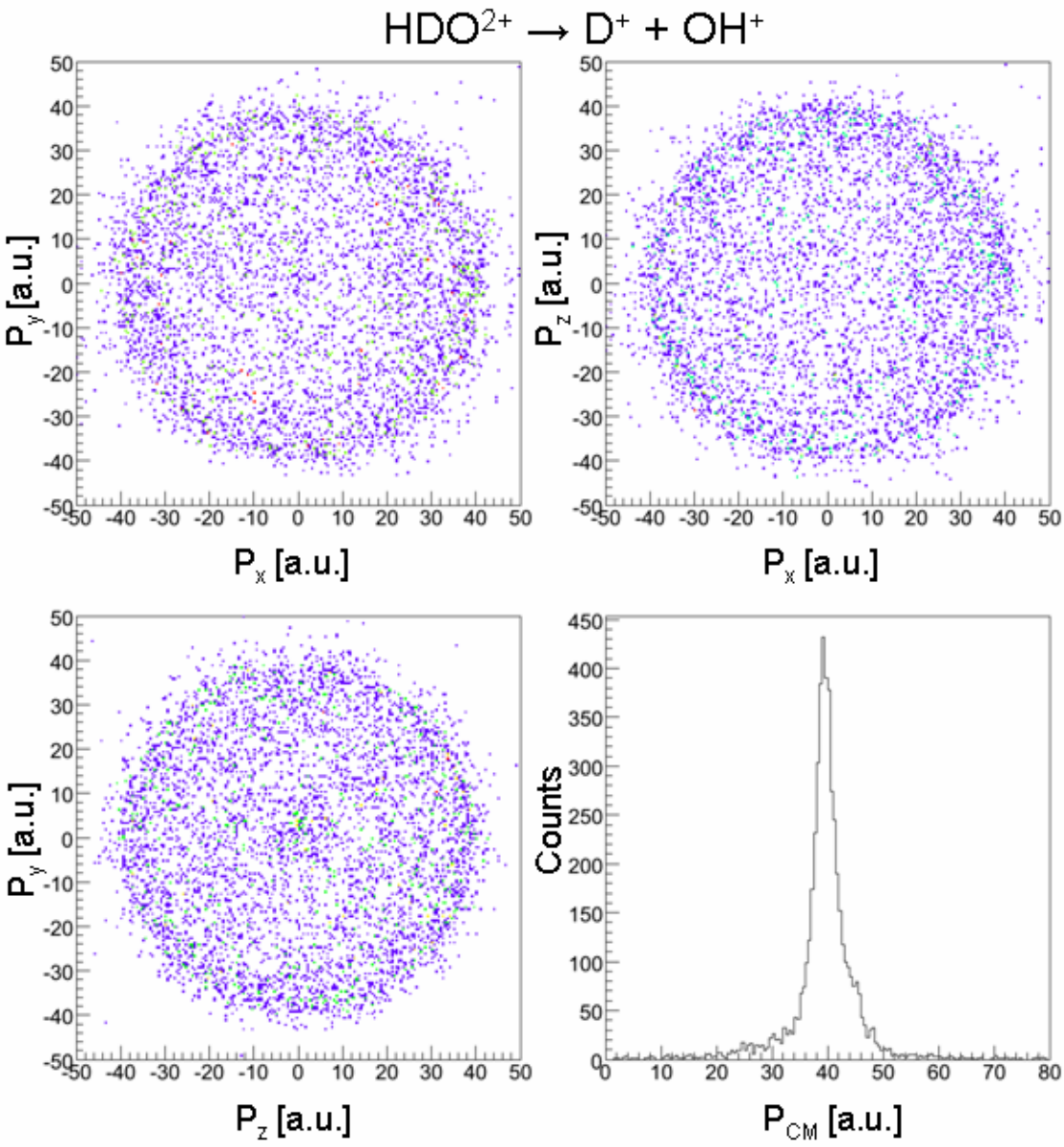

Figure V- 5 Fragmentation momentum in the center-of-mass frame of $HDO^{2+} \rightarrow D^{+} + OH^{+}$ dissociation channel.

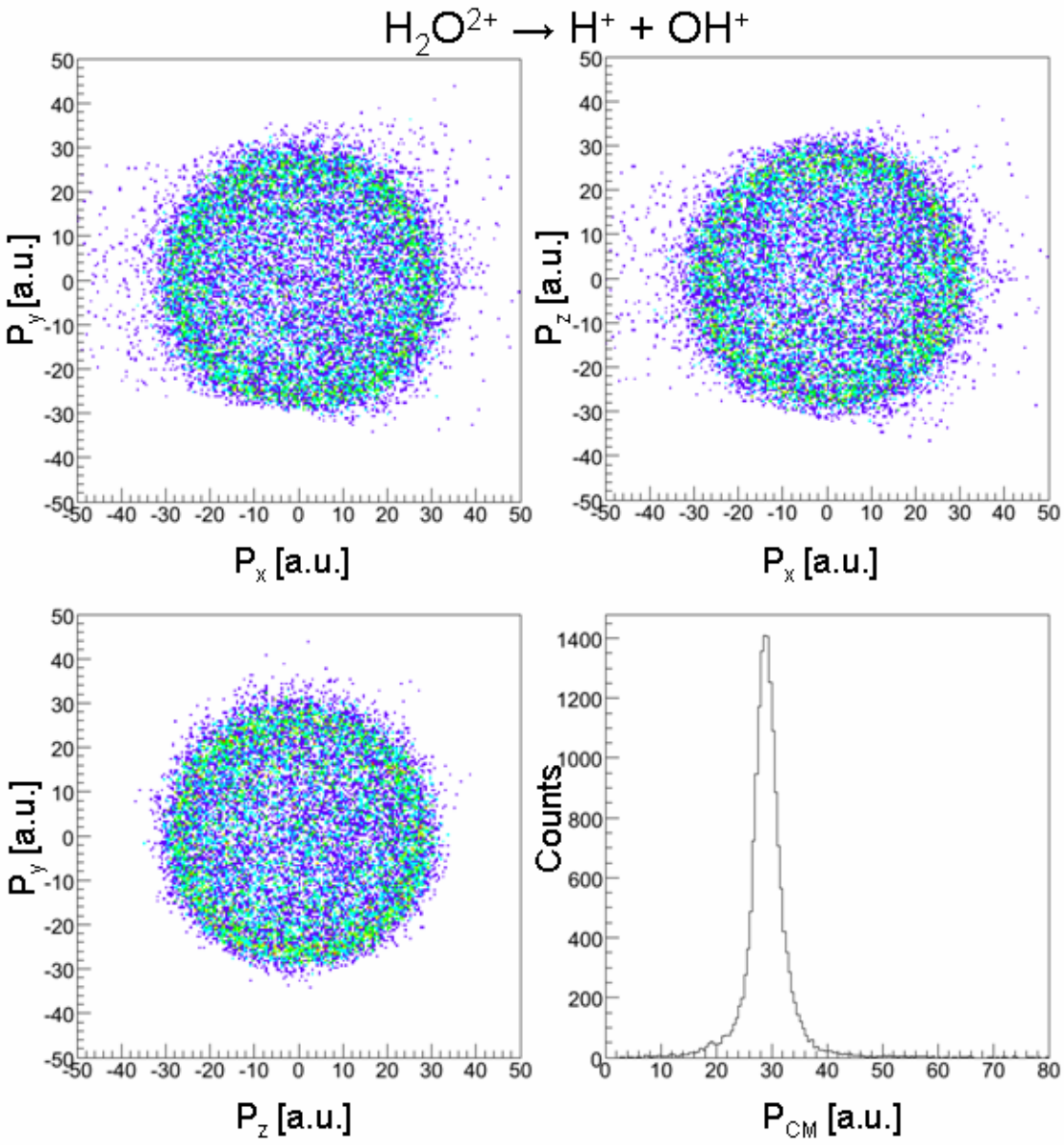

Figure V- 6 Fragmentation momentum in the center-of-mass frame of $H_2O^{2+} \rightarrow H^+ + OH^+$ dissociation channel.

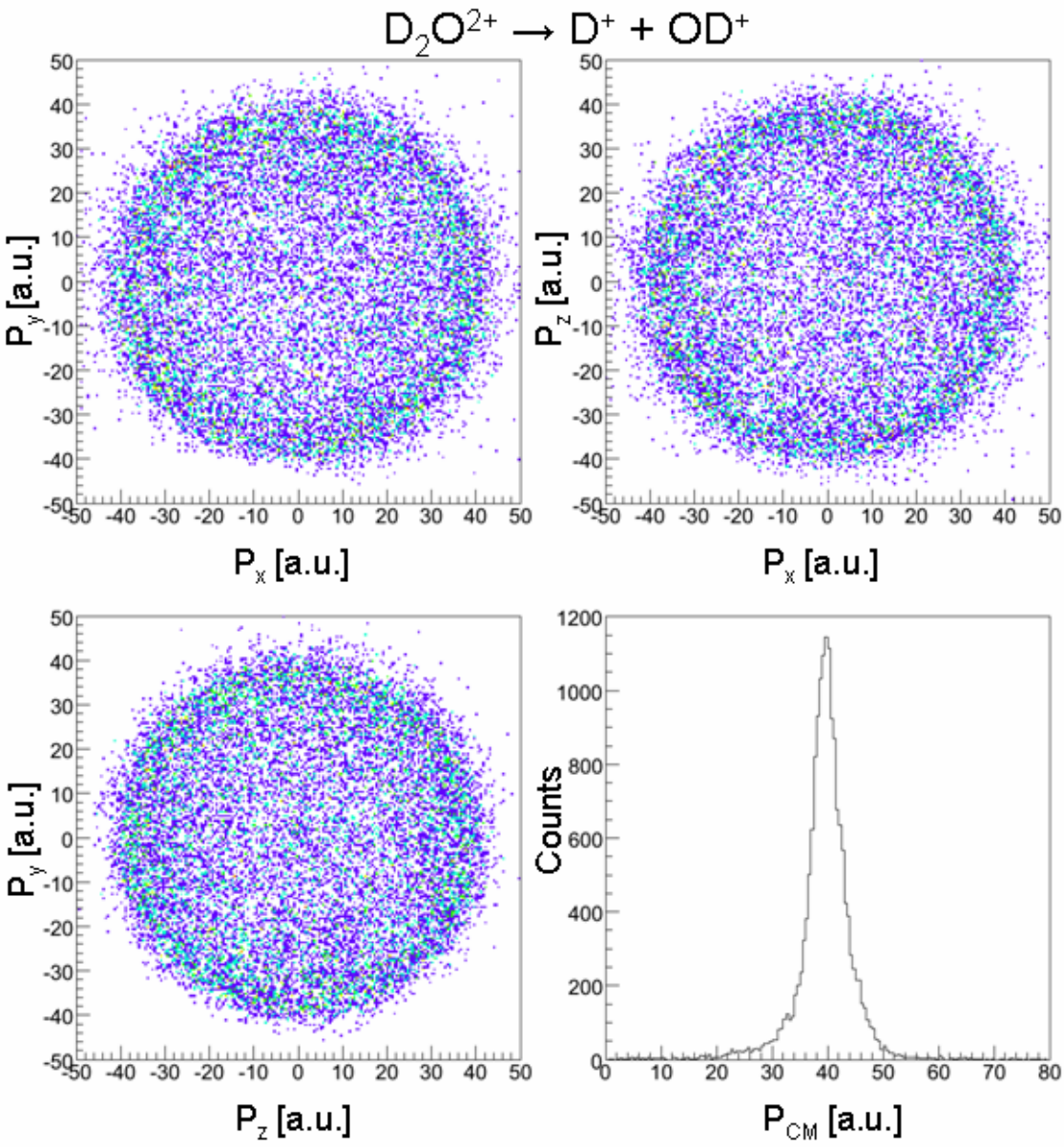

Figure V- 7 Fragmentation momentum in the center-of-mass frame of $D_2O^{2+} \rightarrow D^+ + OD^+$ dissociation channel.

Another surprising aspect about HDO^{2+} two-body fragmentation is a difference of mean KER values between two dissociation channels. The kinetic energy released by a fragmentation is calculated from the momentum of one fragment in the center-of-mass frame P_{CM} as:

$$KER = \frac{1}{2} P_{CM}^{\ 2} \cdot \frac{m_1 + m_2}{m_1 \cdot m_2}$$

Previous work [ref. V.1] reported that the $D^+ + OH^+$ and $H^+ + OD^+$ KER distributions are centered at 6eV and 7eV, respectively (resolution: 0.5eV). In the present experiment, we could improve the precision on these values for all four water dication dissociation channels. The KER values are 6.5±0.1eV for $D^+ + OH^+$, $H^+ + OH^+$ and $D^+ + OD^+$ which is in accordance with the result published by Siegmann *et al* [ref. V.5] for the $H^+ + OH^+$ channel, and 6.9±0.1eV for $H^+ + OD^+$(figure V-8). Intuitively, it was believed that the preferred dissociation channel for HDO would take similar KER distribution as for symmetric molecules H_2O and D_2O. However, the final results of the detailed analysis show that the $H^+ + OD^+$ dissociation channel gives rise to a wider KER distribution than other three channels towards higher KER region. To make it more visible, it is instructive to compare each pair of KER distributions separately. Figure V-9 shows the KER spectra, normalized to the same peak height, for two dissociation channels of HDO^{2+}. The low KER edges of two spectra agree well but the distribution of the $H^+ + OD^+$ channel is about 1.3 times wider than that for $D^+ + OH^+$. From the looks of the same sort of spectra for symmetric molecules (figure V-10), this can not be explained by the momentum difference between O-H and O-D bond braking. The KER spectra of symmetric molecule dissociations $H^+ + OH^+$, $D^+ + OD^+$ overlap each other perfectly (without normalization). The normalized spectra of both $H^+ + OD^+$ and $D^+ + OD^+$, $D^+ + OH^+$ and $D^+ + OD^+$ show also slight differences. This series of spectra reveals that the difference in the mean KER values does not have root in shifting but in broadening of $H^+ + OD^+$ dissociation channel distribution to the higher KER region.

V.4 Comparison with Theoretical Calculations[1]

To go further in the dissociation mechanisms, simulating the dynamics of the fragments on Potential Energy Surfaces (PES) is required. For the simulation, the momenta and positions of the three atoms are generated from the Wigner distribution deduced from the harmonic approximation of a precise PES of H_2O ground state [ref. V.6, 7]. This PES has a saddle point as presented in figure V-11, which separates the dissociation path into two and three body. Assuming a Frank-Condon transition, the system is then propagated classically on the X^3B_g ground state surface of the dication in a wide range of bending angles [ref. V.8]. We make sure to propagate for a sufficiently long time, so

[1] This simulation results have been obtained by people from "Simulation of the Excited Matter" group in CIRIL (B. Gervais, E. Giglio and a collaborator M.E. Galassi from Universidad Nacional de Rosario, Argentina.)

that dissociation is completed, and the remaining Coulomb repulsion energy between the charged fragments becomes negligibly small with respect to the kinetic energy of the system. We simulated 10^6 trajectories to achieve good statistics. We checked sensitivity to initial conditions by scaling the PES so that the vibrational frequencies match closely the experimental frequency measurements. The simulated branching ratio then changes from 7.5 in the pure harmonic approximation to 7.2 when matching experimental frequencies. The difference with our previous simulated ratio (13.5) arises mainly from a too short time and thus the propagation was incomplete. Thus, the calculation reproduces well a preferential cleavage of the O-H bond as experimentally observed. The branching ratio is found to be about 1.3 times higher than the experimental value. Obviously, the ratio depends strongly on the PES. As described above, the simulation only takes into account the ground-state population. Furthermore, theoretically the target supersonic jet temperature ensures that only the lowest vibrational mode should be populated. Then the difference between experiment and calculation may come from the population not only in the ground state but also in electronic excited states of the dication. This will be discussed later again with low-energy experiment results.

The simulated KER distributions for HDO, H_2O and D_2O dication two-body fragmentation are shown in FigureV-12 - V-13. For each dissociation channels, mean KER values similar to experimental results are obtained: 6.5eV, 7.3eV and 6.8eV for $D^+ + OH^+$, $H^+ + OD^+$ and both $H^+ + OH^+$ and $D^+ + OD^+$, respectively. Although slight difference appears in the distribution shape and the KER value of $H^+ + OD^+$ channel, it is remarkable that mean KER separation between the two dissociation channels of HDO^{2+} is well reproduced. Differences in the KER distribution width and position between theoretical and experimental results (figureV-10-13) have no conclusive interpretation for the moment.

	Experiment 13.5MeV/u S^{15+}		Experiment 170keV Ne^{10+}		Calculation	
	KER [eV]	FWHM	KER [eV]	FWHM	KER [eV]	FWHM
$H^+ + OD^+$	6.9	2.4	6.7	2.0	7.3	2.6
$D^+ + OH^+$	6.5	1.9	6.3	1.5	6.5	2.8
$H^+ + OH^+$	6.5	2.2	6.3	1.8	6.8	3.0
$D^+ + OD^+$	6.5	2.2	6.3	1.8	6.8	3.0

Table V- 2 Comparison of Kinetic Energy Releases from four dissociation channels induced by different ionization processes and theoretical calculation.

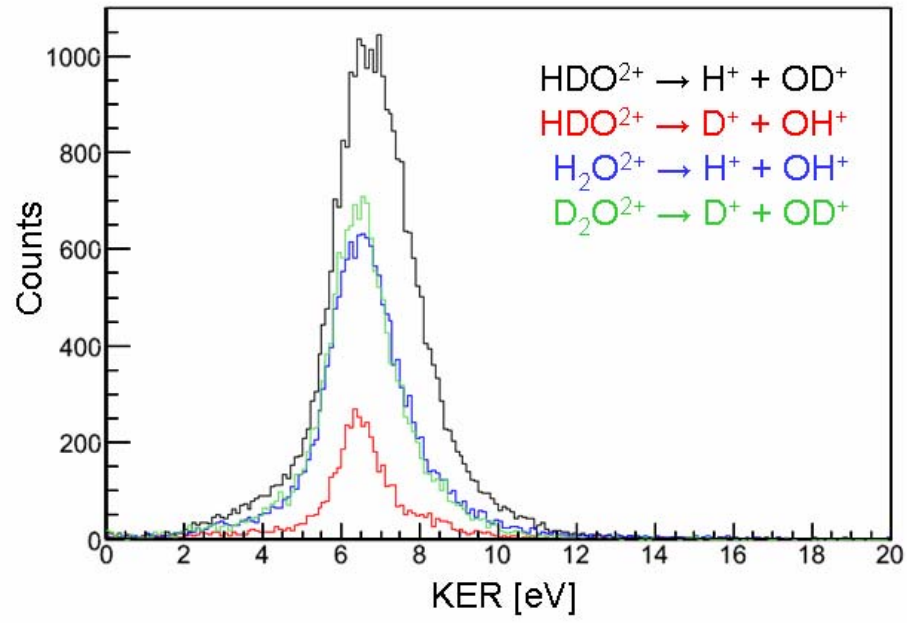

Figure V- 8 KER distributions of four dication two-body dissociation channels induced by 13.7MeV/u S^{15+}, without normalization.

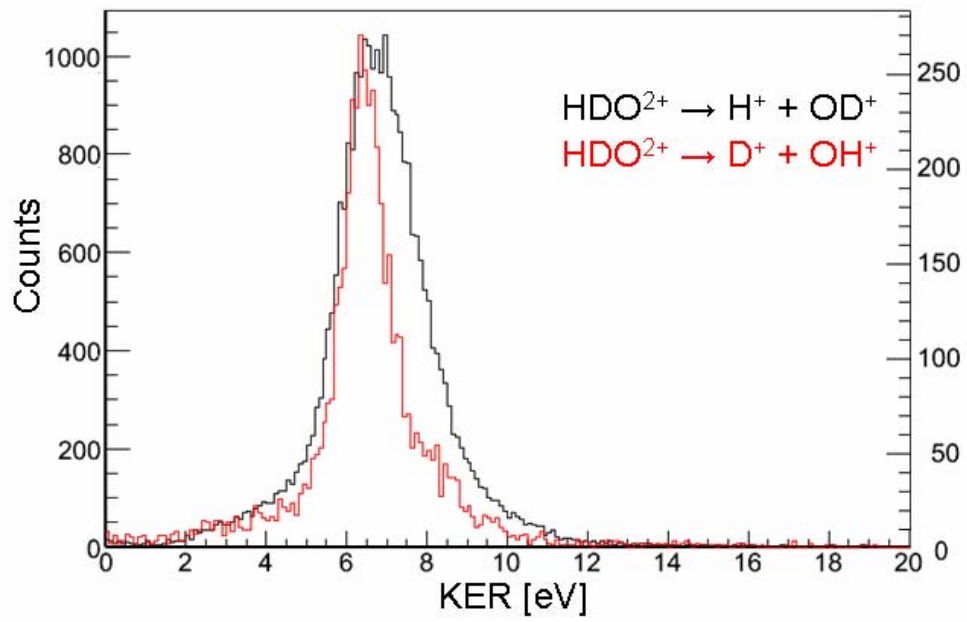

Figure V- 9 KER distributions of $HDO^{2+} \rightarrow D^+ + OH^+$ (red) , $H^+ + OD^+$ (black) dissociation channels induced by 13.7MeV/u S^{15+}, normalized by peak height.

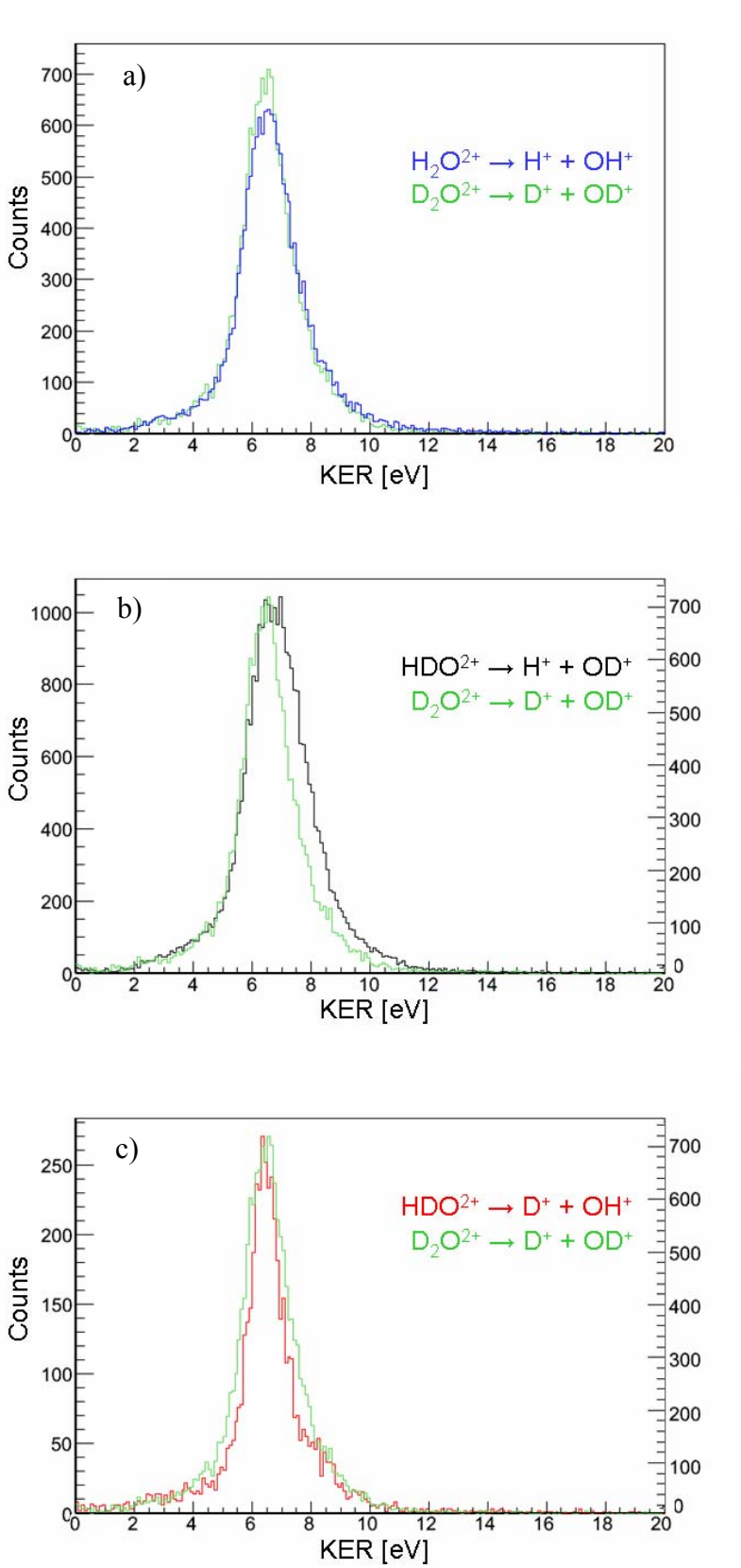

Figure V- 10 Comparison of each pair KER distributions among four dissociation channels: $H^+ + OD^+$ (black) , $D^+ + OH^+$ (red), $H^+ + OH^+$ (blue) , $D^+ + OD^+$ (green) induced by 13.7MeV/u S^{15+}.
a): without normalization, b) and c): normalized by peak height.

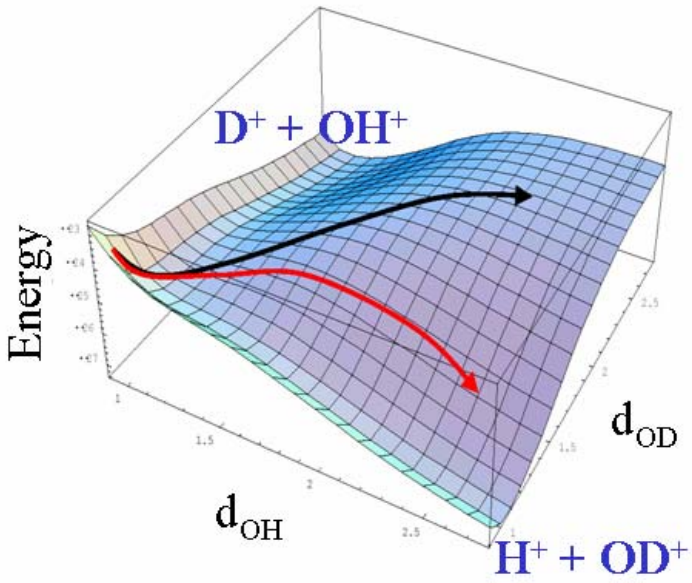

Figure V- 11 Ground state HDO^{2+} Potential Energy Surface. Arrows indicate dissociation pathways of three-body fragmentation (black) and H+/OD+ two-body fragmentation (red).

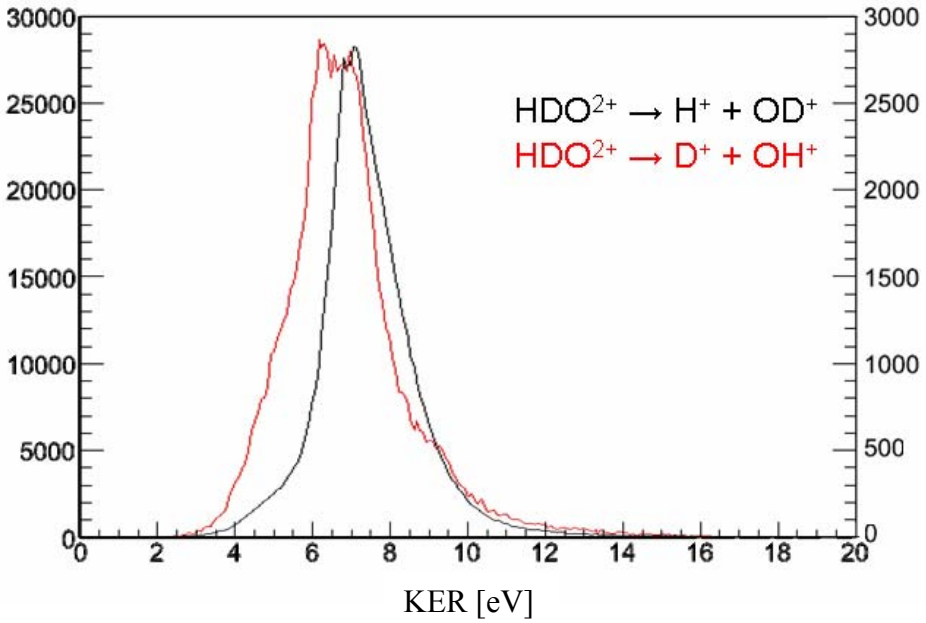

Figure V- 12 Calculated KER distributions of $HDO^{2+} \rightarrow D^+ + OH^+$ (red) , $H^+ + OD^+$ (black) dissociation channels, normalized by peak height.

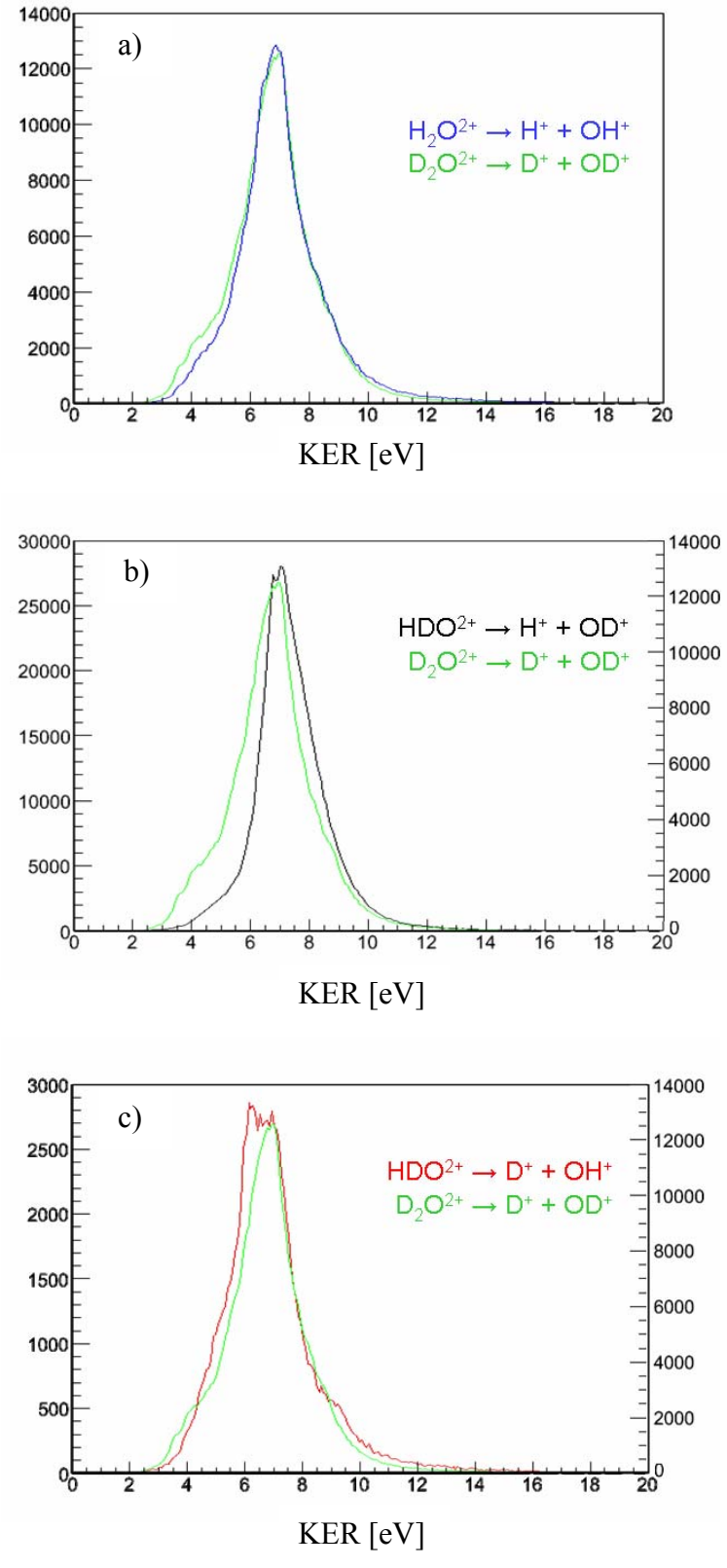

Figure V- 13 Comparison of each pair KER distributions among four dissociation channels: $H^+ + OD^+$ (black) , $D^+ + OH^+$ (red), $H^+ + OH^+$ (blue) , $D^+ + OD^+$ (green) induced by 13.7MeVu S^{15+}.
a): without normalization, b) and c): normalized by peak height.

V.5 Comparison with Low Energy Projectile Experiment

After the high energy projectile experiment and the new calculation, one hypothesis that was proposed to explains the quantitative difference: dication excited states may be populated by collision with fast highly charged ions and may play a role in the fragmentation scheme. One way to test this hypothesis is to observe the same dissociation dynamics induced by different interaction process. HDO^{2+} dication may be produced by the ionization process: the two missing electrons are ejected to the continuum. That's the case in high energy regime collisions. Another possibility to doubly ionize the molecule is to take advantage of the electron capture process: the electrons are captured by the colliding projectile. This process is known to occur at low collision energy. Valence electrons are mainly concerned thus the target molecular ion seldom left in an electric excited state.

To perform this experiment, 170keV Ne^{10+} projectile ion has been chosen. The reactions leading to an HDO^{2+} product are the following:

$$HDO + Ne^{10+} \rightarrow HDO^{2+} + Ne^{9+} + e^{-} \quad \text{(a)}$$

$$\rightarrow HDO^{2+} + Ne^{8+} \quad \text{(b)}$$

The auto-ionizing double electron capture channel (a) represents 79% of the dication two-body dissociation while the true double electron capture process contribution (b) 19%. In termes of the momentum sharing among the target molecule, any difference between processes (a) and (b) were not observed.

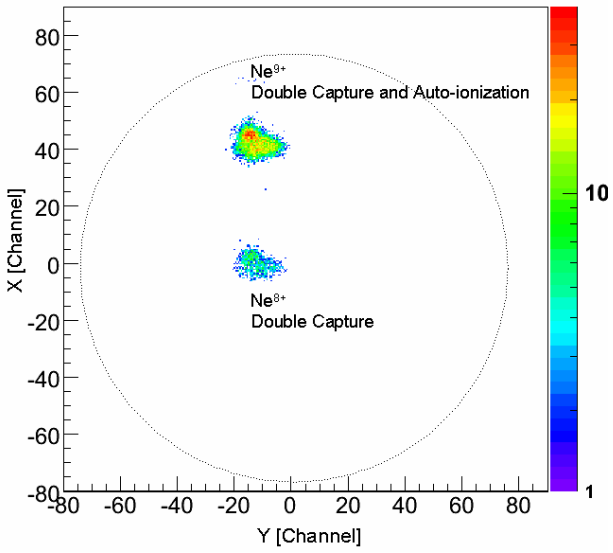

Figure V- 14 PSD image of projectile detection filtered for H^+/OD^+ fragmentation

The coincidence map for this experiment is shown in figure V-15. The distribution extension for all four dissociation channels is almost the same correspond to fast ion impact. On the other hand, as is seen clearly on the $H^+ + OD^+$ spectrum, the distributions width corresponding to the initial center-of-mass momentum distributions are about twice as wide as the result of fast ion impact. This corresponds to the higher momentum of the molecular ion after the collision due to a larger momentum transfer from the slow projectile ion.

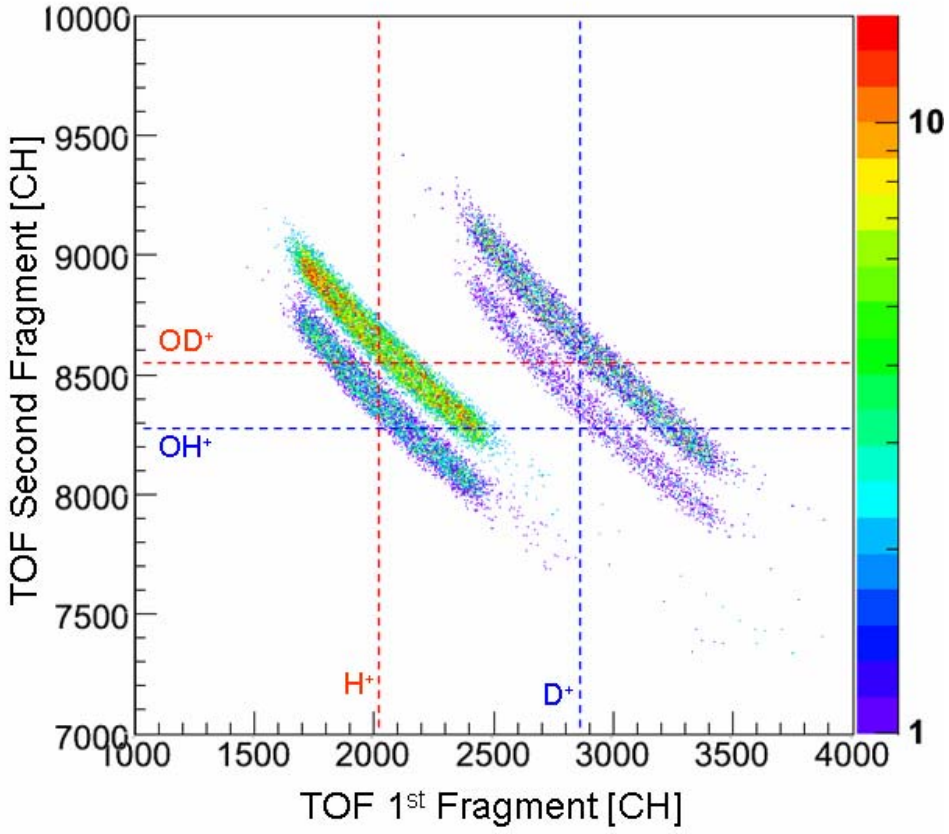

Figure V- 15 Superposition of four dissociation channels of interest after 3D position filtering

The obtained branching ratio and mean values for HDO, H_2O and D_2O dication two-body fragmentation shows finally very similar results as the high energy experiment. Comparing to $D^+ + OH^+$ channel, the branching ratio was found to be 5.6 for $H^+ + OD^+$ and to 3.3, 3.2 for $H^+ + OH^+$, $D^+ + OD^+$, respectively. The KER distribution width behaves as in the high energy experiment (figure V-16-18). The mean KER value of $H^+ + OD^+$ channel is, as well, 0.4eV higher than that of other channels. The observed clear difference between the high energy and low energy projectile experiment concerns the shape of KER distributions. As shown in figure V-19, the slow projectile KER distributions have a smaller contribution at low KER values (<5eV) than in the case of fast projectiles. This is may be a signature of the population in excited states but does not explain the difference between the theoretical and the experimental results.

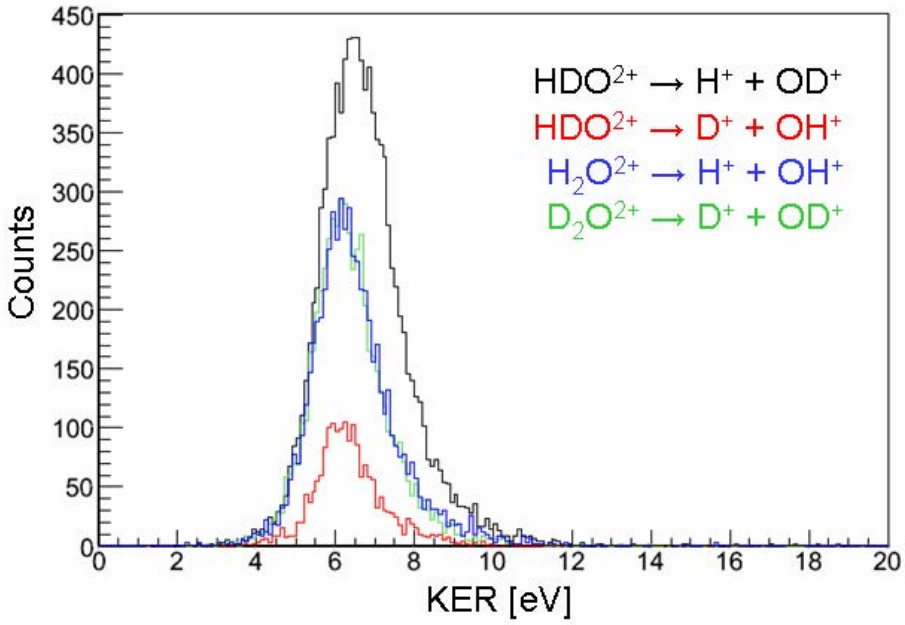

Figure V- 16 KER distributions of four dication two-body dissociation channels induced by 170keV Ne^{10+}, without normalization.

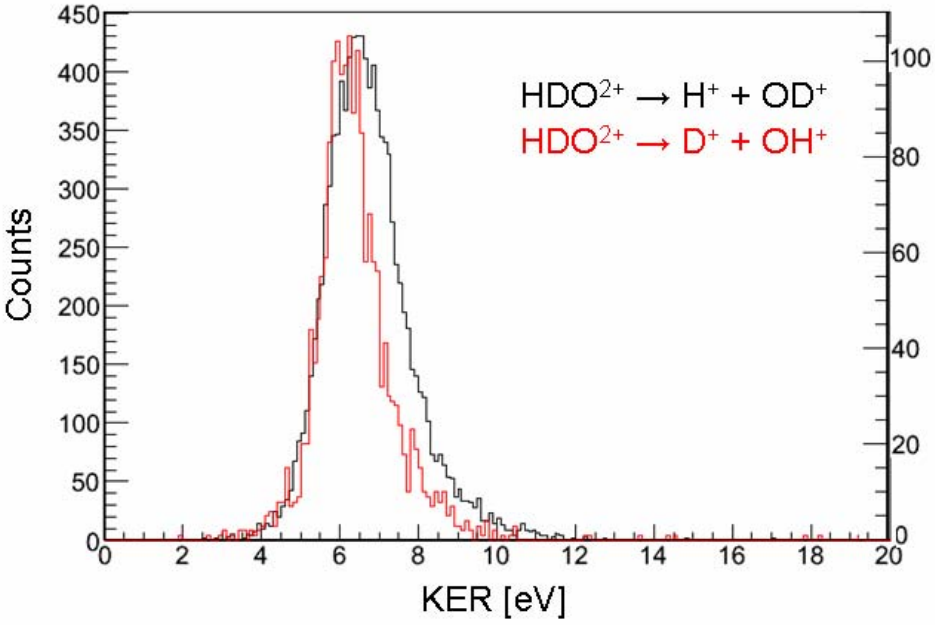

Figure V- 17 KER distributions of $HDO^{2+} \rightarrow D^+ + OH^+$ (red) , $H^+ + OD^+$ (black) dissociation channels induced by 170keV Ne^{10+}, normalized by peak height.

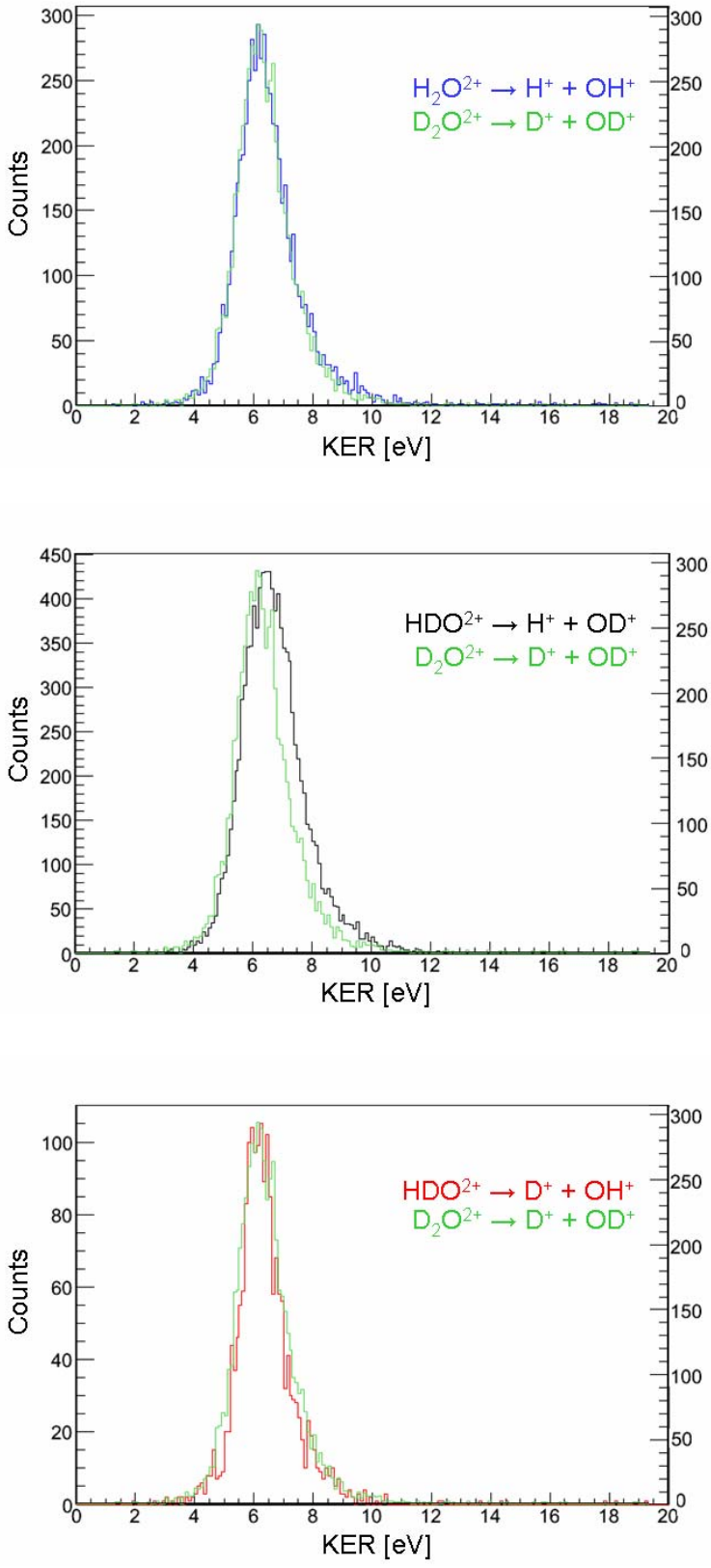

Figure V- 18 Comparison of each pair KER distributions among four dissociation channels: $H^+ + OD^+$ (black) , $D^+ + OH^+$ (red), $H^+ + OH^+$ (blue) , $D^+ + OD^+$ (green) induced by 170 keV Ne^{10+}.
a) Without normalization, b) and c): Normalized by peak height.

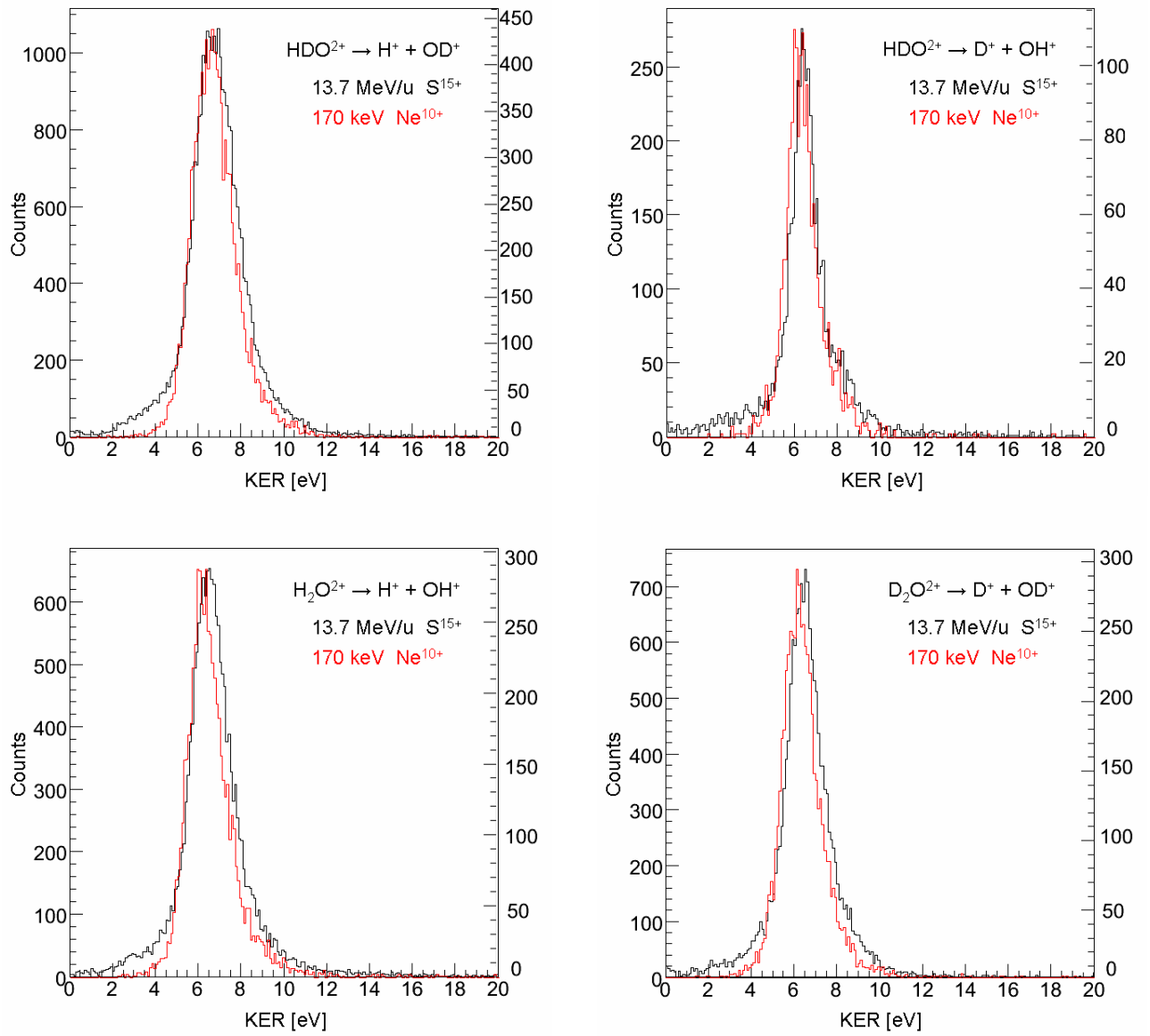

Figure V- 19 Comparison of KER distributions of four different dissociation channels induced by 13.7 MeV/u S^{15+} (black) and 170 keV Ne^{10+} (red), normalized by peak height.

Dissociation Channel	Total Counts	Ratio to ($D^+ + OH^+$)
$H^+ + OD^+$	10273	5.6 ± 0.1
$D^+ + OH^+$	1848	1
$H^+ + OH^+$	5874	3.2 ± 0.1
$D^+ + OD^+$	6024	3.3 ± 0.1

Table V- 3 Obtained total counts of four dissociation channels and branching ratios

V.6 Conclusion

The dominance of the $HDO \rightarrow H^+ + OD^+$ dissociation channel on the $D^+ + OH^+$ channel has been observed experimentally in two different ionization processes with higher accuracy. The main features of the process are nicely reproduced by a semi-classical calculation. The differences observed between experimental and theoretical results are reduced by enhancing the statistics and propagation time of the simulation. Although some quantitative differences remain, the preferential cleavage of O-H bond can be understood. This can be classically described as a "race" of H^+ versus D^+ ion. Because the lighter H^+ fragment is accelerated more than the D^+ ion, the O-H distance thus increases faster with respect to the O-D distance making the OD^+ potential attractive (see Figure V-11). As a consequence, the competition between O-H and O-D bond elongation leads, in most case, to the O-H bond breakage while the D^+ ion, still in the vicinity of the O atom, is trapped in the potential well of the OD^+ potential.

§ VI Summary

In this thesis, a detailed experimental study of the fragmentation dynamics of bent triatomic molecule: nitrogen dioxide (NO_2) and water (HDO, H_2O, D_2O) is presented. The experiments were conducted with the swift highly charged ion beams provided by the GANIL facility. This study evidences the competitive advantages of the use of fast ion impact ionization. While laser pulse duration lie in the femtosecond range, ion-molecular interaction may be two orders of magnitude shorter (attosecond, 10^{-18}s). Such short excitation time means that nuclear motion of the target fragments is free from any interaction with the projectile ion and is only due to the fragmentation process. This poly-atomic molecular fragmentation strongly benefited from the recent evolution of the COLd-Target Recoil Ion Momentum Spectroscopy (COLTRIMS). The multi-hit 4π solid angle detection and imaging techniques allow kinematically complete experiments. The measured positions and Time Of Flight of molecular ion fragments are converted into the corresponding momentum vectors.

In the case of NO_2, the dynamics of double and triple ionization dissociation are investigated with a time focusing spectrometer setup. This allows the measurement even in the case of undetected neutral fragments. The dissociation process of the triply charged molecular ion NO_2^{3+}, which dissociates into (N^+ /O^+ /O^+) is found to be synchronous concerted type similar to the case of CO_2^{3+} fragmentation. Both singly charged oxygen fragments are emitted with momenta making an angle of about 130 degrees, in molecular frame, close to the bond angle of neutral molecule NO_2 in its electronic ground state. This fact indicates that both N^+-O^+ bonds break simultaneously. The measured Kinetic Energy Release distribution of this channel shows a single broad peak at 34 eV. The geometrical contribution observed is that the central fragment N^+ also has a momentum, as expected, forming the bond angle. This is in contrast with the case of CO_2^{3+} which C^+ fragment is at rest and shows two peaks at around 23 eV and 36 eV in KER spectrum. On the other hand, NO_2^{2+} is found to have several dissociation channels. The doubly charged two-body dissociation leading to (NO^+/O^+) is the most frequent channel in this experiment. The KER distribution has a single sharp

peak at 6.7 eV which agrees with the previous results. In particular case, this (NO^+/O^+) state is regarded as an intermediate step to the complete dissociation ($N^+/O^+/O$). Due to the incompleteness of the fragment detection of this dissociation channel, avoiding random coincidence events coming mainly from the residual gas is the primary role of the analysis. The problem is solved by the use of the momentum conservation law. For this doubly ionized three-body breakup ($N^+/O^+/O$), two particular dissociation cases could occur. The first one is supported by the results from photoionization dissociation of NO_2^{2+} having KER around 9 eV with neutral oxygen at rest. The Dalitz diagram clearly shows that the configuration of the molecule changes during the fragmentation via metastable NO^{2+} fragment molecule. This dissociation channel named "differed charge separation" dissociation was not observed for CO_2^{2+} dissociation. The other type of dissociation, named as "initial charge separation" has already been observed for the ($C^+/O^+/O$) fragmentation channel of CO_2^{2+}. The first bond breakage leads to (NO^+/O^+) then, depending on the released energy, the dissociation may end as two-body (NO^+/O^+) or three-body ($N^+/O^+/O$) fragmentation channel. These sequential steps can only be observed at the lower KER (KER<20eV). As increases its released energy, the first and the second bond breakages interact with each other until the two bonds break simultaneously (synchronous concerted fragmentation). These different dissociation processes generating the neutral particles are intertwined. Consequently the dissociation process of doubly ionized nitrogen dioxide NO_2^{2+} into ($N^+/O^+/O$) can be defined as an asynchronous concerted fragmentation. For further investigation, the calculation of triatomic dication (CO_2^{2+}, NO_2^{2+}) potential energy surfaces is on its way.

Another approach to study doubly ionized triatomic molecular fragmentation was done with isotopic water molecules (HDO, H_2O, D_2O). The COLTRIMS type mass spectrometer with 3D position focusing condition was first adapted by the CIRIL group to this experiment. The shorter flight distance (without field free region) make it possible to reduce the magnitude of the electric extraction field keeping still a 4π collection solid angle and thus improve the KER resolution down to 100 meV. The kinematically complete measurement plays an essential role to identify and extract the true events from the random coincidences: the dissociation channel $H_2O^{2+} \rightarrow H^+ + OH^+$ recorded either from the target gas or from the residual gas in the reaction chamber can be distinguished one from the other, for example. Fragmentation of HDO^{2+} dication molecule is of particular interest with its strong isotopic preference for cleavage of the OH bond over the OD bond. The motivation of our experiments is to observe the underlying fragmentation process precisely with an improved spectrometer and to evaluate the role of excited states in this isotopic asymmetry by fast and slow highly charged heavy ion impact. In order to compare with isotopic molecules, all dication dissociation channels (H^+/OD^+), (D^+/OH^+), (H^+/OH^+) and (D^+/OD^+) are analyzed in the same way.

In this experiment, either at low or high energy, highly charged projectile ions lead to the same branching ratio: $(H^+ + OD^+) / (D^+ + OH^+) = 5.7 \pm 0.1$. However, slight differences have been observed in the KER distributions of all dication dissociation channels. The KER of the fast ion impact show a strange contribution at the low KER region. By an improved semi-classical calculation, the main features of the process are nicely reproduced. The differences observed between experi-

mental and theoretical results have been reduced by enhancing the statistics and the propagation time of the simulation. Although some quantitative differences remain, the preferential cleavage of O-H bond can be understood. The calculated potential energy surface of HDO^{2+} revealed the mechanism of the "race" between H^+ and D^+: since the lighter H^+ fragment is accelerated more than the D^+ ion, the O-H distance thus increases faster with respect to the O-D distance making the OD^+ potential attractive. In the next future, the theoretical calculation will be improved by implementing excited potential energy surfaces contributing to the $H^+ + OH^+$ fragmentation channel.

References I

[I.1] L. Adoui, C. Caraby, A. Cassimi, D. Lelièvre, J.P. Grandin, A.Dubois: J. Phys. B: At. Mol. Opt. Phys. 32, 631 (1999)

[I.2] K. Wohrer, G. Sampoll, R.L.Watson, M. Chabot, O. Heber, V. Horvat: Phys. Rev. A 46, 3929 (1992)

[I.3] I. Ben-Itzhak, S.G. Ginter, V. Krishnamurthi, K.D. Carnes: Phys. Rev. A 51, 391 (1995)

[I.4] H. Tawara, T. Tonuma, T. Matsuo, M. Kase, H. Kumagai, I. Kohno: Nucl. Instrum. Methods A 262, 95 (1987)

[I.5] T. Matsuo, T. Tonuma, M. Kase, T. Kambara, H. Kumogai, H. Tawara: Chem. Phys. 121, 93 (1988)

[I.6] G. Sampoll, R.L.Watson, O. Heber, V. Horvat, K.Wohrer, M. Chabot: Phys. Rev. A 45, 2903 (1992)

[I.7] I. Ben-Itzhak, S.G. Ginter, K.D. Carnes: Phys. Rev. A 47, 2827 (1993)

[I.8] J.Vancura and V.O. Kostoum, Phys.Rev.A 49, 321 (1994)

[I.9] A Remscheid, B.A.Huber, M.Pykavyj, V.Staemmler and K.Wiesemann, J.Phys.B: At. Mol. Opt. Phys. 29, 515 (1996)

[I.10] M. Tarisien, L. Adoui, F. Frémont, D. Lelièvre, L. Guillaume, J.Y. Chesnel, H. Zhang, A. Dubois, D. Mathur, Sanjay Kumar, M. Krishnamurthi, A. Cassimi: J. Phys. B: At. Mol. Opt. Phys. 33, L11 (2000)

[I.11] C. Maul, K.H. Gericke: Int. Rev. Phys. Chem. 16, 1 (1997)

[I.12] S. Hsieh, J.H. Eland: J. Phys. B: At. Mol. Opt. Phys. 30, 4515 (1997)

[I.13]J.Ullrich, V.P.Shevelko (Eds.) Many-Particle Quantum Dynamics in Atomic and Molecular Fragmentation, ISBN 3-540-00664-2 Springer-Verlag Berlin, Heidelberg (2003)

[I.14] Th.Weber, O. Jagutzki, M. Hattass, A. Staudte, A. Nauert, L. Schmidt,M.H. Prior, A.L. Landers, A. Bräuning-Demian, H. Bräuning, C.L. Cocke, T. Osipov, I. Ali, R. Diez Muino, D. Rolles, F.J. Garcia de Abajo, C.S. Fadley, M.A. Van Hove, A. Cassimi, H. Schmidt-Böcking, R. Dörner: J. Phys. B: At. Mol. Opt. Phys. 34, 3669 (2001)

[I.15] T.D. Märk: Electron Impact Ionization, ed. by T.D. Märk and G.H. Dunn (Springer, New York 1985)

[I.16] I. Nenner, P. Morin: 'Electronic and Nuclear Relaxation of Core Excited Molecules'. In: VUV ans Soft X-Ray Photoionization Studies in Atoms and Molecules, ed. by U. Bexker and D.A. Shirley (Plenum, London 1995)

[I.17] S. Chelkowski, P.B. Corkum, A.D. Banbrauk: Phys. Rev. Lett. 82, 3416 (1999)

[I.18] W.C.Wiley and I.H.McLAren ; Rev. Sci. Instrum., Vol. 26, p.1150, (1955)

[I.19] R. Dörner, H.Bräuning, J.M.Feagin, V.Mergel, O.Jagutzki, L.Spielberger, T.Vogt, H.Khemliche, M.H.Prior, J.Ullrich, C.L. Cocke, H. Schmidt-Böcking; Phys.Rev.A 57, 1074 (1998)

[I.20] M.A. Abdallah, W.Wolff, H.E. Wolff, E.Y.Kamber, M.Stöckli, C.L.Cocke; Phys.Rev.A 58 2911 (1988)

[I.21] M.Tarisien ; Thesis for doctorat de l'Université de Caen, (2003)

[I.22] R.G. Cooks, D.T. Terwilliger, J.H. Beynon, J. Chem. Phys. 61 (1974) 1208.

[I.23] J.H.D. Eland, F.S. Wort, P. Lablanquie, I. Nenner, Z. Phys. D 4 (1986) 31.

[I.24] J.H.D. Eland, Mol. Phys. 61 (1987) 725.

[I.25] P.G. Fournier, J.H.D. Eland, P. Millie, S. Svensson, S.D. Price, J. Fournier, G. Comtet, B. Wannberg, L. Karlsson, P.
Baltzer, A. Kaddouri, U. Gelius, J. Chem. Phys. 89 (1988) 3553.

[I.26] T.Masuoka, A.Kobayashi; Chemical Physics 302 31 (2004)
[I.27] S.Legendre, E.Giglio, M.Tarisien, A.Cassimi, B.Gervais and L.Adoui; J. Phys. B: At. Mol. Opt. Phys. 38, L233–L241 (2005)
[I.28] A. M.Sayler, M.Leonard, K.D.Carnes, R.Cabrera-Trujillo, B.D.Esry and I.Ben-Itzhak; J. Phys. B: At. Mol. Opt. Phys. 39, 1701–1710 (2006)

References II

[II.1] P.Jardin ; Thesis for doctorat de l'Université de Caen, (1995)
[II.2] C.Caraby, A.Cassimi, L.Adoui and J.P.Grandin ; Phys. Rev. A, Vol. 55, p.2450, (1997)
[II.3] M.Tarisien ; Thesis for doctorat de l'Université de Caen, (2003)
[II.4] X.Fléchard ; Thesis for doctorat de l'Université de Caen, (1999)
[II.5] R.Campargue ; Thèse de doctorat de la Faculté des sciences de Paris, (1970)
[II.6] R.Campargue ; J. Phys. Chem., Vol. 88, p. 4466, (1984)
[II.7] M.Lundqvist, P.Baltzer,D.Edvardsson, L.Karlsson and B.Wannberg ; Phys.Rev. Lett., Vol. 75, p. 1058, (1995)
[II.8] W.C.Wiley and I.H.McLAren ; Rev. Sci. Instrum., Vol. 26, p.1150, (1955)
[II.9] Roentdek http://www.roentdek.com/
[II.10] CERN http://root.cern.ch/

References IV

[IV.1] H.Hogreve: J. Phys. B: At. Mol. Phys., Vol. 28, p. L263, (1995).
[IV.2] Th.A.Field and J.H.D.Eland: Chem. Phys. Lett., Vol. 211, p. 436, (1993).
[IV.3] C.Tiany and C.R.Vidal: Phys. Rev. A, Vol. 58, p. 3783, (1998).
[IV.4] J.H.D. Eland: Mol. Phys. 61 725 (1987).
[IV.5] T.Masuoka, A.Kobayashi: Chemical Physics 302 31 (2004).
[IV.6] R.H.Dalitz ; Philos. Mag., Vol. 44, p. 1068, (1953).
[IV.7] A.A.Hoops, J.R.Gascooke, A.E.Faulhaber, K.E.Kautzman and D.M.Neumark ; Chem. Phys. Lett., Vol. 374, p. 235, (2003).
[IV.8] Ch. Maul and K.H.Gericke ; J. Phys. Chem. A, Vol. 104, p. 2531, (2000).
[IV.9] L.M.Wiese, O.Yenen, B.Thaden and D.H.Jaecks ; Phys. Rev. Lett., Vol. 79, p. 4982, (1997).
[IV.10] V. Kokoouline and C.H. Greene: Phys. Rev. A, Vol. 68, 012703 (2003).
[IV.11] D.Strasser, L.Lammich, H.Kreckel, S.Krohn, M.Lange, A.Naaman, D.Schwalm, A.Wolf and D.Zajfman; Phys. Rev. A, Vol. 66, p. 32719, (2002).
[IV.12] B.Siegmann, U.Werner, H.O.Lutz and R.Mann; J. Phys. B: At. Mol. Phys., Vol. 35, p. 3755, (2002).
[IV.13] M.Tarisien; Thesis for doctorat de l'Université de Caen, (2003).
[IV.14] T. Masuoka, I. Koyano, N. Saito, Phys. Rev. A, Vol. 44, 4309 (1991).
[IV.15] T. Masuoka, J. Electron. Spectrosc. Relat. Phenom. 101–103 (1999).
[IV.16] T. Masuoka and A. Kobayashi; J.Chem. Phys.vol, 113, 16 22 (2000).
[IV.17] R.K. Singh, G.S. Lodha, V. Sharma, I.A. Prajapati, K.P. Subramanian, and B. Bapat; Phys. Rev. A, Vol. 74, 022708 (2006).

References V

[V.1] S.Legendre, E.Giglio, M.Tarisien, A.Cassimi, B.Gervais and L.Adoui; J. Phys. B: At. Mol. Opt. Phys. 38, L233–L241 (2005)
[V.2] A. M.Sayler, M.Leonard, K.D.Carnes, R.Cabrera-Trujillo, B.D.Esry and I.Ben-Itzhak; J. Phys. B: At. Mol. Opt. Phys. 39, 1701–1710 (2006)
[V.3] B. Siegmann , U.Werner, H.O.Lutz and R.Mann J. Phys. B 34 L587 (2001)
[V.4] N.E.Henriksen, K.B.Moller and V.Engel; J. Chem. Phys. 122, 204620 (2005)
[V.5] H.Akagi, H.Fukazawa, K.Yokoyama and A.Yokokawa; J. Chem. Phys. 123, 184305 (2005)
[V.6] H.Partridge and D.W.Schwenke; J. Chem. Phys. 106, 11, 4618-4639 (1997)
[V.7] K.S.Sorbie and J.N.Murrell; Mol. Phys. 29, 1387 (1975)
[V.8] P. R. Bunker, Ota Bludsky, Per Jensen, S. S. Wesolowski, T. J. Van Huis, Y. Yamaguchi and H. F. Schaefer, III; J. Mol. Spectroscopy**,** 198, 2, 371-375 (1999)

Appendix A
Contribution of Dimer N_2O_4

Due to the phase diagram of NO2 discussed in section II.2, one have to give special attention to the contribution of N2O4 dimers to the results.

By comparing the two types of run of which target gas injection pressure was around 2bars and 5bars, the contribution of dimer in the results can be estimated. The proof of existence of fragments from dimer was first found in the TOF spectrum of NO_2^+. The singly charged "parent" molecule with no initial momentum due to breakup should have the sharp peak expected from the cold supersonic gas jet. However, it is obviously shown in the figure A-1, a broad distribution is observed below the main sharp peak. The larger injection pressure provides a larger contribution from the dimers (redline). The rising question was how this contribution impacts on NO_2 fragmentation: could we extract the proper events from those coming from the dimer molecule.

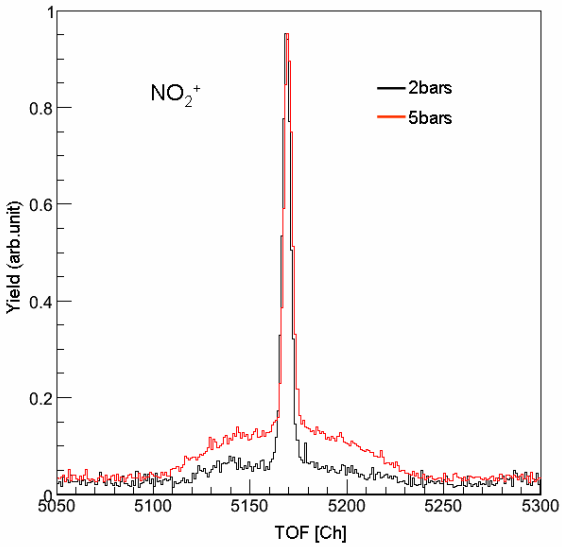

Figure A-1
TOF mass spectrum of NO_2^+ on the raw data (TG_DI) normalized to the peak height. The red line corresponds to the 5bars injection pressure. With higher contained amount of dimers shows higher mound due to the fragment NO_2^+ around the sharp peak from charged parent monomer molecule.

The pedestal under the sharp NO_2^+ peak is obviously increased compared to the case of a 2 bars injection pressure (see also figure III-7).

In the case of the triply ionized dissociation channel $NO_2^{3+} \rightarrow N^+ + O^+ + O^+$, the filters on the sum of momentum components (see section IV.2) was the most effective way to reduce the false events. Series of Dalitz plot presented in figure A-2 show the distribution of triple coincidence ($N^+/O^+/O^+$) events obtained by different injection pressures before and after filtering.

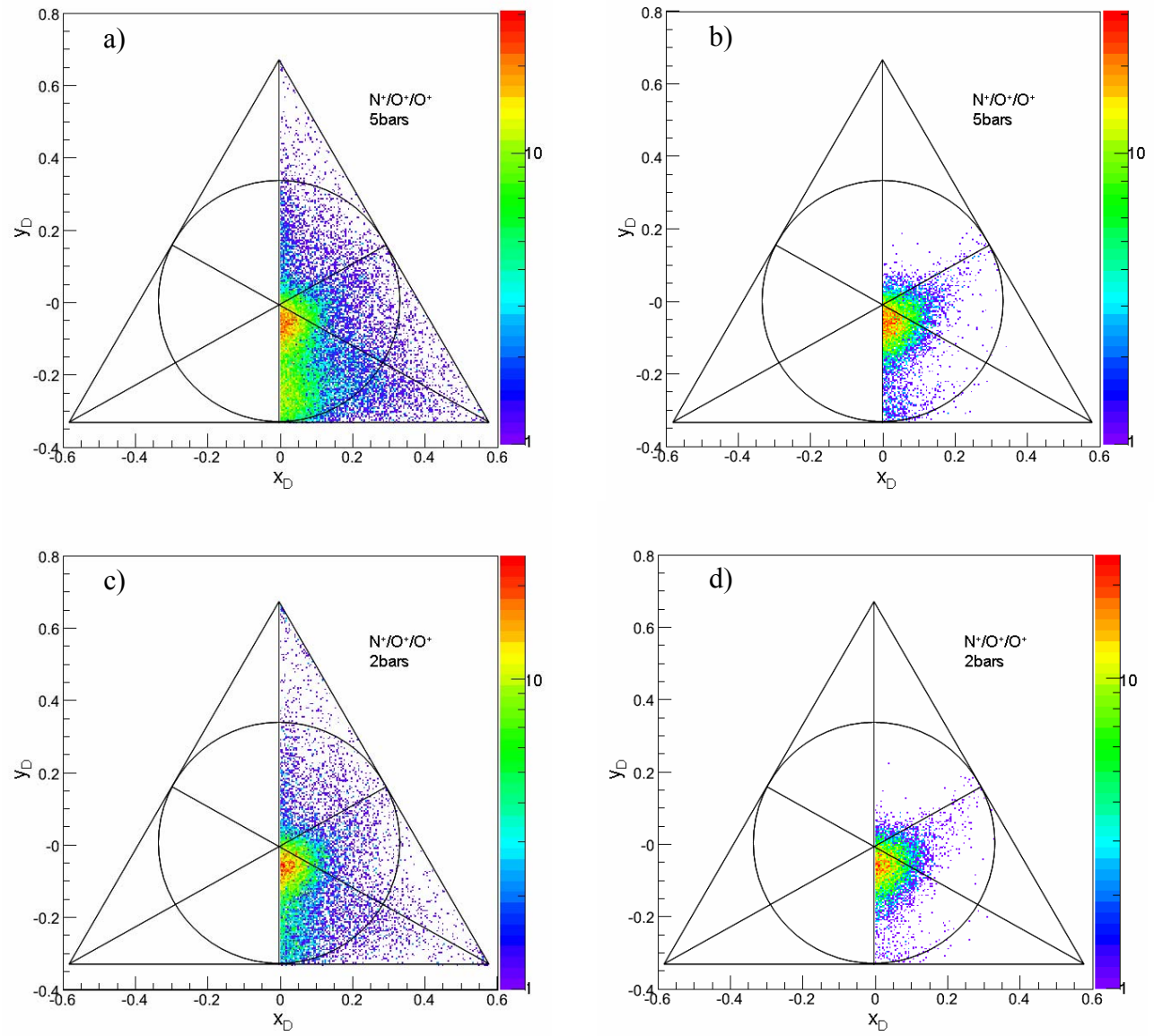

Figure A-2 Dalitz plots of the dissociation channel $NO_2^{3+} \rightarrow N^+ + O^+ + O^+$ with target gas injection pressure of 5 bars a), b) and 2 bars c), d). Plots a), c) are raw data of triple coincidence measurement and b), d) are after filtering by each component of momentum sum. The "pollution" due to dimes can be removed by the momentum sum filters but still remains for the case of high target injection pressure.

The distribution at the center bottom position is notably large for the case of 5 bars injection pressure experiment without filtering. Although it is not possible to remove the dimer contribution

completely, only by the momentum conservation law the false events can be reduced to less than 1 percent of all events, as shown in upper right side figure. As shown in the figure A-3, the contribution of dimer is hardly recognized in KER spectrum after cleaning. A weak difference can be seen in the spectra before filtering but only at higher KER region (Both spectra are normalized by peak height), and disappears completely after filtering.

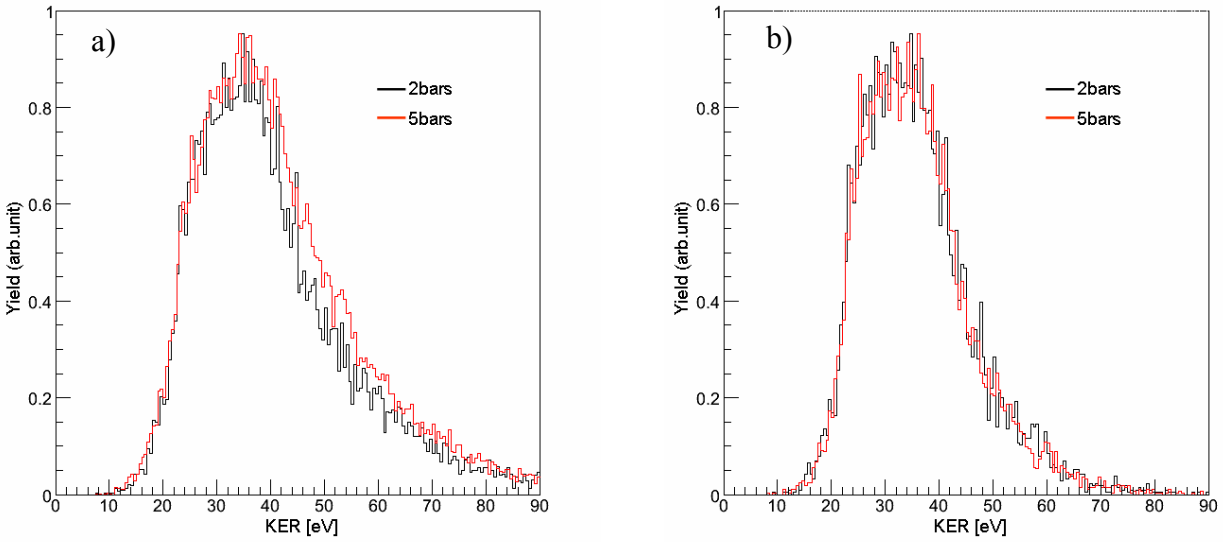

Figure A-3 Kinetic Energy Release distributions of the dissociation channel $NO_2^{3+} \rightarrow N^+ + O^+ + O^+$ with target gas injection pressure of 5 bars (red line) and 2 bars (black line). It is hardly to see the difference between distributions of two cases after filtering (b) in the 1D spectrum.

The distribution due to the dimes at the center bottom region is of course observed for the case of (N^+/O^+) double coincident measurement (figure A-3) as well. While the ratios of the particular structures (A-C) discussed in the section IV.5 to the total counts are unchanged, the events on the center bottom distribution for the 5 bars experiment were measured three times more than that for the 2 bars injection pressure. Another strong distribution at lower left hand side shown in unfiltered plot figure A-4.a) and c) is the contribution of the residual gas N_2 and O_2. The interested reader will be also able to refer to Appendix B for further information on the residual gas contribution and the elimination method.

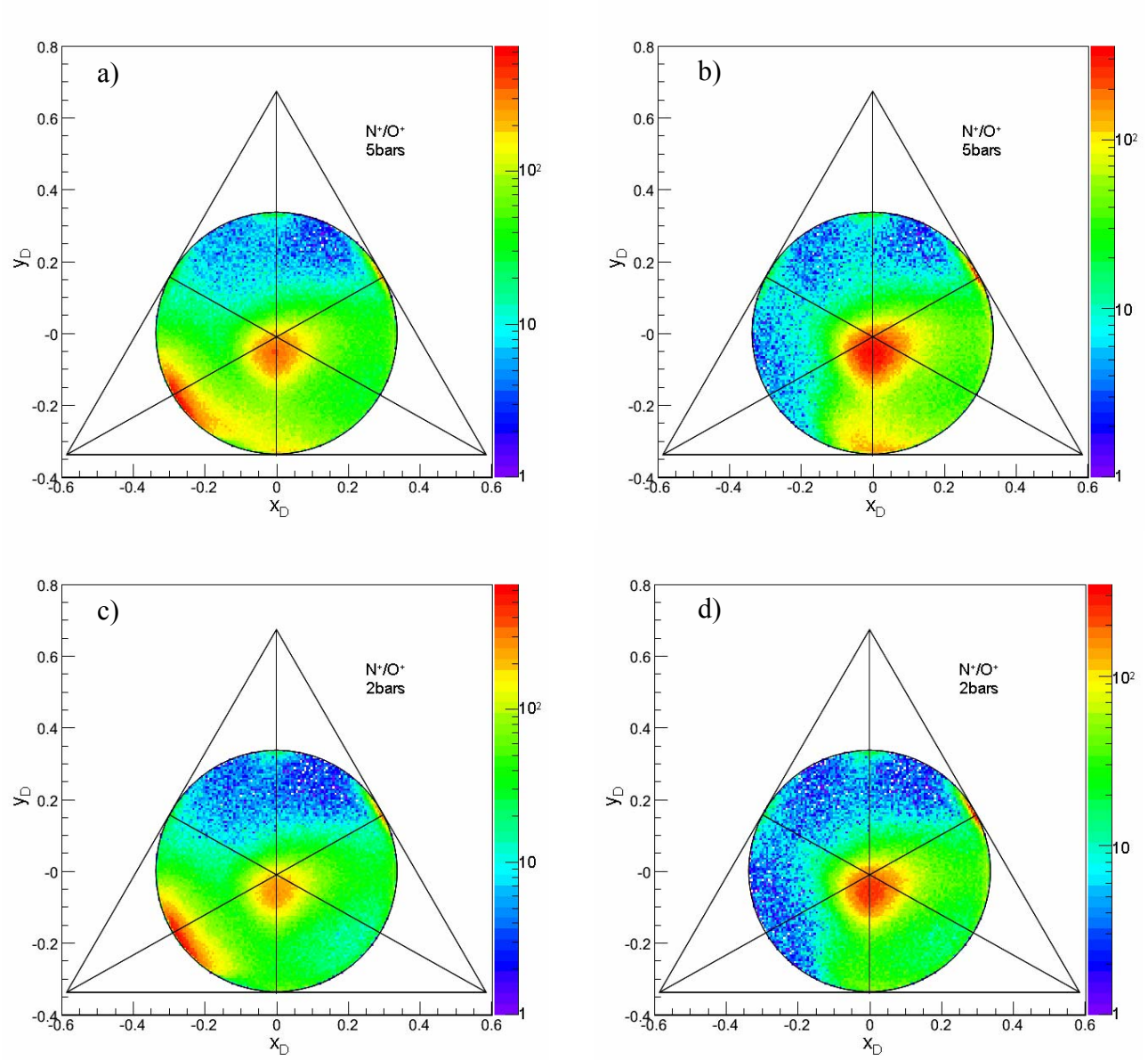

Figure A-4 Dalitz plots of the dissociation channel of double coincidence measurement (N^+ /O^+) with target gas injection pressure of 5 bars a), b) and 2 bars c), d). Plots a), c) are raw data of tdouble coincidence measurement including the contribution of residual gas fragmentation and b), d) are after filtering by each component of momentum sum.

Appendix B

Separation of ($N^+/O^+/O$) channel from other contributions

Since only two fragments out of three are detected, extracting of ($N^+/O^+/O$) fragmentation channel needs a special care in order to eliminate contribution from other channels. From the wide time of flight window shown in figure IV-21, the double coincidence events for analysis have to be chosen properly.

One critical contribution comes from residual gas (N^+/N^+) and (O^+/O^+). By measuring the background spectrum without target molecular gas (figure B-1) and applying the same analysis, the corresponding peaks from residual gas was successfully determined. The momentum sum of the first and second fragments on the x direction (along the electric extraction field) was calculated choosing the first fragment as N^+ and the second one as O^+. Therefore, the background signal (N^+/N^+) and (O^+/O^+) lead to sharp peaks but far from zero due to wrong mass combination (figure B-2).

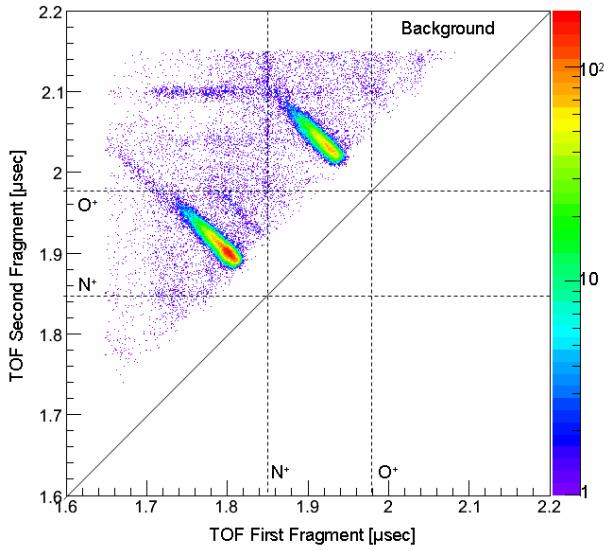

Figure B-1 Coincidence map of the first and second fragments from the residual gas in the reaction chamber collision with the 4.7MeV/u Ne^{8+} projectile. Double coincident detection for the fragments from background N_2 and O_2 are observed

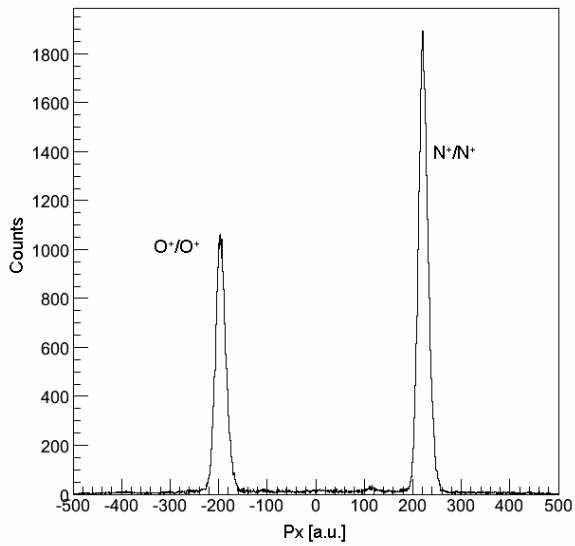

Figure B-2 Momentum sum component along the electric extraction field direction for the background measurement. Two fragments are calculated by the charges and mass as (N^+/O^+).

The background signal on the Dalitz plot is shown in figure B-2 (see also A-4).

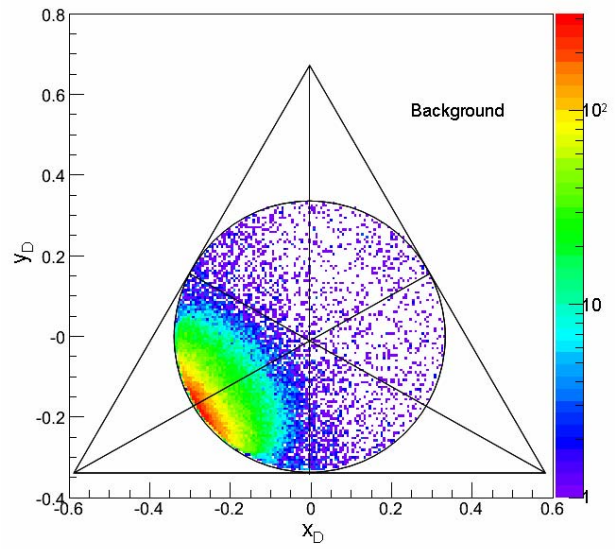

Figure B-3 Dalitz plot can be reconstructed by calculating the momentum of the third fragment. Such a structure is visible on figure A-4 which is attributed to the background contribution.

The other problem is that the separation from triple coincidence events consisting mainly ($N^+/O^+/O^+$) with undetected O^+ fragment. Although it is difficult to suppress completely its contribution, by comparing with the results obtained by the triple coincident measurement, it is possible to extract the specific features of ($N^+/O^+/O$) dissociation channel. To do so, it is necessary to apply the same analysis to both sets of data. As explained section IV.4, the events only with the forward-emitted N^+ have been selected for the case of ($N^+/O^+/O^+$). Thus one has to apply the same condition, i.e. $V_x(N^+)>0$ to the measured (N^+/O^+) coincidence events. Finally by filtering both $V_x(N^+)$ and sum of momentum components, we have obtained the double coincidence measurement data set to compare with the triple coincidence events.

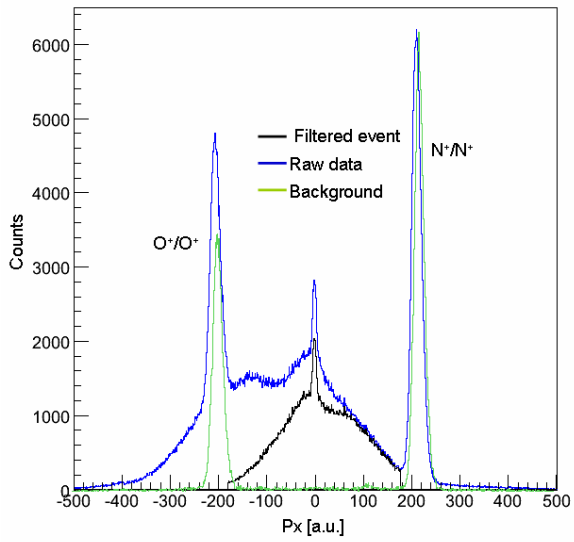

Figure B-4 Momentum sum spectra in the electric extraction field direction for the raw double coincident data in the window (figure IV-21) (blue line), background measurement (green line) and final reduced one (black line).

The 2D position image on the recoil ion detector gives the confirmation of the removing noises. Figure B-5 shows the position of the first fragment in case of double-hit detection on the recoil ion detector. The Z axis corresponds to the projectile beam direction while the Y axis corresponds to the target gas jet direction.

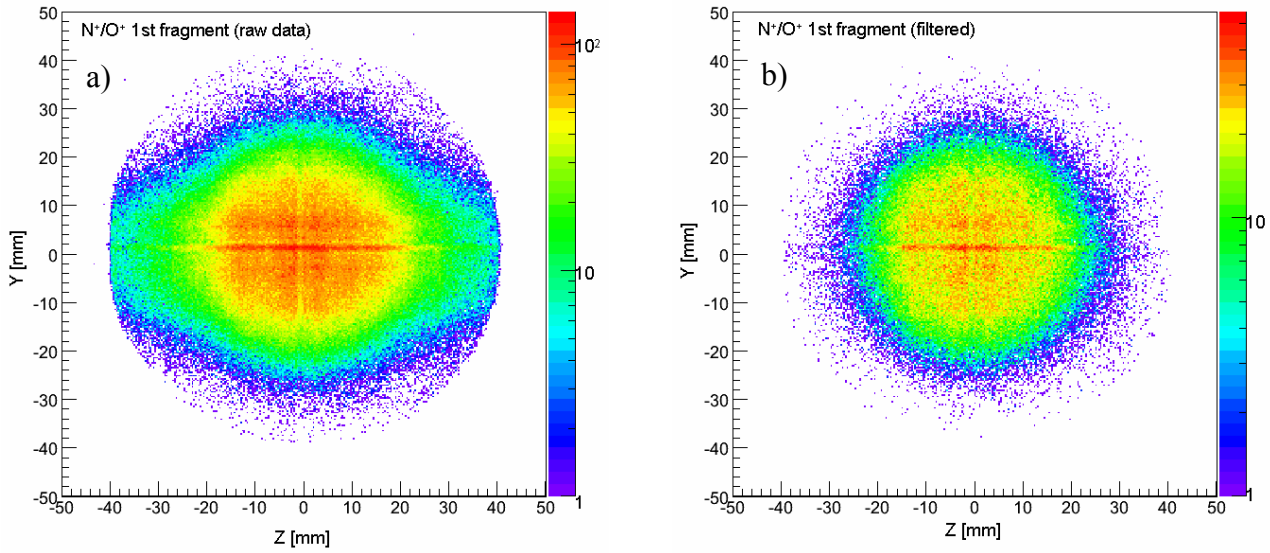

Figure B-5 The detector image of the first fragment of a) all double coincident measurements in the time window and b) after filtering by V_x and momentum sum. The isotropic distribution of the fragment emission is the reason of this round image.

The effect of this filtering appears clearly on figure B-5 as an imposed quality of the image on the position sensitive detector. The resulting circlr distribution is a direct evidence of the isotropy of the fragmentation process.

Dynamique de la fragmentation de molécules tri-atomiques: contribution de la géométrie

Résumé

La dynamique de fragmentation des molécules poly-atomiques est un problème compliqué du fait de l'existence de couplages entre leurs différents degrés de liberté. Dans le but de comprendre le rôle de ces couplages, nous av+

-ons étudié la fragmentation de molécules triatomiques induite par impact d'ions rapides multichargés. L'intérêt de ces ions est de conduire à une ionisation multiple de la molécule au cours d'une interaction d'une durée de quelques attosecondes (10^{-18}s). Ce temps est suffisamment bref pour que la relaxation, par fragmentation, de l'ion moléculaire ainsi créé se fasse hors de toute perturbation extérieure. Les premières études réalisées sur le CO_2 soumis aux ions Ni^{24+} de 8 MeV/u ont montré que la fragmentation de l'ion moléculaire CO_2^{q+} pouvait être modélisée par une fragmentation concertée synchrone (q=3) ou une fragmentation concertée asynchrone (q=2), i.e. par l'intermédiaire d'un mode de vibration asymétrique de la molécule. Nous avons réalisé des expériences avec des molécules non linéaires telles que NO_2, D_2O, H_2O et HDO pour lesquelles les couplages entre degrés de liberté sont différents de ceux rencontrés dans les molécules linéaires comme CO_2, et ainsi tester ce modèle de dissociation plus sévèrement. Dans le cas de fragmentation du NO_2^{2+} induite par des ions Ne^{8+} de 4.7Mev/u, des fortes différences, par rapport à CO_2^{2+}, ont été observées en raison de la contribution de la géométrie. La fragmentation de HDO^{2+} a permis de confirmer à haute et basse énergie de collision, un important effet isotopique: la rupture de la liaison O-H est 5.7 fois plus probable que celle de la liaison O-D.

Dynamics of triatomic molecular fragmentation: contribution of geometry

Abstract

The dynamics of the fragmentation process, rather simple for diatomic molecules, becomes more interesting in the case of poly-atomic molecules due to the coupling between the additional internal degrees of freedom (bending, stretching…). In order to reveal the role of these contributions, we studied several bent triatomic molecules (NO_2, H_2O, D_2O, HDO).

Ion-impact induced fragmentation of molecule is a well adapted way to observe the momentum sharing among atoms in a molecule due to a short interaction time (10^{-18}s). A first study of carbon dioxide CO_2 fragmentation induced by collision with 8 MeV/u Ni^{24+} has shown that the fragmentation dynamics of molecular ion CO_2^{q+} can be categorized as synchronous concerted fragmentation (q=3) or asynchronous concerted fragmentation (q=2), i.e. fragmentation through an intermediate asymmetric vibration mode. We have conducted experiments with NO_2, D_2O, H_2O and HDO target molecules in order to test this behaviour in the more general case of molecules with a bond angle. In the case of NO_2^{2+}, induced by 4.7Mev/u Ne^{8+}, clear differences, compared to CO_2^{2+} fragmentation have been observed. In the case of HDO^{2+} fragmentation, the strong selectivity of bond cleavage has been confirmed and a new branching ratio $(H^+ + OD^+)/(D^+ + OH^+) = 5.7 \pm 0.1$ measured.

Mots-clés

Dynamique Moléculaire, Molécules Polyatomiques, Interactions Ion-Molécule, Ionisation, Effet Isotopique, Accélérateur d'Ions Lourds, Grand Accélérateur National d'Ions Lourds (France), COLTRIMS

Discipline

Milieux dilués et optique fondamentale

Laboratoire

Centre Interdisciplinaire de Recherche Ions Lasers (CIRIL)
CIRIL-GANIL, Avenue H. Becquerel, BP 5133, 14070 Caen Cedex 5